



UNIVERSITÀ DEGLI STUDI DI GENOVA

Facoltà di Scienze Matematiche, Fisiche e Naturali
Dipartimento di Fisica

**Search for the Standard Model Higgs
boson produced by vector boson
fusion and decaying to beauty quarks
with the ATLAS detector.**

Carlo Varni

19 March 2015

Thesis Advisors: Dr. Fabrizio Parodi, Dr. Carlo Schiavi

Thesis Co-Advisor: Dr. Carla Biggio

A Thesis presented for the degree of
Master of Science in Physics.



To my Mom



Abstract

The Higgs Boson has been discovered in 2012 by the ATLAS and the CMS collaborations. Studying its properties and checking if they agree with the Standard Model predictions constitute pivotal topics in High Energy Physics research. This analysis presents the current status of a search for an Higgs Boson produced via the Vector Boson Fusion mechanism and decaying to a $b\bar{b}$ pair, performed with $\sim 20 \text{ fb}^{-1}$ of LHC proton-proton data at $\sqrt{S} = 8 \text{ TeV}$, collected by the ATLAS experiment during the 2012 data-taking campaign. For an Higgs mass of 125 GeV, the Vector Boson Fusion process possesses the second largest cross section, and the bottom quark pair is the main decay channel. The clear event topology is exploited for trigger selection. The author's work focuses on data-screening tuning by means of Multivariate Analysis techniques, background modelling, signal extraction, and systematic errors assessment. We expect an uncertainty of the signal strength, normalized to the expected SM prediction, of $\sigma_{\mu}(stat) = \pm 1.8$, without taking into account the systematic uncertainties.

Contents

Introduction	1
1 Theoretical background	3
1.1 The standard model	3
1.1.1 Electromagnetic interactions	4
1.1.2 Weak interactions	6
Electro-weak interactions for quarks	8
1.1.3 Strong interactions	10
1.2 Spontaneous symmetry breaking	11
1.2.1 The Brout-Englert-Higgs mechanism	11
1.2.2 Quark and lepton masses	13
1.3 The standard electroweak Lagrangian	14
1.4 The Higgs boson search	16
2 The ATLAS experiment	21
2.1 The Large Hadron Collider	21
2.2 The ATLAS Experiment	23
2.2.1 Inner Detector	26
Pixel Detector	26
SemiConductor Tracker	29
Transition Radiation Tracker	29
2.2.2 Calorimeter detector	30
The electromagnetic calorimeter	30
The hadronic calorimeter	31
The forward calorimeter	31
2.2.3 Muon Spectrometer	31
2.2.4 The trigger system	35
2.3 Software infrastructure	36
2.3.1 ATLAS software	37
2.4 LHC operations	37
3 Events selection	39
3.1 The data sample	39
3.2 MC Samples	40

3.2.1	Higgs boson	41
3.2.2	Z^0 boson	41
3.3	Preselection	42
3.3.1	Trigger	44
3.3.2	p_T^{jets} threshold	44
3.3.3	p_T^{bb} threshold	44
3.4	Multivariate analysis	45
3.5	Significance	46
4	Fit to the $b\bar{b}$ pair invariant mass	51
4.1	Fit strategy	51
4.1.1	BDT Regions	52
4.1.2	Fit Range	54
4.2	Combinatorial backgrounds	56
4.3	Signals determination	56
4.4	Systematic uncertainties	58
4.4.1	Background-modelling uncertainty	58
4.4.2	b -tagging uncertainty	60
4.4.3	Jet-Energy-Scale uncertainty	60
4.4.4	Theory uncertainty	61
4.5	Comparison with CMS	62
	Conclusions	65
	Appendix A ATLAS coordinate system	67
	Appendix B b-tagging	69
	Appendix C Monte Carlo Simulations	73
	Appendix D Multivariate Analysis Techniques	77
D.1	Boosted Decision Tree	78
D.2	MultiLayers Perceptron Neural Network	79
D.3	LikelihoodPCA	80
D.4	H-matrix discriminant	81

Introduction

The introduction of the Higgs field in the Standard Model lagrangian explains the masses of elementary particles through a mechanism of spontaneous symmetry breaking. Theorized in the 60s, it remained for 50 years a chimera, waiting to be found. Researchers conducted experiments in different facilities – LEP and Tevatron – but their findings were not relevant to prove its existence. Eventually, in 2012, the ATLAS and CMS experiments announced the discovery of a new Standard Model Higgs boson-like particle [1, 2]. Since then, the High Energy Physics community made this new-found boson the pivotal topic in their searches, systematically studying its properties. More precise measurements strengthened the hypothesis this particle was indeed a Higgs boson [3, 4, 5], later confirmed in 2013 [6]. Waiting for the incoming resumption of LHC operations on March 2015, the so-called Run-II, further analysis of the Run-I data sample is still ongoing.

The LHC proton-proton collisions can produce such a particle through different processes. For an Higgs mass of 125 GeV [7], the gluon-gluon fusion mechanism possesses the highest cross-section value, and the b -quark pair is the main decay channel [8, 9]. However, such a search is impossible due to the large amount of background QCD events with an analogous topology at LHC. The Vector Boson Fusion production possesses the second largest value of cross-sections. Recently the CMS experiment presented the preliminary results on a search for an Higgs boson produced in such a way and decaying to a $b\bar{b}$ pair [10]. They observed a fitted signal strength of $\mu = \sigma/\sigma_{SM} = 0.7 \pm 1.4$.

We aim to perform a similar study analysing the $\sim 20 \text{ fb}^{-1}$ of LHC proton-proton data at $\sqrt{S} = 8 \text{ TeV}$, collected with the ATLAS detector [11]. Our analysis is based on Multivariate Analysis techniques in order to select data and maximize the signal significance. During this work we cross-checked the results with a cut-based analysis, performed by the ATLAS UChicago group¹ – an alternative approach to our analysis strategy. Their work is reported on a supporting note [12]. This analysis is currently under review by an ATLAS internal Editorial Board, so all the results presented in the following are still to be considered preliminary.

The author of this thesis essay focused on different aspects: data-screening

¹<http://hep.uchicago.edu/atlas/>

tuning; background modelling; signal extraction; systematic errors assessment. The essay is structured into four chapters and four appendices:

- Chapter 1 presents a brief overview of the Standard Model theory, with particular focus on the role the Higgs boson covers.
- Chapter 2 describes the experimental apparatus used, i.e. the ATLAS detector.
- Chapter 3 explains how we shortlisted the massive data pull taken during the 2012 data-taking period.
- Chapter 4 presents the strategies adopted during the analysis and the results achieved so far.
- Appendix A summarizes the ATLAS coordinate system convention, introducing the pseudorapidity.
- Appendix B lists the main algorithms used for the identification of jets originating from b quarks.
- Appendix C describes what a Monte Carlo simulation for hard processes consists of.
- Appendix D provides an overview of the Multivariate Analysis techniques, listing those we took into consideration for this analysis.

Both the CMS and our preliminary results show the data statistics collected during the Run-I is not sufficient; the rarity of this phenomenon requires more data to be gathered. The Run-II operations will supply this lack.

Theoretical background

This chapter illustrates the theoretical model that introduces the mechanism of spontaneous symmetry breaking, which leads to the existence of the Higgs boson. This particle is part of the Standard Model: the most complete and satisfying field theory that describes particle interactions.

We will provide a quick description of this theoretical framework before focusing on the Brout–Englert–Higgs mechanism. We will explain how spontaneous symmetry breaking occurs and how it leads to massive particles; we will show both Higgs boson production and decay channels; and eventually, the reasons behind the choice of the search this thesis is focused on.

1.1 The standard model

In the last century, the main focus of physics researches was to understand what the very-fundamental constituent of matter are and what forces rule the interactions between particles. In the attempt of testing theoretical predictions, experiments resulted in revolutionary discoveries that brought to the formulation of a comprehensive quantum field theory: the so-called Standard Model (SM) [13, 14, 15]¹.

The SM describes and treats physical systems by means of fields – i.e. functions defined in each point of ordinary spacetime – in a renormalizable, local, gauge invariant (under the internal symmetries of the unitary product group $\mathbf{U}(1) \otimes \mathbf{SU}(2) \otimes \mathbf{SU}(3)$) and covariant way. Moreover, it associates particles to the irreducible representations of the symmetry groups. According to this theory, only two kinds of particles exist in nature: fermions and bosons. The spin-statistic theorem guarantees the former obey

¹Salam, Weinberg and Glashow’s works were the first and main contributions that led to the Standard Model formulation. In 1979 these physicists were awarded jointly with the Nobel Prize in Physics “for their contributions to the theory of the unified weak and electromagnetic interaction between elementary particles, including, *inter alia*, the prediction of the weak neutral current” [16]. The first corroborations came from Gargamelle, UA1 and UA2 collaborations discoveries [17, 18, 19].

Fermi-Dirac statistics and are half-integer spin particles, the latter obey Bose-Einstein statistics and have integer-spin values. Moreover, the CPT theorem states every particle has an anti-particle with the same properties but opposite charges.

Particles interact by means of three forces – the electromagnetic, the weak and the strong interaction – due to the exchange of spin-1 particles: photon; W^\pm and Z^0 ; and eight gluons. The SM unifies the electromagnetic and the weak forces into a single framework – the standard electro-weak theory – but treats the strong interaction as a separate phenomenon.

Table 1.1 summarizes the main properties – electric charge and mass – of the spin-1/2 particles which constitute matter; table 1.2 illustrate how the six leptons and the six quarks are assembled into three families; table 1.3 gives an overview of the forces and their carriers.

Leptons		
Flavour	Charge [$e > 0$]	Mass [GeV]
e^-	-1	$(0.510998928 \pm 0.000000011) \times 10^{-3}$
ν_e	0	$< 2 \times 10^{-9}$
μ^-	-1	$(105.6583715 \pm 0.00000035) \times 10^{-3}$
ν_μ	0	$< 0.19 \times 10^{-3}$
τ^-	-1	1.77682 ± 0.00016
ν_τ	0	< 0.018

Quarks		
Flavour	Charge [$e > 0$]	Mass [GeV]
u	2/3	$2.3^{+0.7}_{-0.5} \times 10^{-3}$
d	-1/3	$4.8^{+0.5}_{-0.3} \times 10^{-3}$
c	2/3	1.275 ± 0.025
s	-1/3	$(95 \pm 5) \times 10^{-3}$
t	2/3	$173.21 \pm 0.51 \pm 0.71$
b	-1/3	4.18 ± 0.03

Table 1.1: Scheme of spin-1/2 particles that constitute matter: the six leptons – electron, muon, tau and the corresponding neutrinos –; and the six quarks – up, down, charm, strange, top (or truth) and bottom (or beauty). Data taken from references [20, 21, 7].

1.1.1 Electromagnetic interactions

Quantum Electro-Dynamics (QED) is the theoretical framework which fully describes how charged leptons (i.e. electrons, muons, taus and their anti-particles) interact with the electro-magnetic field. It schematizes the in-

	First family	Second family	Third family	
Leptons	$\begin{pmatrix} \nu_e \\ e^- \end{pmatrix}$	$\begin{pmatrix} \nu_\mu \\ \mu^- \end{pmatrix}$	$\begin{pmatrix} \nu_\tau \\ \tau^- \end{pmatrix}$	Matter
Quarks	$\begin{pmatrix} u \\ d \end{pmatrix}$	$\begin{pmatrix} c \\ s \end{pmatrix}$	$\begin{pmatrix} t \\ b \end{pmatrix}$	
Anti-Leptons	$\begin{pmatrix} \bar{\nu}_e \\ e^+ \end{pmatrix}$	$\begin{pmatrix} \bar{\nu}_\mu \\ \mu^+ \end{pmatrix}$	$\begin{pmatrix} \bar{\nu}_\tau \\ \tau^+ \end{pmatrix}$	Anti-matter
Anti-Quarks	$\begin{pmatrix} \bar{u} \\ \bar{d} \end{pmatrix}$	$\begin{pmatrix} \bar{c} \\ \bar{s} \end{pmatrix}$	$\begin{pmatrix} \bar{t} \\ \bar{b} \end{pmatrix}$	

Table 1.2: Overview of the very-fundamental constituent of matter and anti-matter, divided into the three families. Anti-matter particles have the same properties of their matter counterparts, but different charges (electric, hypercharge).

Interaction	Boson	Charge [$e > 0$]	Mass [GeV]
Electro-magnetic	γ	0	0
Weak	Z^0	0	91.1876 ± 0.0021
	W^\pm	± 1	80.385 ± 0.015
Strong	8 gluons	0	0

Table 1.3: Scheme of the three forces described by the Standard Model with the corresponding spin-1 gauge particles (the force carriers). Data taken from references [21, 7].

interaction through the exchange of a virtual photon γ , giving a complete account of matter and light coupling.

If the $e - \mu - \tau$ universality is satisfied (i.e. the coupling of leptons to gauge bosons is flavour-independent), this theory is gauge invariant under the local set of transformation of the $\mathbf{U}(1)$ group

$$\begin{aligned} e^f &\rightarrow e^{-iq\Lambda(x)}e^f \\ A^\mu &\rightarrow A^\mu + \partial^\mu\Lambda \end{aligned} \tag{1.1}$$

where: Λ is a real function of the spacetime coordinates; q is the coupling constant of the theory, which correspond to the charge of the lepton e^f ($= e, \mu, \tau$ for $f = 1, 2, 3$ respectively). The Lagrangian density that defines this system must be invariant with respect to the gauge transformation of equation 1.1. In order for this to be realized, the covariant derivative $D_\mu \equiv \partial_\mu + iqA_\mu$ must be introduced. This gives rise to the interaction term. Herefore, the Lagrangian is:

$$\mathcal{L}_{QED} = \sum_{f=1}^3 \bar{e}^f (i\gamma^\mu D_\mu - m)e^f - \frac{1}{2}(\partial_\mu A_\nu)(\partial^\mu A^\nu) \tag{1.2}$$

QED forbids a photon mass term ($\propto A_\mu^2$) in the Lagrangian density due to the gauge conditions of equation 1.1. Thus, it predicts a massless photon, consistently with non-covariant formulation and experimental results. The Lagrangian density of equation 1.2 consists of a sum of terms each of which involves one kind of lepton only. As a consequence, the Feynman diagrams that describe QED interactions have vertices with fermion lines referring to the same family. Hence, QED precludes reactions involving different kinds of lepton, such as

$$e^- + \mu^+ \rightarrow e^+ + \mu^- \tag{1.3}$$

Eventually, QED is a local theory: it describes only elementary particles, such as leptons. Instead, non-elementary particles, such as Hadrons (protons and neutrons for instance), have a definite radius. Being composed by color-charged elementary particles, only Quantum Chromodynamics (QCD) can describe their kinematics properly.

1.1.2 Weak interactions

In 1954 the physicists Chen-Ning Franklin Yang and Robert Laurence Mills developed a gauge theory based on the invariance with respect to a non-abelian group. The SM describes Weak interactions as invariant with respect to a set of transformations of the $\mathbf{SU}(2)$ group but treats them in analogy to QED.

Pioneering experiments [22] showed that weak interactions, unlike QED, violate parity symmetry. Thus, the SM treats differently the left and right components of Dirac spinors assigning the former to the doublet representation of $\mathbf{SU}(2)$ and the latter to the singlet (or scalar) one. It implies the

presence of three independent currents (one neutral and two charged) and, as experiments conducted in 1983 [17, 18, 23, 24] evidenced, the existence of three intermediate massive vector bosons – W^\pm and Z^0 –, whose interactions are described by three vector fields W_i^μ (with $i = 1, 2, 3$). Acting only on the left components of leptons, the neutral current W_3^μ has a chiral nature and envisages the production of neutrinos, therefore it is dissimilar from the electromagnetic current.

In the so-called electro-weak unification, the SM includes the QED current into its framework by adding an abelian factor and requiring the invariance with respect to a wider symmetry group. We should then introduce a new vector boson field, known as B_μ , that affect only the neutral current component, and impose invariance of the theory with respect to a set of transformations of the product group $\mathbf{U}(1) \otimes \mathbf{SU}(2)$.

$$\begin{aligned}
l_L^f &\equiv \begin{pmatrix} \nu^f \\ e^f \end{pmatrix}_L \rightarrow e^{ig\Lambda_i \frac{\tau_i}{2}} \begin{pmatrix} \nu^f \\ e^f \end{pmatrix}_L \\
e_R^f &\rightarrow e^f \\
l_L^f, e_R^f &\rightarrow e^{ig'\Lambda \frac{Y}{2}} l_L^f, e_R^f \\
W_i^\mu &\rightarrow W_i^\mu - g\epsilon_{ijk}\Lambda_j W_k^\mu + \partial^\mu \Lambda_i \\
B^\mu &\rightarrow B^\mu + \partial^\mu \Lambda
\end{aligned} \tag{1.4}$$

where g' and g are the coupling constants for $\mathbf{U}(1)$ and $\mathbf{SU}(2)$ respectively, τ_i the generators of weak interactions, i.e. the Pauli matrices, and Y the weak hypercharge.

The electro-weak symmetry breaking mechanism gives mass to the current mediators, leaving the photon a massless boson. However, this mechanism implies that the fields with a physical meaning and that acquire mass are a combination of W_i^μ and B^μ . Thus, we introduce the W_μ^\pm , Z_μ and A_μ fields for the weak and the QED currents:

$$\begin{aligned}
W_\mu^\pm &= \frac{1}{\sqrt{2}} (W_\mu^1 \mp i W_\mu^2) \\
Z_\mu &= -\sin \theta_W B_\mu + \cos \theta_W W_\mu^3 \\
A_\mu &= \cos \theta_W B_\mu + \sin \theta_W W_\mu^3
\end{aligned} \tag{1.5}$$

where θ_W is the weak angle, determined through experiments. We derive the weak gauge-invariant Lagrangian density, for fermion fields, that defines this theory as composed of three terms: a free propagation and two interaction

components.

$$\begin{aligned}
\mathcal{L}_0 &= \sum_{f=1}^3 \left[i \bar{l}_L^f \gamma^\mu \partial_\mu l_L^f + i \bar{e}_R^f \gamma^\mu \partial_\mu e_R^f \right] \\
\mathcal{L}_c &= \frac{g}{\sqrt{2}} \sum_{f=1}^3 \left[\bar{\nu}_L^f \gamma^\mu e_L^f W_\mu^+ + \bar{e}_L^f \gamma^\mu \nu_L^f W_\mu^- \right] \\
\mathcal{L}_n &= \bar{\Psi} \gamma^\mu \left[g \sin \theta_W T^3 + g' \frac{Y}{2} \cos \theta_W \right] \Psi A_\mu + \\
&\quad + \bar{\Psi} \gamma^\mu \left[g \cos \theta_W T^3 - g' \frac{Y}{2} \sin \theta_W \right] \Psi Z_\mu
\end{aligned} \tag{1.6}$$

where Ψ , introduced in the neutral term, is a column vector formed with all left-handed and right-handed fermions in the theory:

$$\Psi \equiv \begin{pmatrix} \nu_L^f \\ e_L^f \\ \nu_R^f \\ e_R^f \end{pmatrix} \tag{1.7}$$

However, the experiments themselves raised an issue: weak interactions have short range and thus intermediate vector bosons are massive while gauge theories require massless mediators. Moreover, charged leptons have non-negligible masses but the electro-weak Lagrangian density does not show a mass term for them, due to the gauge invariance. The Brout-Englert-Higgs mechanism solves this issue.

Electro-weak interactions for quarks

Quarks have an electric charge and are associated to non-trivial representations of the $\mathbf{SU}(2)$ group; thus, being coupled to both the photon and the weak bosons, they interact through the electro-weak force. Their confinement nature made them hard to be accepted when in 1964 the american physicists Murray Gell-Mann [25] and George Zweig [26] proposed, independently, a quark model able to describe the hadrons zoology of that time. This model included the only three quarks they knew of: up, down and strange. But experimental discoveries evidenced the presence of new hadrons not explainable with this quark model: only in 1970 the physicists S. Glashow, J. Iliopoulos and L. Maiani suggested (GIM mechanism [27]) to include a new quark, i.e. the charm quark – whose existence was confirmed in 1974 thanks to the J/ψ discovery [28, 29]. In order to include the new findings, physicists formulated modified quark models such as the *Constituent Quark Model* (CQM) and the *Isgur and Karl model* [30, 31, 32]. The SM now implies the existence of at least six quark flavours, which have all been discovered.

Weak interactions allow a mixing phenomenon between quarks of different flavours: in 1973 Makoto Kobayashi and Toshihide Maskawa [34] introduced the CKM matrix V_{fg} – an extension of the GIM mechanism,

and f labels the quark family ($u^f = u, c, t$ and $d^f = d, s, b$ for $f = 1, 2, 3$). The Lagrangian density that defines this environment is an extension of the Lagrangian density of equation 1.6

$$\begin{aligned}
\mathcal{L}_0 &= \sum_{f=1}^3 \left[i \bar{l}_L^f \gamma^\mu \partial_\mu l_L^f + i \bar{e}_R^f \gamma^\mu \partial_\mu e_R^f + \right. \\
&\quad \left. + i \bar{q}_L^f \gamma^\mu \partial_\mu q_L^f + i \bar{u}_R^f \gamma^\mu \partial_\mu u_R^f + i \bar{d}_R^f \gamma^\mu \partial_\mu d_R^f \right] \\
\mathcal{L}_c &= \frac{g}{\sqrt{2}} \left[\sum_{f=1}^3 \bar{\nu}_L^f \gamma^\mu e_L^f + \sum_{f,g=1}^3 \bar{u}_L^f \gamma^\mu V_{fg} d_L^g \right] W_\mu^+ + \\
&\quad + \frac{g}{\sqrt{2}} \left[\sum_{f=1}^3 \bar{e}_L^f \gamma^\mu \nu_L^f + \sum_{f,g=1}^3 \bar{d}_L^f \gamma^\mu V_{fg}^* u_L^g \right] W_\mu^- \\
\mathcal{L}_n &= \bar{\Psi} \gamma^\mu \left[g \sin \theta_W T^3 + g' \frac{Y}{2} \cos \theta_W \right] \Psi A_\mu + \\
&\quad + \bar{\Psi} \gamma^\mu \left[g \cos \theta_W T^3 - g' \frac{Y}{2} \sin \theta_W \right] \Psi Z_\mu
\end{aligned} \tag{1.10}$$

where Ψ now includes the left components of quarks too.

1.1.3 Strong interactions

Strong force affects particles with a color charge: the quarks and the eight color-charged gluons, the force carriers. The gauge theory that describes quark dynamics is Quantum ChromoDynamics (QCD). Based on the Yang-Mills theory, it treats strong forces as invariant with respect to a set of transformation of the $\mathbf{SU}(3)$ group.

We introduce eight gauge fields A_i^μ and define six Dirac fields Ψ^f (with $f = u, d, s, c, b, t$) as composed of three component fields, one for each color (r, g, b). Instead of the three Pauli matrices in the $\mathbf{SU}(2)$ case, it is the eight Gell-Mann matrices λ that act as generators of $\mathbf{SU}(3)$. Thus, the theory is invariant with respect to the local transformation

$$\Psi^f \rightarrow e^{i g_s \Lambda_i \frac{\lambda_i}{2}} \Psi^f \tag{1.11}$$

$$A_i^\mu \rightarrow A_i^\mu - g_s f_{ijk} \Lambda_j A_k^\mu + \partial^\mu \Lambda_i$$

where: g_s is the strong coupling constant; f_{ijk} are the total antisymmetric structure constants; and Λ_i are real local functions of the spacetime coordinate, small enough to ensure the validity of perturbation theory. Table 1.4 reports the f_{ijk} values for different ijk configurations.

We include the interaction gluon-quark term in the covariant derivative D_μ^2 , and introduce the gauge fields $G_i^{\mu\nu} \equiv \partial^\nu A_i^\mu - \partial^\mu A_i^\nu + g_s f_{ijk} A_j^\mu A_k^\nu$. The Lagrangian density that defines this theory is

$$\mathcal{L}_{QCD} = \sum_{f=1}^3 \bar{\Psi}^f (i \gamma^\mu D_\mu - m_f) \Psi^f - \frac{1}{4} G_{i\mu\nu} G_i^{\mu\nu} \tag{1.12}$$

²In strong interactions the covariant derivative is defined as $D_\mu \equiv \partial_\mu + i g_s \frac{\lambda_i}{2} A_\mu^i$

ijk	123	147	156	246	257	345	367	458	678
f_{ijk}	1	$\frac{1}{2}$	$-\frac{1}{2}$	$\frac{1}{2}$	$\frac{1}{2}$	$\frac{1}{2}$	$-\frac{1}{2}$	$\frac{\sqrt{3}}{2}$	$\frac{\sqrt{3}}{2}$

Table 1.4: Values of the completely antisymmetric structure constant f_{ijk} for different ijk combinations. Data taken from reference [36].

1.2 Spontaneous symmetry breaking

Experiments [17, 18, 23, 24] demonstrated the electro-weak bosons W^\pm and Z^0 , as well as charged leptons, are massive particles. However, gauge theories require massless mediators and fermions. Due to the chiral nature of the weak interactions, Dirac mass terms lack gauge invariance: these are proportional to

$$\bar{e}^f e^f = \bar{e}_L^f e_R^f + \bar{e}_R^f e_L^f \quad (1.13)$$

but left- and right-handed components transform in different ways under an $\mathbf{SU}(2)$ transformation. This implies the existence of another mechanism through which particles acquire mass.

This issue puzzled physicists for many years. Until 1961-1962 when the theoretical physicist Jeffrey Goldstone proposed a new model in which particles acquire mass through a mechanism of spontaneous symmetry breaking [37, 38]. This concept, first suggested by Yoichiro Nambu during his studies about superconductivity and ferromagnetism [39], states spontaneous symmetry breaking occurs when a system – with a definite symmetry invariance – has a degenerate ground state; the arbitrary choice of the fundamental configuration produces the asymmetry.

1.2.1 The Brout-Englert-Higgs mechanism

Goldstone took Nambu concept and developed a field theory – invariant under a $\mathbf{SU}(2)$ gauge transformation – that exhibits this behaviour. Robert Brout, François Englert and Peter Higgs generalized this theory to be invariant under a $\mathbf{U}(1)$ gauge transformation [40, 41, 42]. The modern standard electroweak theory is invariant under a $\mathbf{U}(1) \otimes \mathbf{SU}(2)$ gauge transformation.

The Brout-Englert-Higgs mechanism presents a scalar field whose potential has its minimum translated from the origin of the isotopic space (reported on figure 1.2). As a consequence, the ground state – characterized by the non vanishing vacuum expectation value – doesn't show all the symmetries the Lagrangian has. Assigned the scalar field ϕ to the doublet representation of the non-abelian $\mathbf{SU}(2)$ group, the minimum of the potential lies in $\phi_0 = v/\sqrt{2}$ – where v is a constant. This theory imposes the invariance with respect to the set of transformations of the gauge $\mathbf{U}(1) \otimes \mathbf{SU}(2)$ product group

$$\begin{aligned} \phi + \phi_0 &\rightarrow e^{ig\Lambda_i \frac{\tau^i}{2}} (\phi + \phi_0) \\ \phi + \phi_0 &\rightarrow e^{ig'\Lambda^Y \frac{Y}{2}} (\phi + \phi_0) \end{aligned} \quad (1.14)$$

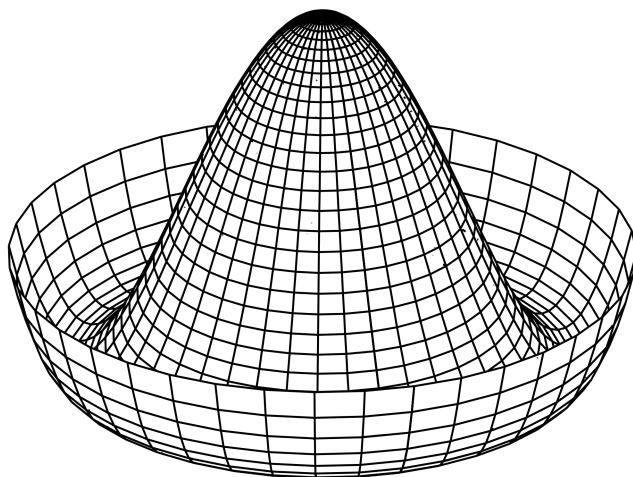


Figure 1.2: The Higgs potential: $\mathcal{V} = \mu^2|\phi|^2 + \lambda|\phi|^4$. With $\mu^2 < 0$ and $\lambda > 0$ the spontaneous symmetry breaking occurs. The minimum of the potential \mathcal{V} lies in a circle $\phi_0 = e^{i\alpha\theta}v/\sqrt{2}$ (where v is an $\mathbf{SU}(2)$ doublet constant with $|v| = \sqrt{-\mu^2/\lambda}$): the vacuum state is chosen so that $\phi_0 = v/\sqrt{2}$, thus breaking the symmetry.

The SM expects the symmetry breaking to occur in three of the four dimensions on the $\mathbf{U}(1) \otimes \mathbf{SU}(2)$ gauge group without affecting the electrodynamics sub-group $\mathbf{U}_{em}(1)$. The absence of a massive photon is assured by the condition

$$\phi_0 \rightarrow e^{ie\alpha Q} \phi_0 \quad (1.15)$$

where the charge $Q = T_3 + Y/2$. This system has two non-trivial solutions: the first one requires $Y = +1$, the second one requires $Y = -1$. As custom, we choose the first solution.

Being assigned to the doublet representation of the $\mathbf{SU}(2)$ group, the ϕ field is composed by two complex fields: ϕ^0 and ϕ^+ . Several parametrizations exist. These see each complex scalar field as composed by two real scalar fields – thus introducing the Higgs and the Goldstone bosons. The latter represents unphysical degrees of freedom and give mass to the W^\pm and Z^0 fields.

$$\phi + \phi_0 = \frac{1}{\sqrt{2}} e^{i\tau^i \frac{\theta^i}{v}} \begin{pmatrix} 0 \\ v + H \end{pmatrix} \quad (1.16)$$

The phase factor in equation 1.16 contains these non-physical degrees of freedom and H is the Higgs boson. The former disappears using a suitable $\mathbf{SU}(2)$ gauge transformation, the so-called *unitary gauge*. The advantage of this choice is the Goldstone bosons disappear, while both the Higgs and the gauge bosons acquire mass. In this gauge, the Higgs Lagrangian density appears as

$$\begin{aligned} \mathcal{L}_H = \frac{1}{2} \partial^\mu H \partial_\mu H + \left[\frac{1}{4} g^2 W^{\mu+} W_\mu^- + \frac{1}{8} (g^2 + g'^2) Z^\mu Z_\mu \right] (H + v)^2 + \\ + \frac{1}{2} (2\lambda v^2) H^2 + \lambda v H^3 + \frac{1}{4} \lambda H^4 \quad (1.17) \end{aligned}$$

The quadratic parts in the fields produce the mass terms for both the Higgs boson and the intermediate vector bosons. These are functions of the coupling constant, g and g' , λ and v :

$$\begin{aligned} m_H^2 &= 2\lambda v^2 \\ m_W^2 &= \frac{1}{4} g^2 v^2 \quad m_Z^2 = \frac{1}{4} (g^2 + g'^2) v^2 \end{aligned} \quad (1.18)$$

1.2.2 Quark and lepton masses

The gauge symmetries of the SM forbid mass terms for fermions: the chiral nature of spinors makes Dirac mass terms of equation 1.13 not invariant under an $\mathbf{SU}(2)$ transformation. However, both quarks and leptons acquire mass via the Brout-Englert-Higgs mechanism, through a Yukawa coupling: the interaction between two fermions and a boson – the leptons/quarks and the Higgs boson. The resulting Lagrangian densities add mass terms in the SM.

One should introduce three generic 3×3 complex matrices, y_u^f , y_d^f and y_e^f . They represent the Yukawa coupling strengths. However, the Yukawa mass terms – in the form of $\bar{l}_L^f (\phi + \phi_0) y_e^f e_R^f + h.c.$ – are not diagonal in the fields, but a bi-unitary transformation can diagonalize them. Thus, introducing the six unitary matrices $V_{R,L}^{U,D,E}$, we obtain three diagonal matrices h_u^f , h_d^f and h_e^f – with real and non-negative entries – defined as

$$\begin{aligned} h_e^f &\equiv V_L^{E\dagger} y_e^f V_R^E \\ h_u^f &\equiv V_L^{U\dagger} y_u^f V_R^U \\ h_d^f &\equiv V_L^{D\dagger} y_d^f V_R^D \end{aligned} \quad (1.19)$$

This diagonalization process induces a new definition of the fields. Thus, we rotate them in such a way they bring the Yukawa interaction term in diagonal form:

$$\begin{aligned} \tilde{e}_{L,R}^f &\equiv V_{L,R}^E e_{L,R}^f \\ \tilde{u}_{L,R}^f &\equiv V_{L,R}^U u_{L,R}^f \\ \tilde{d}_{L,R}^f &\equiv V_{L,R}^D d_{L,R}^f \end{aligned} \quad (1.20)$$

This leads to Lagrangian terms in which we can identify the corresponding quark and lepton mass terms. In the *unitary gauge* these are

$$\begin{aligned}\mathcal{L}_Y^{lept} &= -\frac{1}{\sqrt{2}}(v + H) \sum_{f=1}^3 h_e^f \bar{e}^f e^f \\ \mathcal{L}_Y^{quark} &= -\frac{1}{\sqrt{2}}(v + H) \sum_{f=1}^3 \left(h_u^f \bar{u}^f u^f + h_d^f \bar{d}^f d^f \right)\end{aligned}\tag{1.21}$$

These rotations influence the other SM Lagrangian terms, leaving unchanged those diagonal in the fields. The neutral-current interaction Lagrangian remain unchanged, due to the universality of the fermion couplings to the photon and to the Z^0 boson. However, the quark Lagrangian in equation 1.21 affect the charged-current interaction Lagrangian while the leptonic Lagrangian leaves it unchanged.

This different behaviour is due to the absence of right-handed neutrinos. Being massless, they can undergo the same rotations as the charged leptons leaving the \mathcal{L}_c Lagrangian untouched. As a consequence, in the SM with massless neutrinos, leptons have no mixing among different generations and the mass eigenstates coincide with the interaction eigenstates. On the other hand, the up and down components of the same left-handed doublet transforms in different ways – V_L^U and V_L^D are different matrices – and this causes a change in the \mathcal{L}_c Lagrangian. Moreover, we can express the unitary matrix $V_L^{U\dagger} V_L^D$ as a single one: the Cabibbo-Kobayashi-Maskawa matrix V_{CKM} (equation 1.8).

The corresponding quark and lepton masses are functions of the Yukawa coupling matrices and v . Table 1.1 reports the experimental mass values.

$$\begin{aligned}m_e^f &= \frac{1}{\sqrt{2}} v h_e^f \\ m_u^f &= \frac{1}{\sqrt{2}} v h_u^f \quad m_d^f = \frac{1}{\sqrt{2}} v h_d^f\end{aligned}\tag{1.22}$$

1.3 The standard electroweak Lagrangian

We can now summarize the standard electro-weak Lagrangian density and schematize it as composed by seven terms – each Lorentz invariant and possessing a $\mathbf{U}(1) \otimes \mathbf{SU}(2)$ group gauge symmetry. These Lagrangian terms are namely:

- Free Lagrangian for matter fermions

$$\begin{aligned}\mathcal{L}_0^F &= \sum_{f=1}^3 \left[\bar{\nu}^f i\gamma^\mu \partial_\mu \nu^f + \bar{e}^f (i\gamma^\mu \partial_\mu - m_e^f) e^f + \right. \\ &\quad \left. + \bar{u}^f (i\gamma^\mu \partial_\mu - m_u^f) u^f + \bar{d}^f (i\gamma^\mu \partial_\mu - m_d^f) d^f \right]\end{aligned}\tag{1.23}$$

- Free Lagrangian for gauge and Higgs bosons

$$\mathcal{L}_0^G = -\frac{1}{4}Z_{\mu\nu}Z^{\mu\nu} + \frac{1}{2}m_Z^2 Z^\mu Z_\mu - \frac{1}{2}W_{\mu\nu}^+ W^{\mu\nu-} + m_W^2 W^{\mu+} W_\mu^- +$$

$$-\frac{1}{2}\partial_\mu A_\nu \partial^\mu A^\nu + \frac{1}{2}\partial^\mu H \partial_\mu H - \frac{1}{2}m_H^2 H^2 \quad (1.24)$$

- Electromagnetic coupling

$$\mathcal{L}_{em} = e \sum_{f=1}^3 \left(-\bar{e}^f \gamma^\mu e^f + \frac{2}{3}\bar{u}^f \gamma^\mu u^f - \frac{1}{3}\bar{d}^f \gamma^\mu d^f \right) A_\mu \quad (1.25)$$

- Charged-current interaction

$$\mathcal{L}_c = \frac{g}{2\sqrt{2}} \left[\sum_{f=1}^3 \bar{\nu}^f \gamma^\mu (1 - \gamma_5) e^f + \sum_{f,g=1}^3 \bar{u}^f \gamma^\mu (1 - \gamma_5) V_{fg} d^g \right] W_\mu^+ +$$

$$+ \frac{g}{2\sqrt{2}} \left[\sum_{f=1}^3 \bar{e}^f \gamma^\mu (1 - \gamma_5) \nu^f + \sum_{f,g=1}^3 \bar{d}^g \gamma^\mu (1 - \gamma_5) V_{fg}^* u^f \right] W_\mu^- \quad (1.26)$$

- Neutral-current interaction

$$\mathcal{L}_n = \frac{e}{4 \cos \theta_W \sin \theta_W} \sum_{f=1}^3 \left[\bar{\nu}^f \gamma^\mu (1 - \gamma_5) \nu^f + \right.$$

$$+ \bar{e}^f \gamma^\mu (-1 + 4 \sin^2 \theta_W + \gamma_5) e^f + \bar{u}^f \gamma^\mu (1 - \frac{8}{3} \sin^2 \theta_W - \gamma_5) u^f +$$

$$\left. + \bar{d}^f \gamma^\mu (-1 + \frac{4}{3} \sin^2 \theta_W + \gamma_5) d^f \right] Z_\mu \quad (1.27)$$

- Vector-boson self-interaction

$$\mathcal{L}_V = ig \sin \theta_W (W_{\mu\nu}^+ W_\nu^\mu A^\nu - W_{\mu\nu}^- W_\nu^\mu A^\nu + F_{\mu\nu} W_\nu^\mu W_\nu^-) +$$

$$+ ig \cos \theta_W (W_{\mu\nu}^+ W_\nu^\mu Z^\nu - W_{\mu\nu}^- W_\nu^\mu Z^\nu + Z_{\mu\nu} W_\nu^\mu W_\nu^-) +$$

$$+ \frac{g}{2} (2g^{\mu\nu} g^{\rho\sigma} - g^{\mu\rho} g^{\nu\sigma} - g^{\mu\sigma} g^{\nu\rho}) \left[\frac{1}{2} W_\mu^+ W_\nu^+ W_\rho^- W_\sigma^- + \right.$$

$$\left. - W_\mu^+ W_\nu^+ (A_\rho A_\sigma \sin^2 \theta_W + Z_\rho Z_\sigma \cos^2 \theta_W + 2A_\rho Z_\sigma \sin \theta_W \cos \theta_W) \right] \quad (1.28)$$

- Higgs interaction

$$\mathcal{L}_H = \left(m_W^2 W^{\mu+} W_\mu^- + \frac{1}{2} m_Z^2 Z^\mu Z_\mu \right) \left(\frac{H^2}{v^2} + \frac{2H}{v} \right) +$$

$$- \frac{H}{v} \sum_{f=1}^3 \left(m_d^f \bar{d}^f d^f + m_u^f \bar{u}^f u^f + m_e^f \bar{e}^f e^f \right) - \lambda v H^3 - \frac{1}{4} \lambda H^4 \quad (1.29)$$

1.4 The Higgs boson search

Before LHC, Higgs boson searches were conducted at LEP II at CERN (Switzerland/France) [43] and at Tevatron at Fermilab (Illinois – USA) [44], reaching a center of mass energy of $\sqrt{S} = 208$ GeV and $\sqrt{S} = 1$ TeV respectively. The former, relying on electron-positron collisions, focused on the Higgs-strahlung mechanism; the latter, relying on proton-proton collisions, focused on the Higgs production associated with hadron states X :

$$e^+ + e^- \rightarrow H + Z^0$$

$$p + \bar{p} \rightarrow H + X$$
(1.30)

None of them found an evidence of a new particle existence. LEP collected a total of 2461 pb^{-1} of e^+e^- collision data and defined an Higgs mass lower bound of 114.4 GeV. Tevatron excluded the Higgs boson mass range between 147 GeV and 180 GeV and found an excess of events that could be from a Higgs boson in the range 115–140 GeV – however, the significance of the statistics was too low to base any conclusions on. Latest experiments at LHC exploited proton-proton collisions at a center of mass energy of $\sqrt{S} = 8$ TeV. In 2012 the ATLAS³ and CMS⁴ collaborations discovered the Higgs boson [1, 2], with a mass value of 125.7 ± 0.4 GeV [7].

However, the theoretical framework allowed a precise calculation of cross sections, decay rates, branching ratios and couplings long before the boson discovery. Figures 1.3 and 1.5 show the Higgs cross section and branching ratio, as functions of the Higgs mass at this energy. Figures 1.4 and 1.6 summarize the corresponding Feynman diagrams.

$\sqrt{S} = 8$ TeV			
m_H [GeV]	σ_{VBF} [pb]	σ_{gF} [pb]	$\mathcal{BR}(H \rightarrow bb)$
115	$1.729^{+2.5\%}_{-2.8\%}$	$22.66^{+10.61\%}_{-10.58\%}$	$0.703^{+2.40\%}_{-2.46\%}$
120	$1.649^{+2.6\%}_{-2.8\%}$	$20.86^{+10.47\%}_{-10.49\%}$	$0.648^{+2.76\%}_{-2.83\%}$
125	$1.578^{+2.6\%}_{-2.8\%}$	$19.27^{+10.40\%}_{-10.41\%}$	$0.577^{+3.21\%}_{-3.27\%}$
130	$1.511^{+2.6\%}_{-2.7\%}$	$17.85^{+10.33\%}_{-10.34\%}$	$0.494^{+3.71\%}_{-3.78\%}$

Table 1.5: Cross sections and breaking ration for different Higgs mass values and at a center of mass energy of $\sqrt{S} = 8$ TeV. Data taken from references [8, 9].

This thesis is imprinted towards the search for a Vector Boson Fusion-produced Higgs boson decaying to a $b\bar{b}$ quark pair. The VBF process has the second largest Higgs production cross-section and very small additional

³<http://atlas.web.cern.ch>

⁴<http://cms.web.cern.ch>

hadronic activity in the central rapidity region due to the suppression of gluon radiation, but it presents a large QCD background with the consequent low signal sensitivity. Together with the predominance of the $b\bar{b}$ decay channel, the clear event topology (2 hard-scattered forward jets and the Higgs decay products in the central region) leads to this production channel choice.

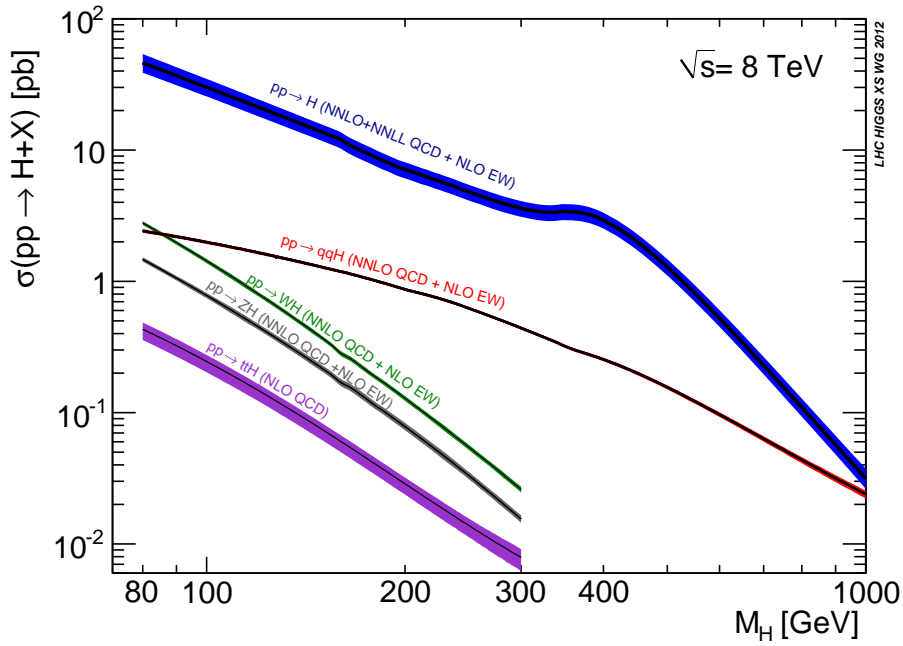


Figure 1.3: The Standard Model Higgs boson production cross sections at $\sqrt{s} = 8$ TeV for different Higgs mass values. Figure supplied by the Higgs Cross Section Working Group <https://twiki.cern.ch/twiki/bin/view/LHCPhysics/CrossSections>.

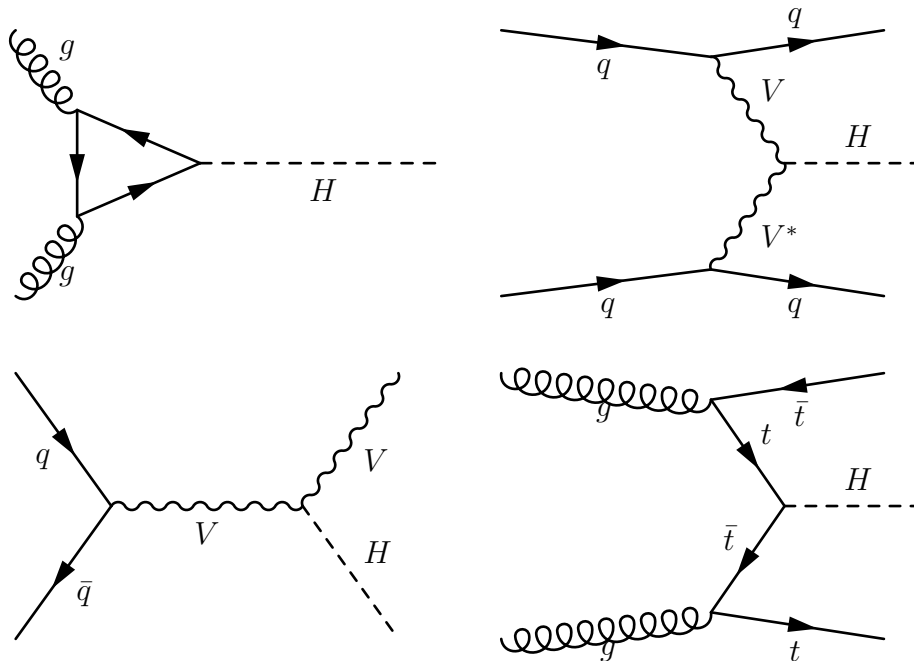


Figure 1.4: The Feynman diagrams representing the different production channels for the Higgs boson in proton-proton collision: gluon Fusion, Vector Boson Fusion, associate production with a intermediate vector boson and the associate production with a top pair.

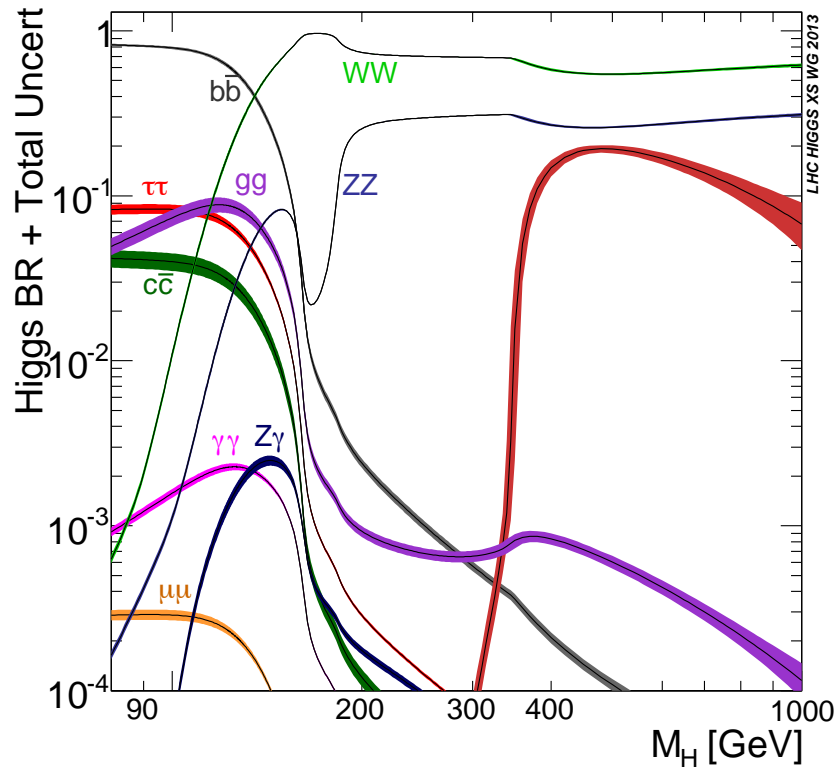


Figure 1.5: The Standard Model Higgs boson decay branching ratios for different Higgs mass values. Figure supplied by the LHC Higgs Cross Section Working Group <https://twiki.cern.ch/twiki/bin/view/LHCPhysics/CrossSections>.

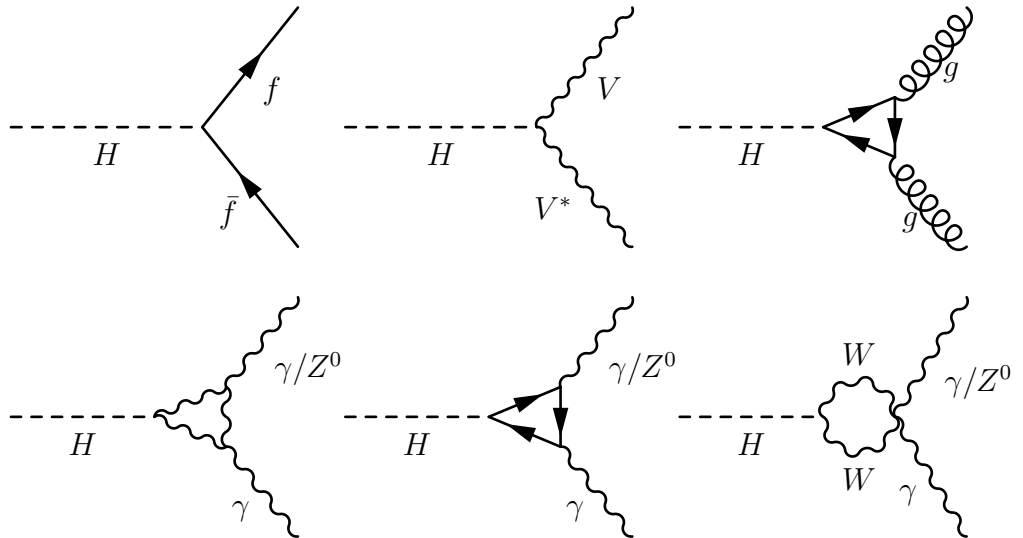


Figure 1.6: The Feynman diagrams representing the Higgs boson decay channels at lowest orders: production of a $f\bar{f}$ pair ($f = b, \tau, c, \mu$), production of a weak vector boson pair, production of a gluon pair, and production of a $\gamma\gamma$ or a γZ^0 pair.

The ATLAS experiment

This chapter provides a comprehensive overview of both the Large Hadron Collider and ATLAS – the experiment that, together with CMS, discovered the Higgs boson.

We will explain what the journey of the protons consists of, from their source to the ATLAS detector. Hence, we will discuss the details of the experimental apparatus: the sub-detectors and the trigger system. Eventually, we will provide a swift summary of LHC operations since its completion in 2008, to the Higgs boson discovery in 2012 and the forthcoming Run-II data taking period of 2015.

2.1 The Large Hadron Collider

The engines used for High Energy Physics investigations are colliders: particle accelerators that rely on collisions between beams of particles for their searches. The Large Hadron Collider (LHC) [45] reaches the world’s highest center of mass energy and luminosity; thus it represents the new frontier for physics experiments. Built from 2000 to 2008 by the CERN – the “*European Council for Nuclear Research*” (“*Conseil Européen pour la Recherche Nucléaire*”), i.e. a provisional council established by 12 European governments in 1952 –, it is situated in Geneva on the Franco-Swiss border, with a sloping towards the Léman lake. This two-ring-superconducting-hadron accelerator, installed in the already existing Large Electron-Positron Collider (LEP) tunnel, accelerates particles using twin-bore magnets, thus magnetically coupling the two rings. The counter-rotating beams collide in four interaction points, equipped with underground caverns where the main experiments stand.

LHC is a proton-proton collider. A complex of accelerating engines constitutes the injector chain. It boosts progressively two proton beams: from the source, a simple hydrogen gas cylinder, to the Large Hadron Collider. Many high intensity proton bunches constitute the resulting beams, with small transverse and well defined longitudinal emittances. In sequence, we find:

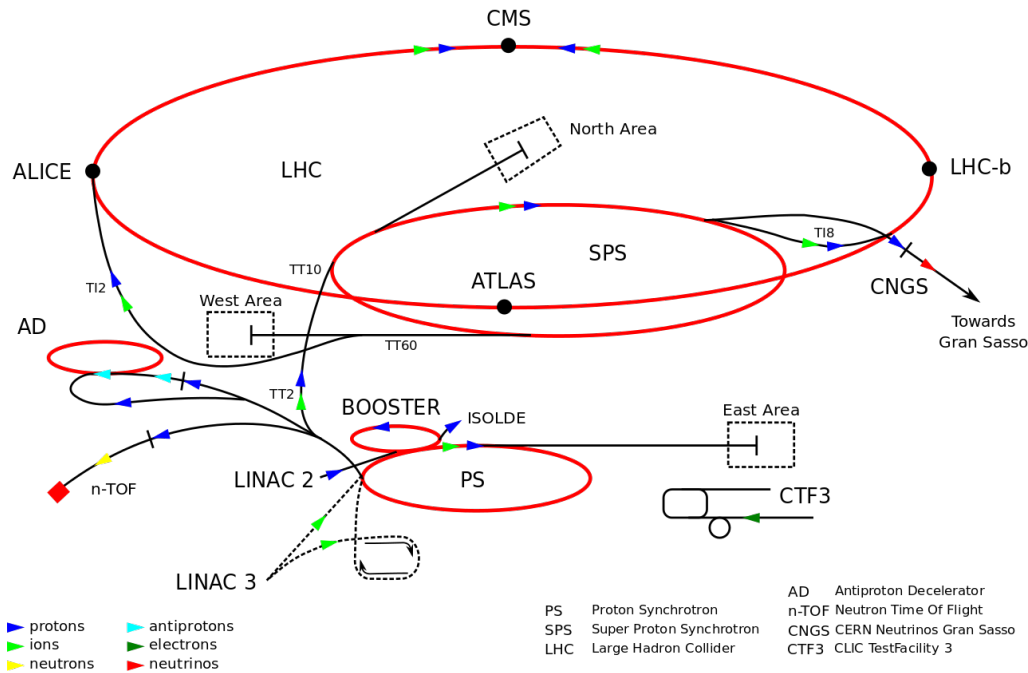


Figure 2.1: A schematic of accelerator complex at CERN. Protons are accelerated by Linac, Booster, Proton Synchrotron (PS) and Super Proton Synchrotron (SPS). Protons are then guided into the LHC ring into two separated pipes, and eventually they collide where experiments are located. The LHC Technical Reports, in three volumes, are reported in references [46, 47, 48]

- **Linac2**, a 50 MeV Alvarez Proton Linac. Operating since 1978, when it took the place of Linac1, it will be replaced in 2017 or 2018 by Linac4, which will accelerate particles up to 160 MeV.
- **The Proton Synchrotron Booster (PSB)**: made up of four super-imposed synchrotron rings, it accelerates the 50 MeV protons injected from Linac2 to 1.4 GeV for injection into the Proton Synchrotron.
- **The Proton Synchrotron (PS)**: built in 1959, it is a 628 metres long synchrotron. It accelerates the protons delivered by the Proton Synchrotron Booster up to 25 GeV and operates as a feeder to the Super Proton Synchrotron.
- **The Super Proton Synchrotron (SPS)**: it is a synchrotron measuring nearly 7 kilometres in circumference and operating at 450 GeV. It works since 1976 (at that time it boosted particle up to 300 GeV) and takes particles from the Proton Synchrotron, accelerating them to directly provide beams for the Large Hadron Collider.
- **The Large Hadron Collider (LHC)**: it is a 27-kilometres long ring-shaped accelerator composed by superconducting magnets and accelerating structures built in a tunnel about 100 metres underground, originally used for hosting LEP. Particle beams can circulate into two separate vacuum pipes, both in clockwise and counter-clockwise direction. The two beams are brought into collision inside four detectors.

At the current moment, the maximum total energy reached at the collision point is equal to $\sqrt{S} = 8$ TeV.

The CERN accelerator complex includes other engines: the linear accelerator Linac3, which provides lead ions to the PSB; the Antiproton Decelerator (AD), used for antimatter-related experiments; the Online Isotope Mass Separator (ISOLDE) facility, dedicated to the production of a large variety of radioactive ion beams; the CERN Neutrinos to Gran Sasso (CNGS) project, for investigating the neutrinos oscillations; and the neutron time-of-flight facility (nTOF), for neutron-nucleus interactions studies. The experiments cover a wide range of physics topics, such as anti-matter related studies, neutrino, neutron and heavy Ions physics.

The biggest collaborations take data directly from collisions in the LHC ring. These are namely:

- **A Large Ion Collider Experiment (ALICE)**: Experiment focusing on strongly interacting matter by means of Pb-Pb nuclei collisions. Its main focus is quark-gluon plasma-related studies in order to understand color confinement and chiral symmetry restoration.
- **A Toroidal LHC Apparatus (ATLAS) and Compact Muon Solenoid (CMS)**: Multi-purpose experiments. their main goals cover different topics: Higgs boson search, CP violation, top quark properties, SUSY, and dark matter.
- **Large Hadron Collider beauty (LHCb)**: Experiment specialized in bottom quark-related physics in order to measure the parameters of CP violation and find rare phenomena regarding B hadrons.

At the present moment, the LHC ring is going through a two-years shutdown period in order to upgrade the center of mass energy to $\sqrt{S} = 14$ TeV for the three-year long Run-II operations beginning in 2015.

2.2 The ATLAS Experiment

ATLAS [49, 50] is a general-purpose experiment set in point 1 of the LHC tunnel. Proposed in 1994, it was funded in 1995 and completed in 2008. Now it includes over 3000 physicists from over 175 institutions in 38 countries. With a length of 46 metres, a diameter of 25 metres and a weight of about 7000 tonnes, it is the biggest experiment in the LHC ring.

Built to probe proton-proton collisions, the physics programme it covers is broad. Rarity and low cross sections characterizes the physics phenomena studied. The peculiar experimental conditions – high center of mass energy, interaction rate and luminosity – require the detector to satisfy different requirements in order to ensure good performance:

- Fast and radiation-hard electronics and high detector granularity to handle the particle fluxes and reduce the influence of overlapping events (pile-up).

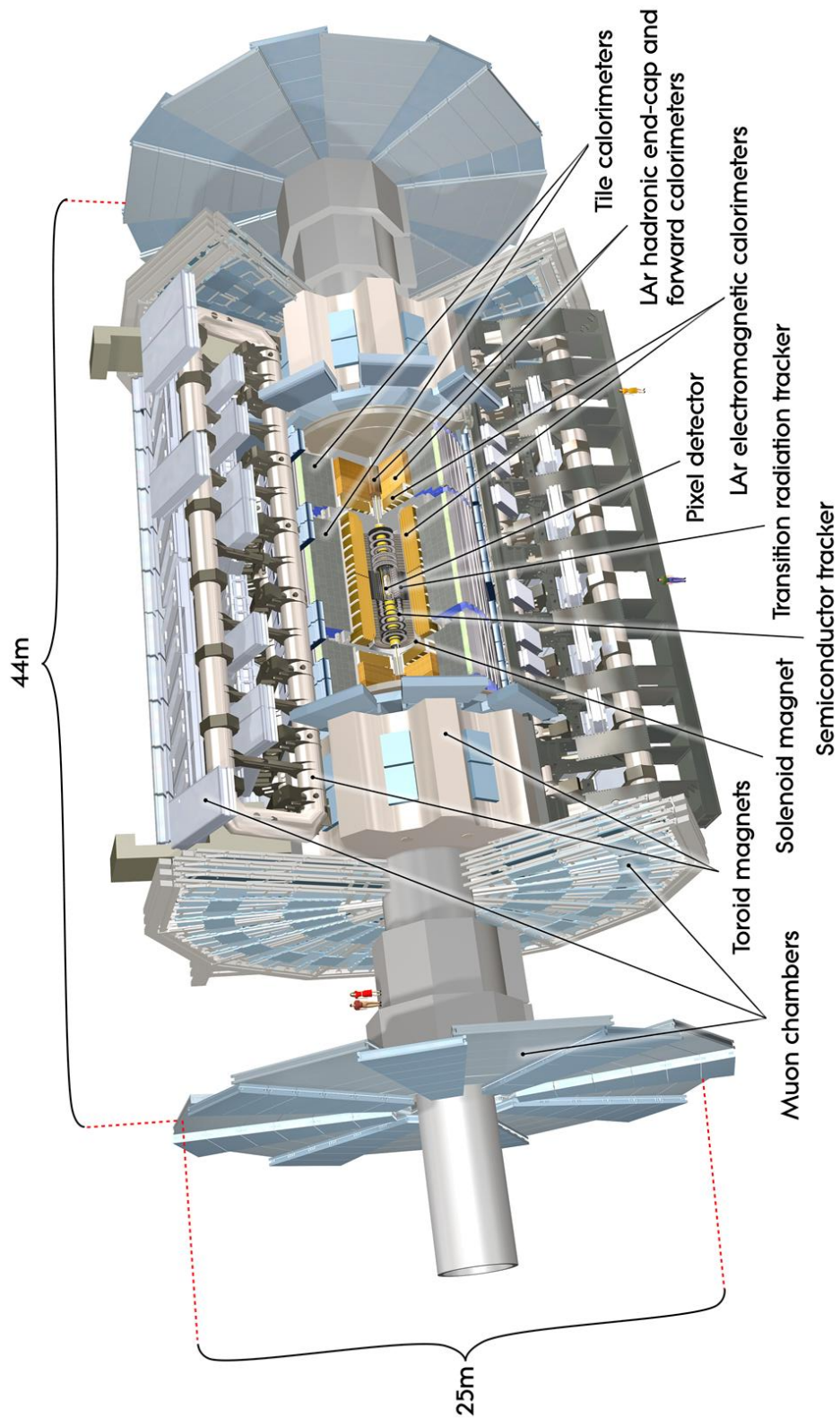


Figure 2.2: A detailed computer-generated image of the ATLAS detector and its systems. Figure taken from <http://www.atlas.ch/photos/index.html>

- Large angular coverage, both in pseudorapidity and azimuthal angle, to reconstruct the events.
- Charged-particle momentum resolution and reconstruction efficiency, together with the capability to identify secondary vertices and tag jets stemming from the hadronization of b quarks and τ leptons.
- Good electromagnetic calorimeter, for electron and photon identification and measurements. Moreover, a full-coverage hadronic calorimeter, for accurate measurements of jet energy and missing transverse energy.
- Accurate muons identification and momentum resolution over a wide range of momenta, and unambiguous determination of the charge of high transverse momentum muons.
- Flexible and efficient trigger system to select interesting physics events while rejecting most of the background processes.

Divided into a barrel section and two end-caps, ATLAS possesses a forward-backward symmetry with respect to the interaction point. It consists of several highly granular and hermetic sub-detectors: the Inner Detector, the Calorimeter, and the Muon Spectrometer. These are concentric layers oriented coaxially with respect to the beam line and centered around the nominal interaction point. A thin superconducting solenoid (surrounding the Inner-Detector cavity), together with three large superconducting toroids (around the calorimeters), constitute the magnet system.

The Inner Detector is immersed in a 2 T solenoidal field. It is composed of three distinct sub-detector: high-resolution semiconductor pixel and strip detectors, and a detector based on straw tubes exploiting the transition radiation mechanism. They provide pattern recognition, momentum and vertex measurements, and electron identification of charged tracks. Outwards, the calorimeter system is composed by a high granularity liquid-argon electromagnetic sampling calorimeter and a scintillator-tile hadronic calorimeter. The Muon Spectrometer surrounds the calorimeter system, defining the overall dimensions of the ATLAS detector. It identifies muons and provides precise momentum measurements.

The air-core toroid system, with a long barrel and two end-cap magnets, generates strong bending power. Multiple-scattering effects are minimised, and the three layers of high precision tracking chambers achieve excellent muon momentum resolution.

A sophisticated trigger system provides real-time event reconstruction. It is able to reduce the proton-proton interaction rate of ~ 1 GHz, to a few hundred Hz for data recording. This requires an overall rejection factor of 5×10^6 against minimum bias processes, while maintaining maximum efficiency for the physics events of interest.

Detector Component	Required Resolution	η Coverage
Tracking	$\sigma_{p_T}/p_T = 0.05\%/p_T \oplus 1\%$	$ \eta < 2.5$
EM calorimetry	$\sigma_E/E = 10\%/\sqrt{E} \oplus 0.7\%$	$ \eta < 3.2$
Hadronic calorimetry (jets)	$\sigma_E/E = 50\%/\sqrt{E} \oplus 3\%$	$ \eta < 3.2$
Muon spectrometer	$\sigma_{p_T}/p_T = 10\%$ at $p_T = 1$ TeV	$ \eta < 2.7$

Table 2.1: General performance goals of the ATLAS detector. Units for E and p_T are in GeV.

2.2.1 Inner Detector

The closest-to-the-beam sub-detector of the ATLAS apparatus is the inner detector (ID) [51]. Combining information about transverse momentum, pseudorapidity, azimuthal angle and both transverse and longitudinal impact parameters, the ID identifies charged particles, reconstructs their trajectories and extrapolates secondary vertices.

It sustains the high track particle density emerging from the collision point: a flux of about 10^3 particles every 25 ns. Its high detector granularity provides high-precision measurements and offers high momentum and vertex resolution, using Pixel and silicon microstrip trackers in conjunction with the straw tubes. With a total length of 6.2 m and a diameter of 2.1 m, this detector is soaked in the 2 T magnetic field provided by the central solenoid. In the following more detailed descriptions are provided for the Pixel Detector, the SemiConductor Tracker, and the Transition Radiation Tracker.

Pixel Detector

The Pixel Detector [52, 53] constitutes the innermost component of the ID. It measures at least three space points, and thus it reconstructs tracks and vertices at each beam crossing independently from the outer detectors. It ensures high granularity in the area around the proton-proton collisions (i.e. with high density of charged tracks) and provides the impact parameter with high resolution.

It is composed of three concentric barrel layers and two end-caps of three disks each. The former have a mean radius of 5.05, 8.85 and 12.25 cm, while the latter extend from 8.88 cm to 14.96 cm. Its 80 million silicon sensors, of size $50 \times 400 \mu\text{m}^2$, cover an active area of $16.4 \times 60.8 \text{ mm}^2$ and contain 47232 pixels [54]. The pixel detector covers the pseudorapidity region $|\eta| < 2.5$. It reaches intrinsic accuracies of 10 μm in $R - \phi$ and 115 μm in z in the barrel; 10 μm in $R - \phi$ and 115 μm in R in the disks.

For 2015 operations, an additional layer – the Insertable B-Layer – has been installed [55]. It will be the closest to the beam detector.

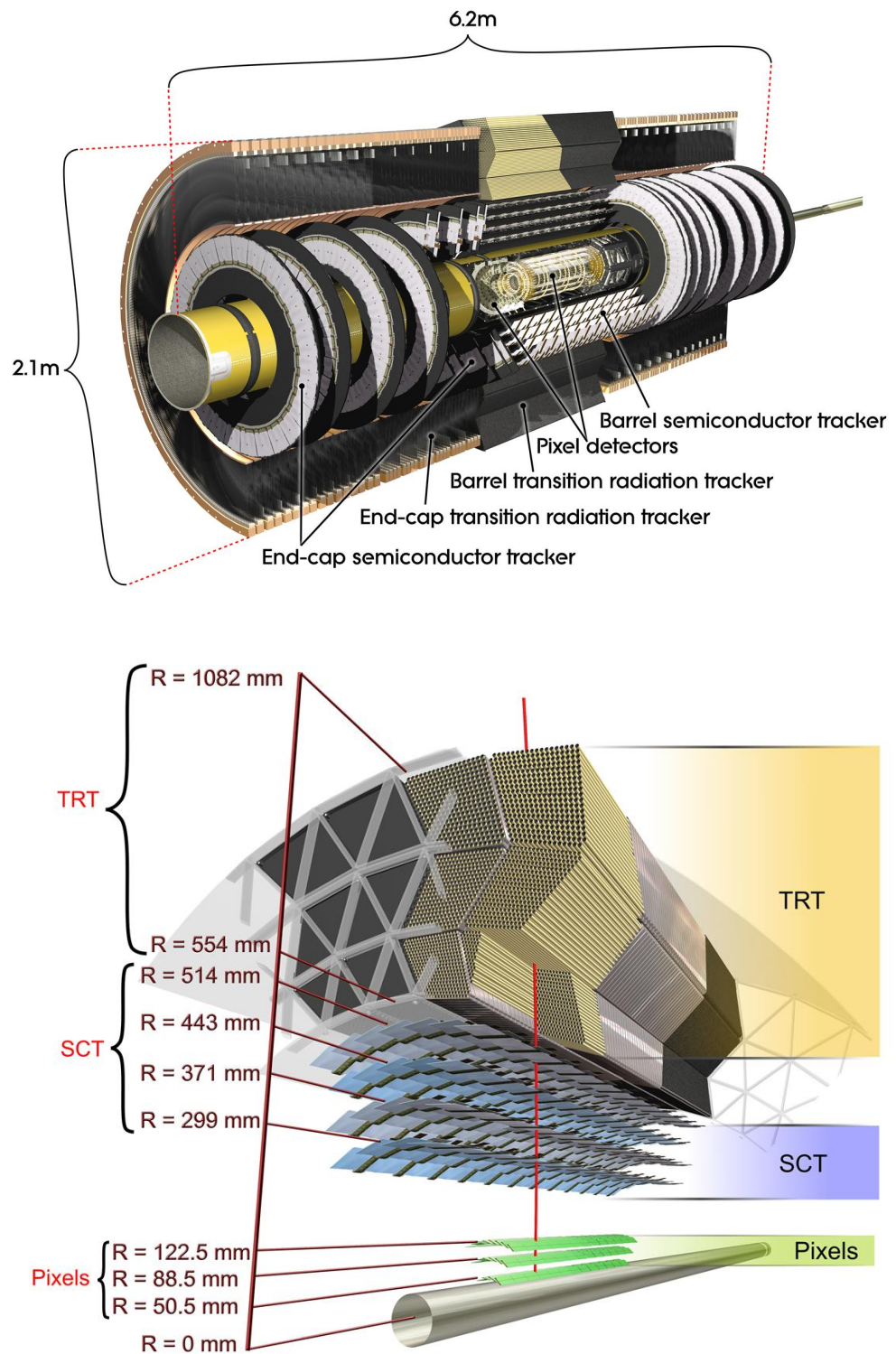


Figure 2.3: Overview of the ATLAS Inner Detector and a scheme of the barrel sector, being crossed by one high-energy particle, with labels and dimensions. Figure taken from <http://www.atlas.ch/photos/index.html>

	Radial extension [mm]	Length [mm]
Overall ID envelope	$0 < R < 1150$	$0 < z < 3512$
Beam-pipe	$29 < R < 36$	
Pixel Detector	$45.5 < R < 242$	$0 < z < 3092$
3 cylindrical layers	$50.5 < R < 122.5$	$0 < z < 400.5$
2 × 3 disks	$88.8 < R < 149.6$	$495 < z < 650$
SCT	$255 < R < 549$	$0 < z < 805$
Overall envelope (barrel)	$251 < R < 610$	$810 < z < 2797$
Overall envelope (end-cap)	$299 < R < 514$	$0 < z < 749$
4 cylindrical layers	$275 < R < 560$	$839 < z < 2735$
2 × 9 disks		
TRT	$554 < R < 1082$	$0 < z < 780$
Overall envelope (barrel)	$617 < R < 1106$	$8827 < z < 2744$
Overall envelope (end-cap)	$563 < R < 1066$	$0 < z < 712$
73 straw planes	$644 < R < 1004$	$848 < z < 2710$
2 × 9 disks		

Table 2.2: Main parameters of the ATLAS inner detector: the Overall ID envelope, the Pixel detector, the SCT and the TRT.

SemiConductor Tracker

The SemiConductor Tracker [56, 57] determines particle momentum, vertex position and impact parameter by providing four three-dimensional position measurements per track. It consists of four concentric barrels and two end-caps. They both use silicon micro-strips. In the former they are arranged in four nested cylindrical layers: one set of strips in each layer parallel to the beam direction and a relative angle of 40 mrad. It reaches an accuracies per module of $17 \mu m$ in $R - \phi$ and $580 \mu m$ in z . In the latter they are arranged in nine disks: a set of strips running radially and a set of stereo strips at an angle of 40 mrad. It reaches an accuracy of $17 \mu m$ in $R - \phi$ and $580 \mu m$ in R . Covering a surface of $63 m^2$, this detector consists of 4.1×10^3 modules [54].

Transition Radiation Tracker

The Transition Radiation Tracker [58] is both a straw drift-tube tracker and a transition radiation detector. Divided in two barrel sections and two end-caps, this gas detector consists of 3.0×10^5 proportional drift tubes – called straws – and 3.5×10^5 readout channels. Each tube has a radius of $2 mm$. In the barrel sections they are arranged parallel to the beam-line direction, $144 cm$ long, with their wires divided into two halves at $\eta = 0$. In two end-cap regions they are arranged radially to the beam-line direction, and $37 cm$ long.

The way it works is straitforward. Charged particles leave a trail of electron-ion pairs while traversing a straw. These drift towards the anode wire, gaining energy and creating further electron-ion pairs. Thus, an avalanche process that creates a cascade of electron-ion pairs begins. The drift time for each straw determines the distance of closest approach of each particle to the anode wire. The detector sensitivity to transition radiation enhances the electron identification capabilities. Charged particles produce radiation when crossing the interface between two media of different dielectric constants – ATLAS exploits polypropylene and the $Xe/CF_4/CO_2$ gas mixture. The TRT uses the radiation intensity – which is proportional to the particle’s relativistic γ factor – and thus discriminates between electrons, with a high γ factor, and hadrons, with a low γ value.

The TRT provides only $R - \phi$ information, with an intrinsic accuracy of $130 \mu m$ per straw. However, the combination of precision silicon-based trackers at small radii with the TRT gives very robust pattern recognition and high precision in both $R - \phi$ and z coordinates. The straw hits contribute to the momentum measurement: the large number of measurements – ~ 36 per crossing track –, and longer measured track length compensate the lower precision per point, compared to silicon detectors.

2.2.2 Calorimeter detector

The ATLAS calorimeter system [59] surrounds the ID. With a shape of a 13.3 m long cylinder and with a radius of 4.23 m, it covers a total range of $|\eta| < 4.9$. It has a total weight of about 4×10^3 tones.

It consists of an electromagnetic and an hadronic calorimeter, the former measures and identifies electrons and photons, the latter measures the energy of both charged and neutral hadrons. It provides: precise measurement of energy, position and shower shape for electrons, photons and jets; estimation of the missing transverse momentum and particle identification, separating electrons and photons from hadrons and jets and hadronic τ decays from background jets; and containment for electromagnetic and hadronic showers of particles up to the TeV scale.

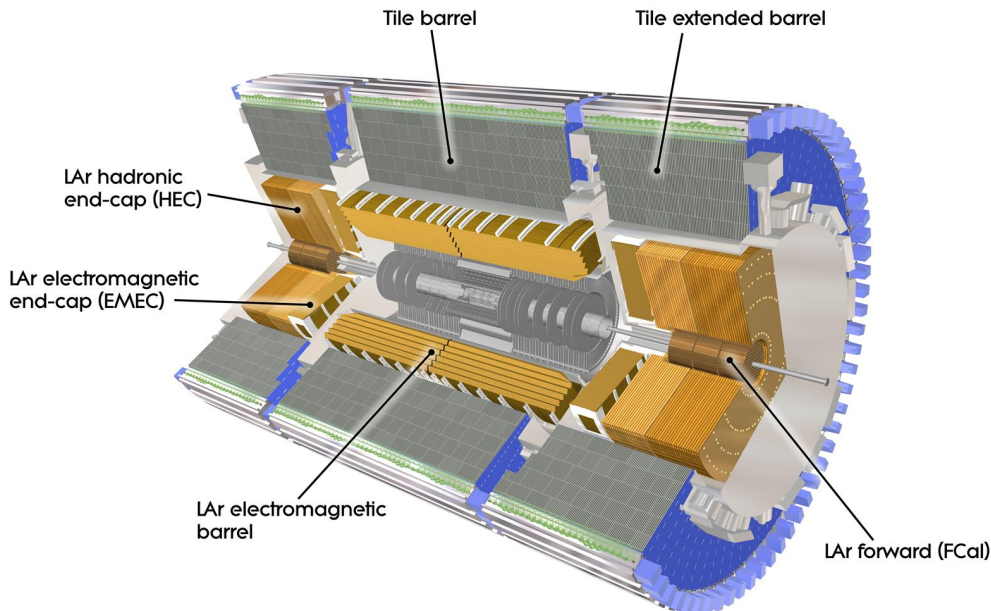


Figure 2.4: A computer generated image of the full ATLAS calorimeter. Figure taken from <http://www.atlas.ch/photos/index.html>

It uses layers of dense materials as absorbers, to cause an incoming particle to initiate a shower, interleaved with layers of active material, to detect particles created in the shower. The total signal in the active material results in the measurement of the incoming particle energy. The hadronic calorimeter needs a longer radial extension to provide the necessary containment to the showers. Placed around the EM, its total thickness is > 22 radiation lengths in the barrel and > 24 in the end-caps.

The electromagnetic calorimeter

The electromagnetic calorimeter is a lead–LAr detector: uses lead as absorber material, and liquid argon as sampling material – it has intrinsic

linearity, stability of response over time, and radiation-hardness. It possesses accordion-shaped Kapton electrodes and lead absorber plates over its full coverage. This geometry provides complete ϕ symmetry without azimuthal cracks.

It is divided into a barrel ($|\eta| < 1.475$) and two end-caps ($1.375 < |\eta| < 3.2$). The barrel calorimeter consists of two identical half-barrels, separated by a small gap of 6 mm at $z = 0$. In the region $|\eta| < 2.5$ the calorimeter is segmented in three sections in depth, suited for precision measurements of electrons and photons, also enhancing γ/π_0 and e/π separation and precision η -measurements. Each end-cap calorimeter is divided into two coaxial wheels: an outer wheel covering the region $1.375 < |\eta| < 2.5$, and an inner wheel covering the region $2.5 < |\eta| < 3.2$. This section is segmented in two sections in depth and has a coarser lateral granularity.

The hadronic calorimeter

The hadronic calorimeter surrounds the electromagnetic one. It measures the passage of charged particles from the induced fluorescence light. With its thickness of 11 interaction lengths at $\eta = 0$, it provides good containment for hadronic showers and reduces the number of punch-through hadrons to be smaller than the number of muons produced in the proton collisions. It possesses large η coverage and guarantees a good E_T -miss measurement.

The barrel hadronic calorimeter covers the range $|\eta| < 1.6$. It uses iron as absorber material and scintillating tiles as active material. These tiles are placed perpendicular to the colliding beams and are staggered in depth. The end-cap hadronic calorimeter, which receives an high radiation dose, uses liquid argon technology with copper as absorber material.

The forward calorimeter

The forward calorimeter uses liquid argon technology with copper and tungsten as absorber materials. It covers the region $3.2 < |\eta| < 4.9$, where radiation levels are high. The forward calorimeter is split longitudinally into an electromagnetic, and two hadronic compartments. Compared to the electromagnetic end-cap calorimeter, the forward calorimeter is placed 1.2 meter further away from the interaction point. This avoids neutrons from being backscattered into the inner detector volume.

2.2.3 Muon Spectrometer

The muon spectrometer [60] constitutes the outermost component of the ATLAS detector. It identifies muons and measures their deflections in the magnetic field, produced by the air-core toroid superconducting magnet system, and provides both high-resolution momentum measurements and stand-alone triggering capabilities.

The muon spectrometer covers the pseudorapidity region $|\eta| < 2.7$ for precision track measurements and $|\eta| < 2.4$ for triggering purposes. The

Table 2.3: Main parameters of the ATLAS calorimeter systems.

	Barrel	End-cap
EM calorimeter		
Number of layers and $ \eta $ coverage		
Presampler	$ \eta < 1.52$	$1.5 < \eta < 1.8$
Calorimeter	$ \eta < 1.35$	$1.375 < \eta < 1.5$
	$ \eta < 1.475$	$1.5 < \eta < 2.5$
		$2.5 < \eta < 3.2$
Granularity $\Delta\eta \times \Delta\phi$ versus $ \eta $		
Presampler	0.025×0.1	0.025×0.1
Calorimeter 1 st layer	$ \eta < 1.52$	$1.5 < \eta < 1.8$
	$ \eta < 1.40$	$1.375 < \eta < 1.425$
	$1.40 < \eta < 1.475$	$1.425 < \eta < 1.5$
		$1.5 < \eta < 1.8$
		$1.8 < \eta < 2.0$
		$2.0 < \eta < 2.4$
Calorimeter 2 nd layer	0.025×0.025	0.025×0.1
	$ \eta < 1.40$	$1.375 < \eta < 1.425$
	$1.40 < \eta < 1.475$	$1.425 < \eta < 2.5$
		$2.5 < \eta < 3.2$
Calorimeter 3 rd layer	0.050×0.025	0.050×0.025
Number of readout channels		
Presampler	7808	1536 (both sides)
Calorimeter	101760	62208 (both sides)

LAr hadronic end-cap	
$ \eta $ coverage	$1.5 < \eta < 3.2$
Number of layers	4
Granularity $\Delta\eta \times \Delta\phi$	1.5×0.1 $1.5 < \eta < 2.5$ $2.5 < \eta < 3.2$
Readout channels	5632 (both sides)
LAr forward calorimeter	
$ \eta $ coverage	$3.1 < \eta < 4.9$
Number of layers	4
Granularity $\Delta x \times \Delta y$ [cm]	FCall1: 3.0×2.6 $3.15 < \eta < 4.30$ FCall1: ~ 4 times finer $3.10 < \eta < 3.15$ FCall1: ~ 4 times finer $4.30 < \eta < 4.83$ FCall2: 3.3×4.2 $3.24 < \eta < 4.50$ FCall2: ~ 4 times finer $3.20 < \eta < 3.24$ FCall3: 5.4×4.7 $4.50 < \eta < 4.81$ FCall3: ~ 4 times finer $3.32 < \eta < 4.60$ FCall3: ~ 4 times finer $3.29 < \eta < 3.32$ FCall3: ~ 4 times finer $4.60 < \eta < 4.75$
Readout channels	3524 (both sides)
Scintillator tile calorimeter	
Barrel	
$ \eta $ coverage	$0.8 < \eta < 1.7$
Number of layers	3
Granularity $\Delta\eta \times \Delta\phi$	0.1×0.1
Last Layer	0.2×0.1
Readout channels	4092 (both sides)
Extended barrel	
$ \eta $ coverage	$ \eta < 1.0$
Number of layers	3
Granularity $\Delta\eta \times \Delta\phi$	0.1×0.1
Last Layer	0.1×0.1
Readout channels	5760

magnetic configuration provides a field orthogonal to the muon trajectories, and minimizes the degradation of resolution due to multiple scattering: we find a large barrel toroid, over the range $|\eta| < 1.4$; two smaller end-cap toroidal magnets, for $1.6 < |\eta| < 2.7$; and a combination of barrel and end-cap fields in the transition region.

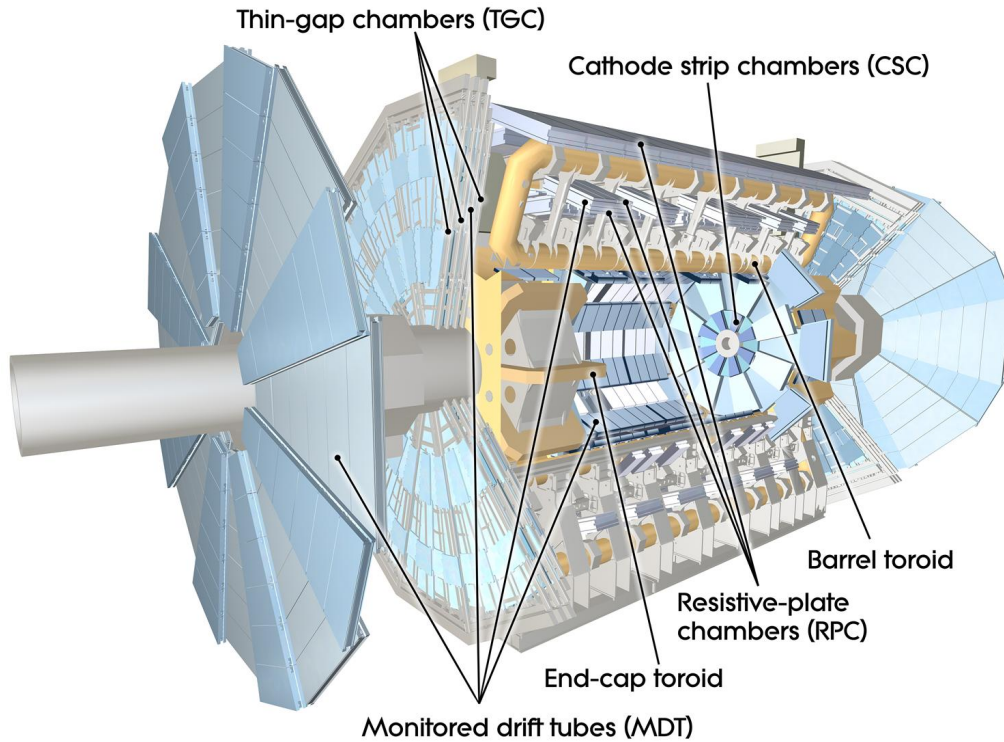


Figure 2.5: Overview of the ATLAS muon spectrometer components, labeled. Figure taken from <http://www.atlas.ch/photos/index.html>

The spectrometer employs four different chamber technologies: Monitored Drift Tubes (MDTs), Cathode Strip Chambers (CSCs), Resistive Plate Chambers (RPCs) and Thin Gap Chambers (TGCs). MDT chambers consist of aluminum tubes, with a 30 mm diameter, and a central wire. It provides precise muon tracking and momentum measurement in the region $|\eta| < 2.7$ ($|\eta| < 2.0$ in the innermost layer).

Its mechanism is plain. A muon crossing a tube produces ionization clusters in the gas, which drift into the wire. The high electric field around the wire multiplies them. Measuring the drift time of the first cluster that reaches the wire and passes over threshold allows to determine the distance between the muon and the wire. This results in a $\sim 80 \mu\text{m}$ resolution on the drift distance. CSC chambers are used in the innermost ring of the innermost end-cap layer ($2.0 < |\eta| < 2.7$) – their preference over the MDT is due to their finer granularity and faster operation. They consist in multi-wire proportional chambers with a spatial resolution of around $60 \mu\text{m}$. RPC chambers are used in the barrel ($|\eta| < 1.05$), while TGC chambers in the end-cap ($1.05 < |\eta| < 2.7$, 2.4 for triggering). They both produce a fast and less precise decision signal, useful in the trigger selection.

The muon spectrometer aims to provide: a stand-alone transverse momentum resolution of 2–3% over most of the kinematic range, except at very high momenta where it increases to about 10% at $p_T \sim 10$ TeV; and an invariant mass resolution for the decay of a heavy particle into two muons of approximately 2–4% for masses up to 1 TeV, increasing to 15% for a 5 TeV massive particle. Muon momenta measurements down to 4 GeV may be performed by the spectrometer alone. For enhancing the momentum resolution in the region below 100 GeV, tracks reconstructed in the muon spectrometer can be extrapolated back to the ID volume and matched with the ones reconstructed in the tracking detectors. In the region below 40 GeV, the ID measurements will dominate the momentum resolution, but measurements from the muon spectrometer are still required to identify the inner detector tracks as muons.

2.2.4 The trigger system

The ATLAS trigger system [49, 61, 62] selects interesting interactions and records them on permanent storage. The short bunch-crossing period of 25 ns, together with the need of high efficiency and selectivity, makes this task challenging: the trigger must be able to reduce the interaction rate of $\sim 10^9$ Hz down to O(100 Hz) for storage (from 3000 GB/s down to 300 MB/s). High precision, fast algorithms and robustness are the main features of the ATLAS trigger. It guarantees coverage of the full physics programme and gives an unbiased reduction of events without affecting physics results using complex signatures, p_T thresholds, tight selection criteria and precise matching between different detectors.

During 2012, a three level trigger system handled the events: the hardware-based Level-1 trigger (L1); and the software-based High Level Trigger (HLT), composed by the Level-2 trigger (L2) and the Event Filter (EF) – each level refines the decisions made at the previous level –, executed on two separate processing nodes. This configuration has changed: in 2015 L2 and EF are merged and processed on a single node.

L1 selects the regions of interest using reduced-granularity information from calorimeters and muon chambers, searching for high transverse-momentum muons, electrons/photons, hadrons and jets. Thus, L1 trigger identifies unambiguously the bunch-crossing of interest. Implemented as a system of purpose-built hardware processors, it handles a 75 kHz (upgradeable to 100 kHz) data flow and reaches its decision, handled by the Central Trigger Processor, within 2.5 μ s.

HLT uses Inner Detector information and the full granularity of both calorimeter and muon chamber data. L2 is the first trigger level in which track reconstruction is performed, using commercial processor farms; it reduces the event rate to 3.5 kHz, with an average event processing time of 40 ms. EF uses offline analysis procedures on fully-built events and performs track reconstruction using the clusters in the L1 Regions of Interest – but a “full-scan” mode, mainly used for B physics triggers, exists as well.

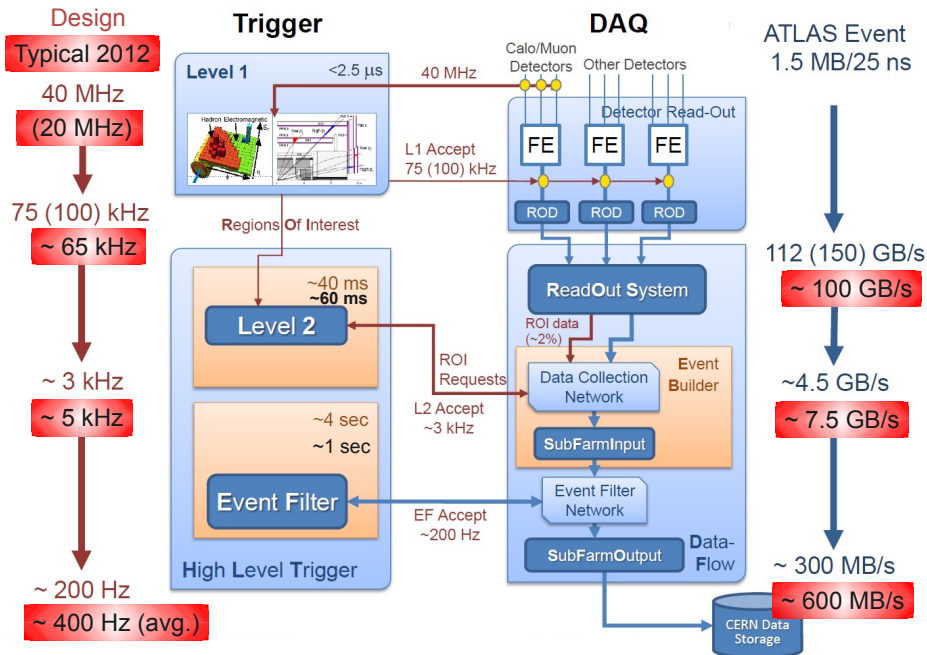


Figure 2.6: A schematic of the ATLAS trigger + DAQ infrastructure.

It brings the event rate to 200 Hz, with an average event processing time of 4 seconds. HLT tracking has different tunes of the pattern recognition specifically for each use, thus satisfying the clients' different requirements. It is essential for both trigger signatures and beam position determination.

The data acquisition system (DAQ) stores the data: it receives and buffers them from L1 readout electronics and, when requested, transmits RoI's information to the L2 trigger. It performs event-building for events fulfilling L2 selection criteria and moves the assembled events to the event filter, before moving them to permanent storage.

2.3 Software infrastructure

Computing is a major aspect of high energy physics. Every year LHC produces several petabytes of data: 15 PB in 2010; 23 PB in 2011; and 27 PB during 2012¹. This require a huge amount of storing power. This colossal volume constitutes a big processing challenge for the CERN Data Centre (DC), that processes it, stores it and sends it around the world for analysis. To manage this, in 2002 a new project started: the Worldwide LHC Computing Grid (WLCG) [63] – a distributed computing infrastructure arranged in tiers. The project is a global collaboration of more than 170 computing centres in 40 countries with the aim to provide global computing resources

¹More information can be found here: <http://www.isgtw.org/feature/large-hadron-colliders-worldwide-computer>

to store, distribute and analyse the LHC data.

This infrastructure manages the data from the four LHC experiments, exploiting a four-tiered structure:

- **Tier-0:** Based at CERN, it records the original raw data emerging from the acquisition systems. The Tier-0 performs the first-pass reconstruction of the events and stores a copy of these data. It also distributes a second copy of both the raw and the reconstructed data across the Tier-1 centres associated with the experiment.
- **Tier-1:** The Tier-1 centres have the responsibility for managing the permanent data storage – raw, simulated and processed data – and providing computational capacity for reprocessing and for analysis processes that require access to large amounts of data.
- **Tier-2:** The Tier-2 centres obtain data from Tier-1 centres, and send them back for permanent storage once they have processed them. They provide computational capacity and storage services for Monte Carlo event simulation and for end-user analysis.
- **Tier-3:** The Tier-3 is constituted by computing facilities in universities and laboratories that take part in the processing and analysis of LHC data. They are provided with access to the data and analysis facilities.

2.3.1 ATLAS software

Each experiment has its own software infrastructure. The ATLAS framework [64] is implemented in *Athena* – an enhanced version of the *Gaudi* architecture [65], developed for the LHCb collaboration. Nowadays, *Athena* is the sum of this kernel framework and ATLAS-specific enhancements. Written in Python language, *Athena* provides several tools, from job configuration, job tracing, performance monitoring, to data-processing history record, event and detector data management, random-number generation. The memory management allows to run a chain of algorithms in one job, or to split it into several jobs that read their input from disk.

Athena's main purposes are to generate simulated samples and to reconstruct both simulated and read events.

2.4 LHC operations

At 10:28 a.m. on 10 September 2008 [66] the LHC successfully completed its major test: for the first time a single proton beam circulated in the accelerator ring, in both the clockwise and the counter-clockwise direction. That was a historic event, a key moment in the High Energy Physics history.

But during these preliminary operations, a large helium leak occurred in sectors 3 and 4 of the LHC complex [67], and this incident postponed the first collision of more than one year. The failure was due to a faulty superconducting electrical connection between two magnets. This affected the magnets that underwent a transition from superconductive to resistive state. As a result, the liquid helium heated, the pressure raised till the point the release valves could not handle and a tonne of liquid helium leaked out into the ring. A total of 53 magnets were damaged in the incident. The repairing operations took place during the winter shutdown: the magnets were replaced; devices to detect similar resistances in advance were developed; and new helium release valves were installed.

LHC operations resumed in Autumn 2009. The first proton-proton collision – at 450 GeV energy per beam – was recorded on 23 November 2009 [68]. Operations lasted until December. In this period the LHC reached the highest-energy collision world record of 1.18 TeV.

The Chamonix workshop², which took place in January 2010, defined the future of the LHC operations. It was settled an initial data taking phase would have taken place. Thus, the accelerator ran at a center of mass energy of $\sqrt{S} = 7$ TeV during 2011, and $\sqrt{S} = 8$ TeV during 2012. The discovery made was a key-stone of the ATLAS searches programme: the Higgs Boson [1, 2]. Then, the accelerator complex would have been upgraded, reaching a center of mass energy of 13 TeV. The LHC will be operational in spring 2015, beginning the so-called Run-II. Collision data at higher energy will allow to measure precisely the Higgs boson properties and open a new window for physics beyond the Standard Model

²The workshop indico page can be found on <http://indico.cern.ch/event/67839/other-view?view=standard>

Events selection

This chapter describes what the raw data we analysed consist of, and what Monte Carlo simulations we performed to describe the studied reactions. Moreover, we will show the criteria used to select signal candidates from the Run-I data pull and the Multivariate Analysis techniques applied to optimize the background-signal separation.

The author was not involved in Monte Carlo simulations. However, these are an essential component of this study, as well as any High Energy Physics search. Thus we will summarize briefly the different programs we used.

The data screening optimization is a complex procedure: it begins with the trigger algorithms, that must correctly identify valid candidates amidst raw data; and ends by exploiting Multivariate tools on the shortlisted data, applying several cuts to a few discriminating variables. The former aspect lies outside this thesis work, but we will provide a rough description of the main concepts. We will focus on the multivariate analysis techniques, showing the discriminating variables we considered and the cuts we applied to them.

3.1 The data sample

CERN Run-I operations cover the 2009-2012 data-taking period, but only the 2011-2012 years prove useful for this search due to the high center of mass energy. However, this analysis uses only the full 2012 data-set, which consist of $\sim 20 \text{ fb}^{-1}$ of LHC proton-proton data at $\sqrt{s} = 8 \text{ TeV}$ – instead of the $\sim 5 \text{ fb}^{-1}$ at $\sqrt{s} = 7 \text{ TeV}$ of 2011. Figure 3.1 shows the total integrated luminosity during this two year-long period.

The data sample receives contributions from different sources. These reactions present in their final state four jets: two originating from the light valence quarks of the colliding protons – labelled as VBF jets –, which lie in the forward and backward regions of the detector; and two stemming from the bottom quarks – labelled as b -jets –, which lie in the central region. The contributions are both non-resonant and resonant processes. The former contain the QCD production of multijets. The latter include:

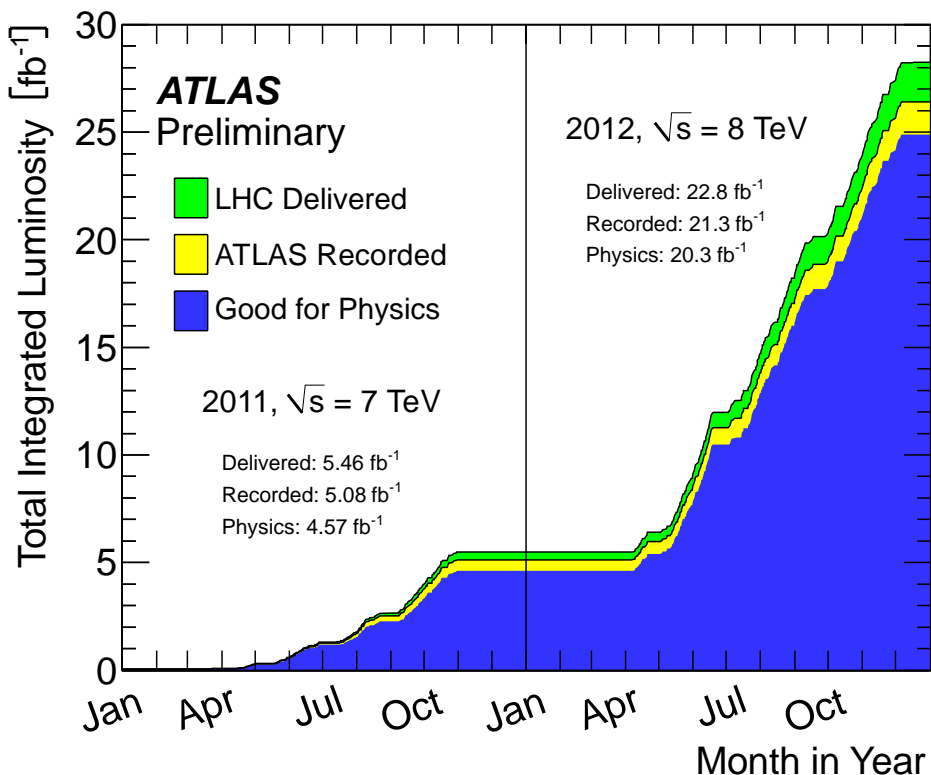


Figure 3.1: The ATLAS luminosity in the 2011-2012 data taking period. In green, yellow and blue we have the delivered, recorded by the ATLAS detector, and useful luminosity. In 2011 it reached ~ 5 fb⁻¹, in 2012 ~ 20 fb⁻¹. Image taken from [69].

$H \rightarrow b\bar{b}$ decay, produced via Vector Boson Fusion or gluon Fusion; $Z \rightarrow b\bar{b}$ decay, produced in association with jets through different processes; other concurrent reactions such as $t\bar{t}$, single top, $W + jets$ processes. In this search the Higgs Boson production via VBF process and its decay to a $b\bar{b}$ quark pair represents the signal. The other reactions constitute the background.

The process $qq \rightarrow qqH \rightarrow qq b\bar{b}$ peaks at $m_{b\bar{b}} \approx 125$ GeV [7]. Similar reactions lie nearby: the gluon Fusion-produced Higgs boson and the VBF-produced Z^0 boson – peaking at $m_{b\bar{b}} \approx 125$ GeV and at $m_{b\bar{b}} \approx 91$ GeV respectively. These three contributions cannot be fully isolated. Figure 3.2 show the resonant processes that constitute the data pull.

3.2 MC Samples

The QCD background components are multiple: the limited statistics of the available multijets simulated samples make it impossible to determine these contributions with MC simulations. Thus, the analysis is data-driven. However, by means of simulation-dedicated programs, we generated Monte Carlo samples of a few resonant processes: the Higgs and the Z^0 bosons.

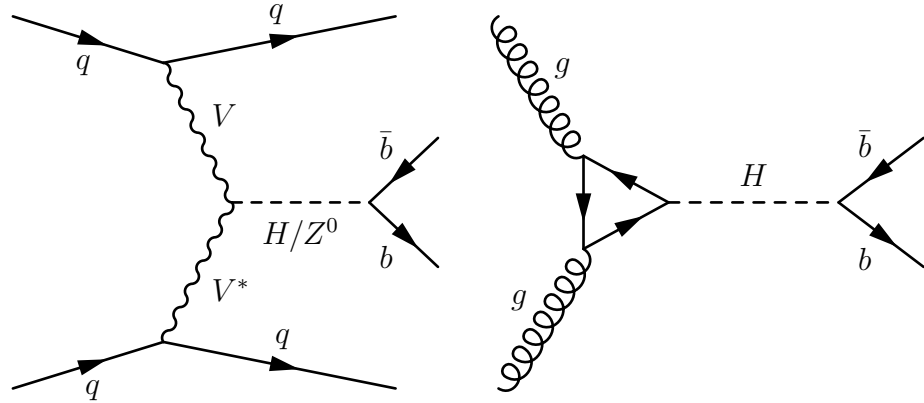


Figure 3.2: Feynman diagrams of the resonant processes involved: the production of an Higgs or Z^0 boson via Vector Boson Fusion; and the production of an Higgs boson via gluon-gluon Fusion. The final states have two b -jets, resulting from the decay of the bosons.

We combined different components of several MC simulation tools, so that we can obtain the most accurate theoretical predictions for these reactions: *Powheg* [70, 71] and *Pythia8* [72] to simulate the particles, their momentum four-vectors as produced in collision, and the hadronization process; *MadGraph* [73], to reproduce the decay of the resonances into a $b\bar{b}$ pair; *Geant4* [74] to simulate the particle interaction with the ATLAS detector.

3.2.1 Higgs boson

We generated MC samples for both the VBF and ggF Higgs events, using the total cross-sections and the decay branching ratios supplied by the theory [8, 9]. We exploited several programs. We modelled the samples using Pythia 8, interfaced with the CT10 [75] parton distribution functions, with the AU2 UE tune [76, 77] for the parton shower, hadronization and multiple parton interactions. Geant4 produced a limited statistic MC sample of the full ATLAS detector simulation. The program was corrected for all known detector effects, geometry and material composition. Atfast-II [78] produced the high statistics samples, once we checked it didn't produce any bias with respect to the fully simulated samples. This program uses detailed parameterization of shower shapes of single particles instead of the full simulation of the calorimeter. Table 3.1 lists the samples we used.

3.2.2 Z^0 boson

The MC for the VBF-generated Z^0 boson is produced using the cross-section reported on reference [79]. This simulation uses: *Pythia8* for the event generation, interfaced with CT10 parton distribution functions and AU2 UE tune; and *Madgraph* for the $Z^0 \rightarrow b\bar{b}$ decay, since the latter takes into account EM corrections for $Z \rightarrow b\bar{b}g$ with a hard gluon. This simulation is not yet available. For this thesis work, we are using the VBF-produced

DSID	Name Tag	Size
169723	PowhegPythia8_AU2CT10_VBFH125_bb e1788_a188_a224_r4348_p1328	1.5M
169723	PowhegPythia8_AU2CT10_VBFH125_bb e1788_s1581_s1586_r4349_p1328	100k
181707	PowhegPythia8_AU2CT10_ggH125NWA_bb_EF4jets e2512_a220_a205_r4540_p1328	500k
181395	PowhegPythia8_AU2CT10_ggH125NWA_Inclusive e2091_a188_a224_r4348	100k
181395	PowhegPythia8_AU2CT10_ggH125NWA_Inclusive e2091_s1581_s1586_r4349_r4348	100k

Table 3.1: *The Monte Carlo samples used, with their simulation and reconstruction tags, and their sizes. They simulated both the Vector Boson Fusion- and the gluon-gluon Fusion-produced Higgs boson and the decay to a bottom quarks pair.*

Higgs boson sample to deduce the Z^0 template: we shift the Higgs mass shape using a scale factor, given by the ratio between the boson masses, while leaving the BDT shape unchanged. If we indicate with m_{Z^0} and m_H the SM masses used in the MC sample generation, the Z^0 $m_{b\bar{b}}$ spectrum is given by:

$$M_{Z^0_{reco}} = M_{H_{reco}} \frac{m_{Z^0}}{m_H} \quad (3.1)$$

This choice relies on the fact that energy and momentum uncertainties are essentially relative errors, and on the assumption the BDT spectra of the processes are similar, being both reactions produced via VBF. The Z^0 MC sample will test the validity of this approach.

3.3 Preselection

The dataset must satisfy several requirements: good beam conditions, good detector performance and data quality requirements. We retain events with exactly four jets and with more than three tracks associated to the primary vertex. Removed those affected by LAr noise burst and data corruption, we sorted the four jets according to their pseudorapidity values: the two less central are identified as the “VBF”-jets; the two more central are b -tagged and required to be within the tracker acceptance – i.e. in the region $|\eta| < 2.5$. Table 3.2 shows the precise cutflow applied.

Jets were reconstructed using the anti- k_T jet algorithm [80] with a reconstruction parameter $R = 0.4$. Those originating from b -quarks were identified and btagged exploiting the MV170 algorithm (see table B.1).

Data			
Cut	N_{bkg}	Cut efficiency	Total efficiency
trigger and at least 4 jets	93258450	–	–
good runs list	87489198	93.81 %	93.81 %
$n_{tracks}^{PV} > 3$	87473561	99.98 %	93.80 %
LAr noise removal	87278533	99.78 %	93.59 %
trigger	35573927	40.76 %	38.15 %
4 jets with $p_T > 50$ GeV	8874186	24.95 %	9.52 %
online RoIs b -jets matching	2111639	23.80 %	2.26 %
centrality of b -jets	2082668	98.63 %	2.23 %
offline b -tagging b -jets	1057860	50.78 %	1.13 %
$p_T^{b\bar{b}} > 100$ GeV	654941	62.91 %	0.70 %

VBF-Higgs			
Cut	N_{bkg}	Cut efficiency	Total efficiency
generated	18211	–	–
$n_{tracks}^{PV} > 3$	18206	99.97 %	99.97 %
LAr noise removal	18206	100.00 %	99.97 %
trigger	996	5.48 %	5.47 %
4 jets with $p_T > 50$ GeV	382	38.41 %	2.10 %
truth-matching	331	86.50 %	1.82 %
η -sorting	258	77.95 %	1.42 %
online RoIs b -jets matching	230	89.22 %	1.26 %
centrality of b -jets	229	99.57 %	1.26 %
offline b -tagging b -jets	196	85.59 %	1.08 %
$p_T^{b\bar{b}} > 100$ GeV	147	75.35 %	0.81 %

ggF-Higgs			
Cut	N_{bkg}	Cut efficiency	Total efficiency
generated	41321	–	–
$n_{tracks}^{PV} > 3$	41315	99.98 %	99.98 %
LAr noise removal	41315	100.00 %	99.98 %
trigger	1504	3.64 %	3.64 %
4 jets with $p_T > 50$ GeV	526	34.97 %	1.27 %
online RoIs b -jets matching	150	28.63 %	0.36 %
centrality of b -jets	150	99.78 %	0.36 %
offline b -tagging b -jets	126	83.89 %	0.31 %
$p_T^{b\bar{b}} > 100$ GeV	95	75.69 %	0.23 %

Table 3.2: Summary of the cut-flows that both data and MC samples got past. The signal yields are normalized to those expected on the full used luminosity, according to the values of cross-section and \mathcal{BR} given by the theory.

3.3.1 Trigger

Events are selected by using b -jets triggers. The p_T thresholds of these triggers are 15 GeV at the L1 trigger and 35 GeV at the EF stage, according to the data-taking period. During the full 2012 year we used 2 b -jets triggers and, for part of the data-taking period ($\sim 20\%$), also some VBF-dedicated triggers – exploiting the reaction topology, they require the presence of one b -jet and one or two forward jets. Table 3.3 summarizes the different p_T thresholds of these triggers.

Year	Period	2 b -jets
2012	A-L	EF_2b35_loose_4j35_a4tchad

Year	Period	b -jets + VBF
2012	H2-L	EF_b35_medium_j35_a4tchad_vbf_3L1J15_FJ15
2012	H2-L	EF_b35_medium_j35_a4tchad_vbf_2L1FJ15

Table 3.3: The triggers used in this analysis for the 2012 data taking periods. The ATLAS trigger naming conventions – referring to the forthcoming Run-II triggers – can be found on <https://twiki.cern.ch/twiki/bin/view/Atlas/TriggerNamingRun2>. The main concept remain unchanged even for Run-I triggers.

We used these two uncorrelated sets of triggers. They have reasonable acceptance on the signal samples and their complementary use ensures a substantial signal acceptance gain.

3.3.2 p_T^{jets} threshold

We performed the secondary vertex reconstruction requiring all the four jets to possess a transverse momentum $p_T > 50$ GeV and pseudorapidity $|\eta| < 4.5$. The transverse momentum energy choice is dictated by the ATLAS trigger efficiency. This is defined as the probability that one event in the data sample satisfies the trigger requirements, as a function of an observable; the efficiency increases the higher the p_T of the four jets. With this selection criterion the working point lies in the trigger efficiency plateau zone, thus the trigger turn-on systematic contribution becomes minimal.

3.3.3 $p_T^{b\bar{b}}$ threshold

The shortlisted data distribution in the $m_{b\bar{b}}$ spectrum shows a “double structure” (the magenta template in figure 3.3), mostly caused by QCD events with back-to-back pairs. Its removal is mandatory for a correct performance of the analysis: this data behaviour makes it impossible to perform an unbiased assessment of both the Z^0 and the Higgs signal. This particular shape of the $m_{b\bar{b}}$ data distribution proves detrimental for the analysis.

In order to cure this behaviour, we imposed a cut on $p_T^{b\bar{b}}$, i.e. the transfer momentum of the b -jet pair – we required $p_T^{b\bar{b}} > 100$ GeV. This choice of a cut allows us to resolve the Z^0 contribution – it lies in a smooth region – and describe the background shape with a low-degree polynomial. While leaving the $m_{b\bar{b}}$ Higgs distribution unchanged. We lose a bit in signal statistics though: the cut efficiency is $\sim 75\%$. Moreover, the unresolved jets contribution to the signal is negligible even without a cut on $\Delta R_{b\bar{b}} \equiv \sqrt{\Delta\eta^2 + \Delta\phi^2}$, i.e. the angular separation between two resolved b -jets. The b -jets in the signal sample are always separated by a $\Delta R_{b\bar{b}}$ distance greater than 0.5. Figure 3.3 compares the data distribution after and before we applied this cut, and shows how it improves the data shape.

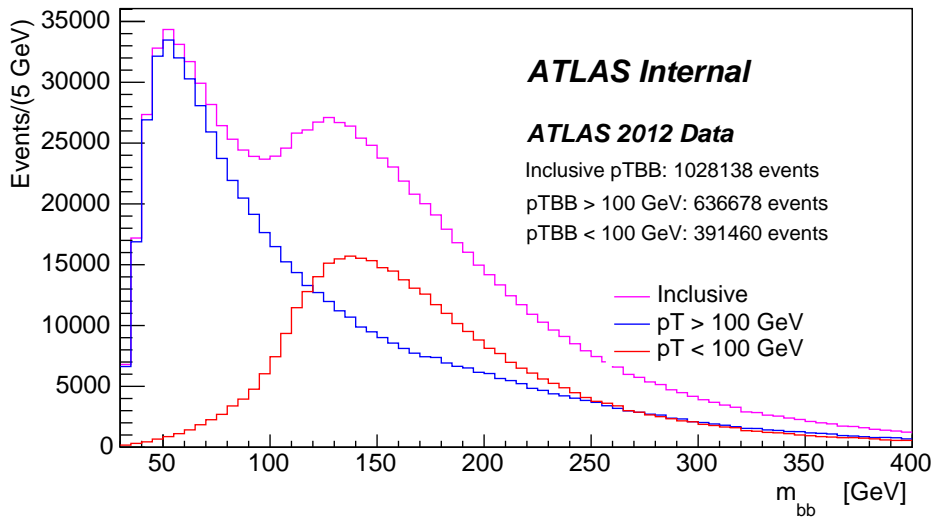


Figure 3.3: The $p_T^{b\bar{b}}$ cut removes the $m_{b\bar{b}}$ “double structure” of the data. In magenta the $m_{b\bar{b}}$ spectrum before this restraint, in red the data excluded, and in blue the retained events.

3.4 Multivariate analysis

The preselection phase provided a first data screening, but too big the background primacy – if compared with signal events – required a more accurate selection. Multivariate Data Analysis (MVA) techniques can achieve a better background-signal separation.

Providing a signal and a bkg-only samples and combining the individual discriminating power of a few selected variables, we can create a single multivariate classifier on which we can apply cuts: different cuts provide particular signal efficiency/background rejection configurations. For both the Multivariate training and testing phase we used: an Higgs Monte Carlo sample as signal; and the data in the side-bands – defined as the regions $70 < m_{b\bar{b}} < 90$ GeV and $150 < m_{b\bar{b}} < 190$ GeV – as background-only sample. On these we applied the selection criteria. The analysis strategy relies on a

background-plus-signal fit of the $m_{b\bar{b}}$ spectrum; thus we took into account, as input variables, only those with a minimal correlation with $m_{b\bar{b}}$:

- m_{JJ} : the invariant mass of the VBF-jet pair.
- $\Delta\eta_{JJ}$: the pseudorapidity separation between the two VBF-jets.
- η_J^* : the pseudorapidity separation between the VBF-jet pair and the Higgs candidate ($\eta_J^* = \frac{1}{2}(\eta_{J_1} + \eta_{J_2}) - \frac{1}{2}(\eta_{b_1} + \eta_{b_2})$)
- H_T : the scalar sum of the transverse momenta of additional jets (with $p_T > 20$ GeV, calibrated, passing the LAr removal and the electron overlap removal as the four main jets in the event) in the central region of the detector, i.e. $|\eta| < 2.5$.
- $\cos\theta$: the cosine of the polar angle of the vector $\vec{p}_{J_1} \times \vec{p}_{J_2}$ in the Higgs boson rest frame.
- $\cos\alpha$: the cosine of the polar angle of the vector $\vec{p}_{J_1} + \vec{p}_{J_2}$ in the Higgs boson rest frame.
- $\max(|\eta_J|)$: The maximum pseudorapidity value of one of the light jets.
- The calorimeter widths of the jets originated by the light quarks.

The last variables aim to separate jets issued from quark hadronization from those produced from gluon hadronization. They constitute the quark/gluon tagger.

We optimized the Multivariate Analysis in order to maximize the VBF significance. We tested several MVA tools, implemented in the ROOT-integrated [83] TMVA package (*Toolkit for Multivariate and Data Analysis*) [84]: Boosted Decision Tree; Neural Networks; likelihoodPCA; and H-matrix discriminant – the best method being the one with the most discriminating ROC curve (figure 3.5), i.e. the Boosted Decision Tree (BDT).

Figure 3.4 shows the signal and the background distributions of the input variables used. Table 3.4 illustrates the discriminant power of these variables: being sorted according to their ranking, the higher a variable is, the more discriminant power it has. The most discriminant variables result to be those constituting the quark/gluon tagger.

3.5 Significance

This data selection reaches the greatest separation between signal and background and maximizes both the signal-to-noise ratio and the Higgs significance. The latter, calculated in the region $100 < m_{b\bar{b}} < 140$ GeV, is defined as the ratio $S/\sqrt{S+B}$, where we labelled with S and B the number of signal and background events. The multivariate selection itself raised the VBF significance from 0.36 to 0.63. Figure 3.6 shows the significance value, for different BDT output cuts.

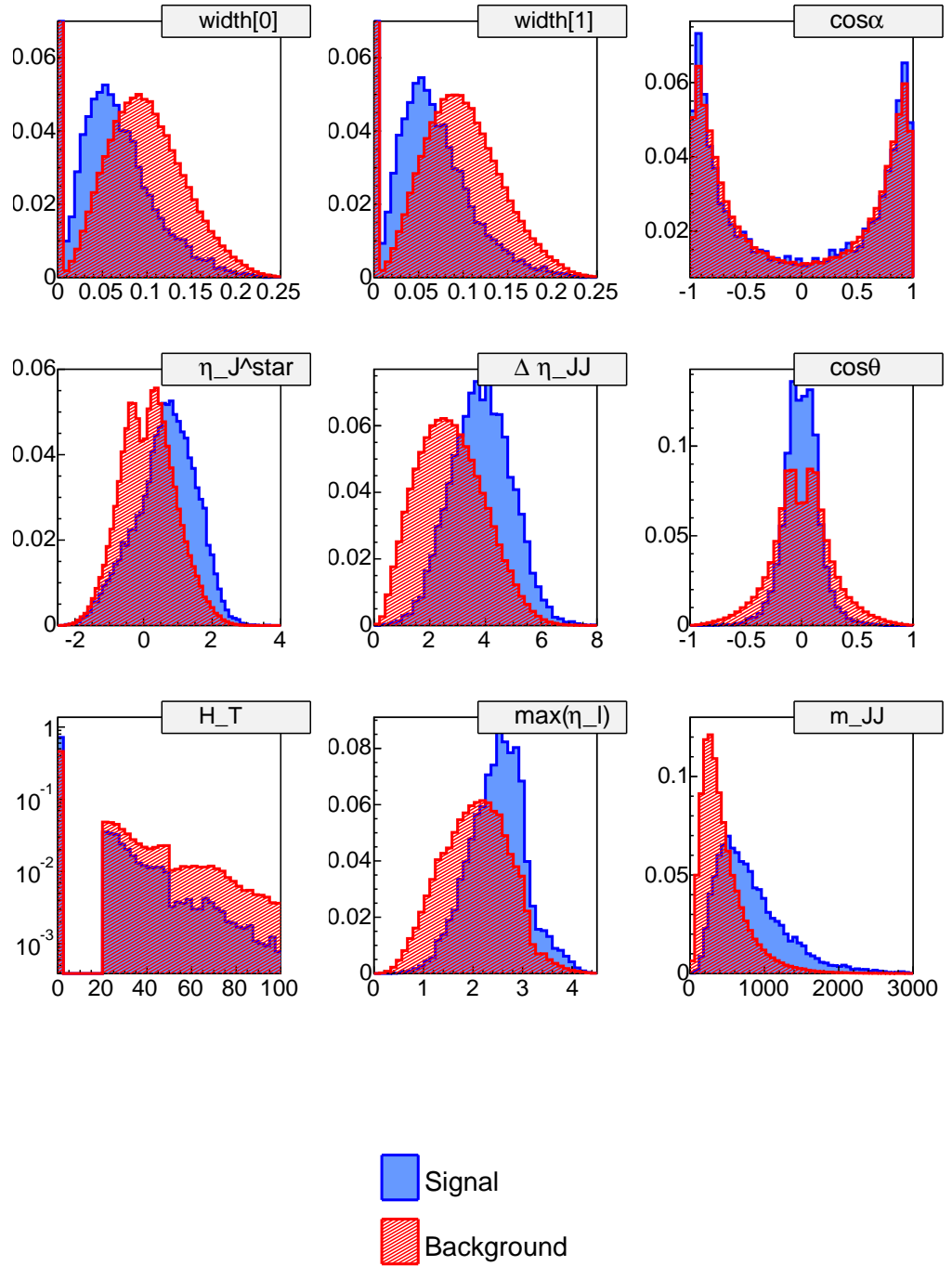


Figure 3.4: The input distributions used in the BDT training and testing phase. The BDT output variable will be the discriminating variable that will separate the background from the signal sample.

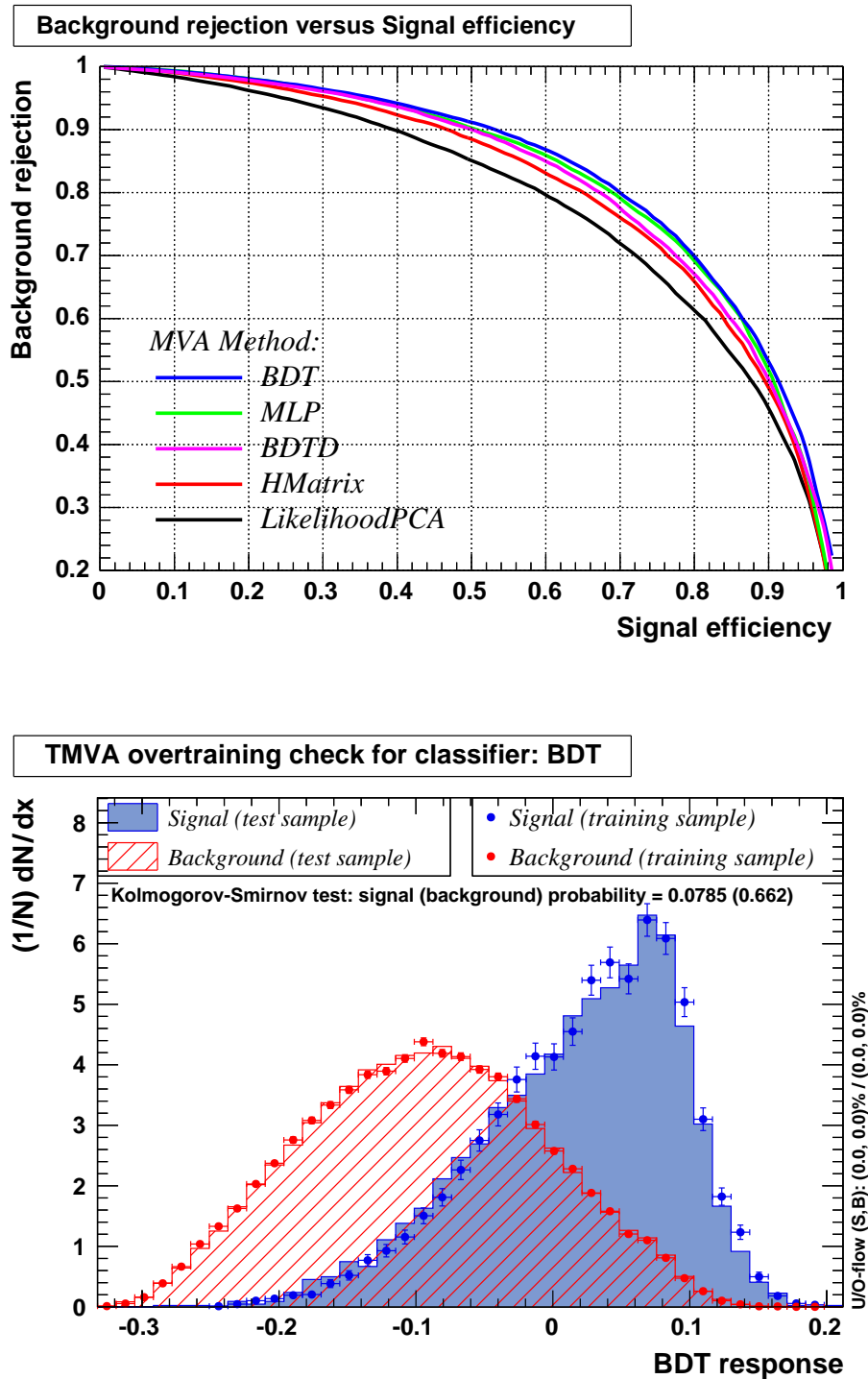


Figure 3.5: The results of the MVA analysis: the ROC curves of the Multivariate Analysis technique we tested; and the BDT output, with training and testing sample superimposed. The overtraining check for the classifiers is performed with the Kolmogorov-Smirnov test [81, 82].

Rank	Variable	Importance
1	width[J_1]	0.132
2	width[J_2]	0.132
3	$\cos \alpha$	0.128
4	η_j^*	0.112
5	$\Delta\eta_{JJ}$	0.109
6	$\cos \theta$	0.099
7	H_T	0.097
8	$\max(\eta_J)$	0.096
9	m_{JJ}	0.094

Table 3.4: The input variable ranking. The top ranked is the most discriminating. We labelled with J_1 and J_2 the VBF-jets, sorted in η .

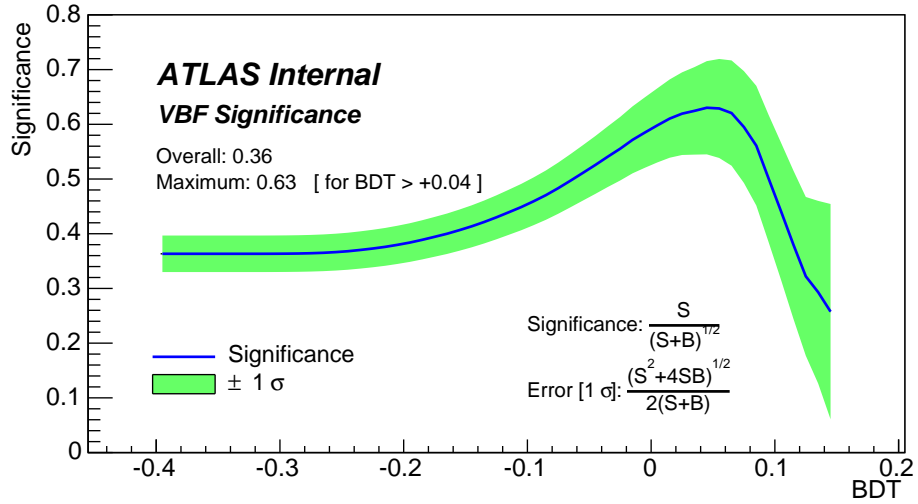


Figure 3.6: Values of the VBF significance for different BDT cuts. We reported both the $S/\sqrt{S+B}$ value and its error. The the maximum signal significance is 0.63, obtained imposing the cut $BDT > +0.04$.

Fit to the $b\bar{b}$ pair invariant mass

This chapter illustrates the procedures we exploited to manage the data pull and assess the systematic contributions, the fit strategies we adopted, and the results we obtained.

At first, we will summarize the preliminary operations: how we divided the shortlisted data into independent BDT regions; how we tuned their choice to minimize the signal statistical uncertainty; and what the optimal interpolation range consists in. Then, we will present the background models which best describe the data pull and the results obtained from the fit. We will also explain which sources contribute to the systematic error and how we evaluate their magnitude. Eventually, we will compare our results with those the CMS collaboration obtained in a similar study.

4.1 Fit strategy

The strategy followed is similar to the one the CMS collaboration adopted [10]: use Multivariate Analysis techniques to create a discriminant variable; defined four MVA output regions – each statistically independent from one another –, fit them simultaneously and extract the signal. The fit is performed with a suitable background function and the physical components, i.e. the Higgs and the Z^0 bosons.

We developed a quark/gluon tagger with the aim to separate the signal from the gluon fusion-produced Higgs boson. This tagger cannot separate the VBF from ggF contribution. Thus the ggF component will be accounted as signal as well. Moreover, the contribution of the final state $Z + jet$ with Z^0 decaying to $b\bar{b}$ has been determined using real data, leaving the corresponding component floating in the fit.

4.1.1 BDT Regions

Figure 4.1 shows the BDT output. We tuned the choice of the BDT slices configuration in order to optimize the VBF signal significance:

- We defined four floating cuts A, B, C and D so that they always satisfy the condition $A < B < C < D$. Thus:
 - **Region 0** covers the range $-1.00 < \text{BDT} < A$
 - **Region I** covers the range $A < \text{BDT} < B$
 - **Region II** covers the range $B < \text{BDT} < C$
 - **Region III** covers the range $C < \text{BDT} < D$
 - **Region IV** covers the range $D < \text{BDT} < 1.00$

Region 0 possesses the lowest VBF significance. As a consequence, the data it contains will not be used in the signal search.

- We analyzed every cut combination and estimated the statistical errors, combining the VBF significances in each of the retained regions. We defined the quantity

$$\Sigma_{stat}(\mu) \equiv \left[\sum_{i=1}^4 \left(\frac{S_i}{\sqrt{S_i + B_i}} \right)^2 \right]^{-\frac{1}{2}} \quad (4.1)$$

where i labels the BDT region, S and B represent the VBF signal and background events in the range $100 < m_{b\bar{b}} < 140$ GeV. Amidst all the possible configurations, the chosen cut values are those that minimize $\Sigma_{stat}(\mu)$.

	BDT Range	$S/\sqrt{S+B}$	$\sqrt{S+B}/S$
Region 0	$-1.00 < \text{BDT} < -0.07$	0.056 ± 0.015	–
Region I	$-0.07 < \text{BDT} < +0.01$	0.18 ± 0.03	5.43 ± 0.96
Region II	$+0.01 < \text{BDT} < +0.06$	0.32 ± 0.06	3.15 ± 0.56
Region III	$+0.06 < \text{BDT} < +0.09$	0.41 ± 0.09	2.42 ± 0.50
Region IV	$+0.09 < \text{BDT} < +1.00$	0.500 ± 0.116	2.00 ± 0.46
		$\Sigma_{stat}(\mu) = 1.34 \pm 0.08$	

Table 4.1: The BDT output cuts that define the four analysis regions and the significances. The assessment of the statistical error $\Sigma_{stat}(\mu)$ is an underestimation of the real value.

We estimated the number of signal events the SM predicts for this search and for these preselection criteria by means of the MC samples. With the achieved BDT cuts configuration we obtained a minimum value of $\Sigma_{stat}(\mu) = 1.34 \pm 0.08$. The overall VBF significance, i.e. in the BDT range covered from the retained regions, is 0.50 ± 0.05 . Table 4.1 summarizes the final region definition, reporting for each of them the significance. Table 4.2 summarizes the expected number of events in the $100 < m_{b\bar{b}} < 140$ GeV range, organized according to the BDT regions.

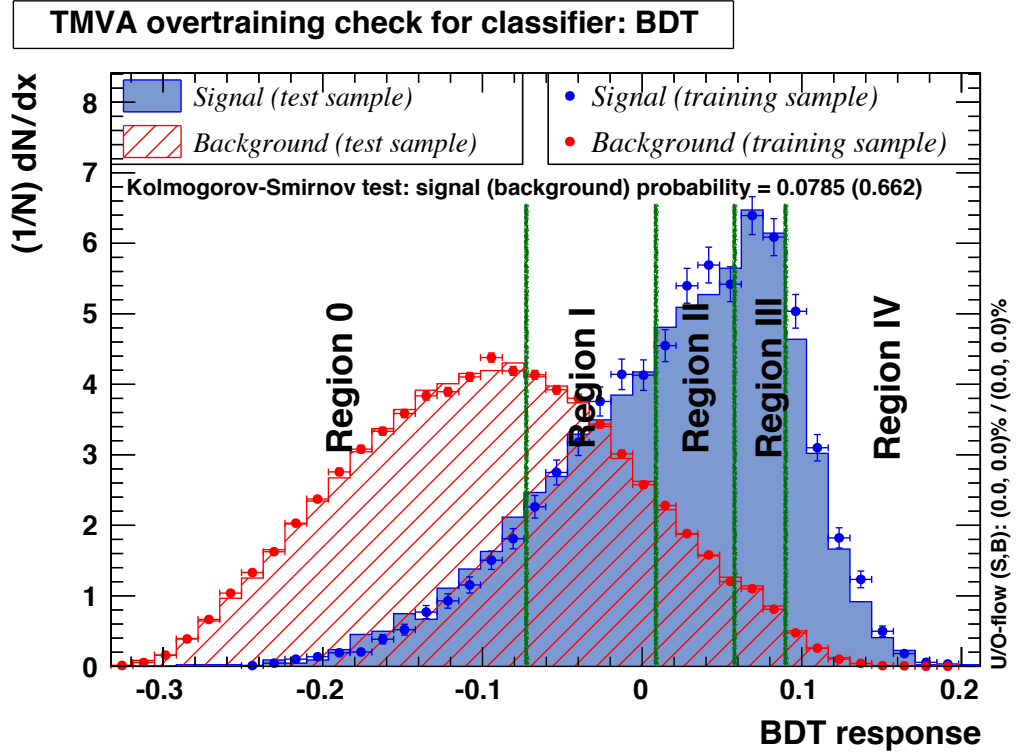


Figure 4.1: The BDT output, i.e. our discriminating variable. We defined four independent regions, but only four of them were retained, covering a total BDT range of $-0.07 < VFB < 1.00$.

$100 < m_{b\bar{b}} < 140 \text{ GeV}$				
ATLAS	Bkg	VBF H	ggF H	ggF H/VBF H
Region 0	6.2e+4	14	38	271.6 [%]
Region I	3.0e+4	32	19	59.7 [%]
Region II	9.6e+3	31	7	23.6 [%]
Region III	4.2e+3	23	2	9.0 [%]
Region IV	3.1e+3	18	1	7.7 [%]
Expected signal in the overall BDT region				
	1.1e+5	118	67	57.3 [%]
Expected signal in the $-0.07 < BDT < 1.00$ region				
	4.4e+4	104	29	28.6 [%]

Table 4.2: Table showing the number of signal – both ggF- and VBF-produced – and the number of background events, according to the BDT regions. The ratios ggF/VBF are reported.

4.1.2 Fit Range

We performed a blind analysis. This requires to define two regions in the $m_{b\bar{b}}$ spectrum: a first one containing the signal sample; and another one completely signal-free. We defined the blind region as the $100 < m_{b\bar{b}} < 140$ GeV range, the remaining $m_{b\bar{b}}$ spectrum as side-bands. However, the Higgs signal is too spread in the $m_{b\bar{b}}$ spectrum. Figure 4.2 shows the VBF-generated Higgs MC sample; it proves the blind region is not wide enough to comprise all the signal, so the side-bands contain some events ($\sim 20\%$ of the total Higgs yield).

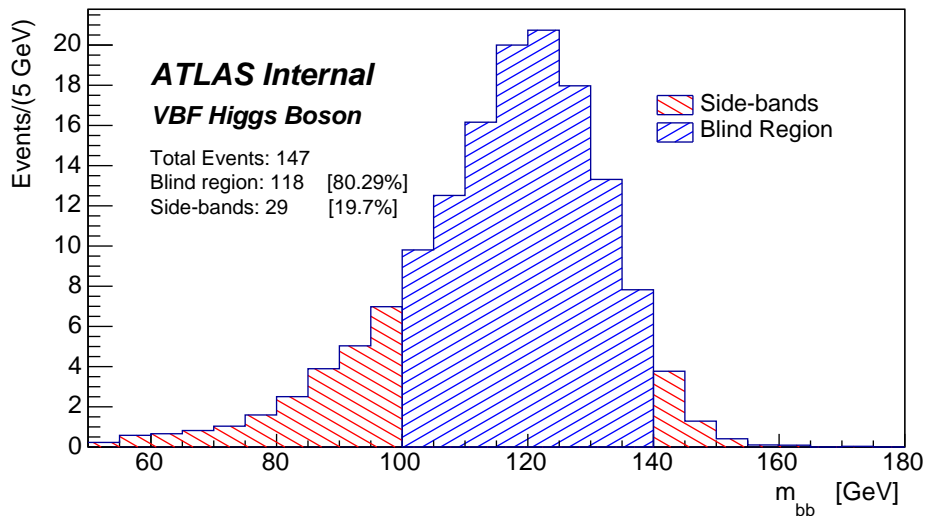


Figure 4.2: The VBF-produced Higgs Boson template. The events in the side-bands ($\sim 20\%$ of the total Higgs events) explain the bias obtained with the side-bands fit procedure.

This represents a problem: we need to verify that the fit produces unbiased results. We considered two different approaches to fit the data. One consists in performing the fit in all the $m_{b\bar{b}}$ spectrum leaving all the parameters floating (the “full-range procedure”). The other consists in determining first both the background shape and the Z^0 contribution with a fit only in the side-bands, fixing them and performing a fit only in the blind region to extrapolate the Higgs contribution (the “side-bands procedure”). To evaluate which one of these strategies provides unbiased results, we developed a procedure summarizable in a few steps:

- Produce several MC samples of both the background and the signals. Fit the pseudo-data with a determined background model using both the approaches.
- Extrapolate from the fit the μ_{meas} value for the Higgs Boson and compare this with the nominal μ value generated.
- Plot the quantity $(\mu_{meas} - \mu)/\sigma_{meas}$. The optimal fit procedure should produce a gaussian-shaped distribution centred in zero.

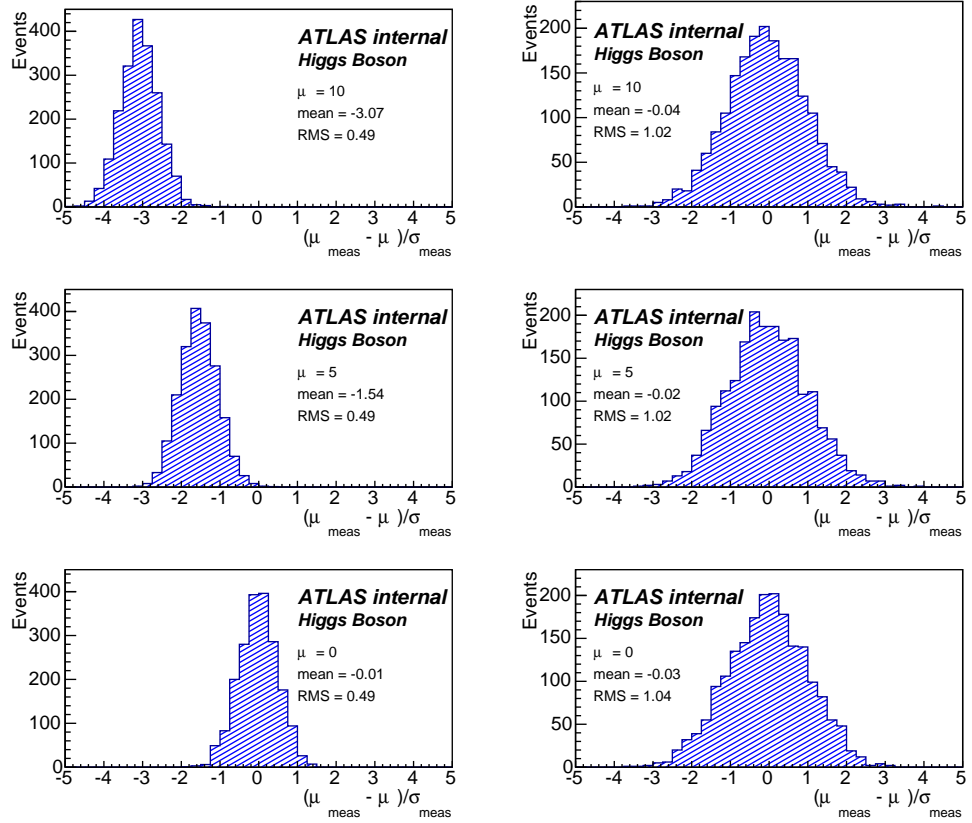


Figure 4.3: Comparison between the two fit methods: the “side-bands procedure” (left) and the “full-range procedure” (right). The former presents a bias that increases linearly with the Higgs μ generated. We performed for each 2000 MC samples.

We performed this study utilizing the data pull over the full BDT spectrum covered by the four retained regions – the generality of the methodology applies also to the BDT slices case. The fitting function consists of three components: a background model and the resonant pdfs. We repeated this methodology changing a few degrees of freedom: the strength μ of the Higgs Bosons during the pseudo-experiment simulation; and the background models. All these simulations produced the same outcome. The “side-bands procedure” mistakes the Higgs events in the side-bands for background and/or Z^0 events and this produces an underestimation of the Higgs strength. The higher the μ generated, the more events are in the side-bands, and the greater this bias becomes. However, a larger blind region would make the Z^0 estimate impossible. Conversely, the fit over the full $m_{b\bar{b}}$ spectrum produces unbiased results.

For clarity we reported on figure 4.3 only one of our tests, were we compare the outcome of the two methods for different μ values: the fit over the full $m_{b\bar{b}}$ spectrum represents the best strategy for a correct signal extrapolation. We then retain the fit over the full range as the optimal strategy. In order to keep the analysis blind we will keep hidden the fitted

signal strength (μ_H).

4.2 Combinatorial backgrounds

The full m_{bb} spectrum analysed covers the range $70 < m_{b\bar{b}} < 300$ GeV. The region from 70 GeV to 160 GeV will determine the magnitude of the resonant contributions, the additional $m_{b\bar{b}}$ range, being completely signal-free, will define the combinatorial background shape. We excluded the turn-on region – i.e. the range $m_{b\bar{b}} < 70$ GeV – that would complicate the background parametrization. We considered several functions for the background description. Using these candidates and the MC pdfs of the resonant processes, we performed a fit over the entire $m_{b\bar{b}}$ range; we found only a few could describe the background shape:

- The linear combination of exponentials

$$f(x) = a_0 e^{-\frac{x}{a_1}} - e^{-\frac{x}{a_2}} \quad (4.2)$$

where we indicated as a_0 , a_1 and a_2 some real positive variables and as x the observable, i.e. $m_{b\bar{b}}$.

- Bernstein polynomials of different order n . Given $x \in [a, b]$ these are defined as

$$B_n(x) = \sum_{\nu=0}^n \beta_\nu \binom{n}{\nu} \frac{(x-a)^\nu (b-x)^{n-\nu}}{(b-a)^n} \quad (4.3)$$

with β_ν the Bernstein coefficients.

We analyzed each region separately. We selected for each BDT region a different background model (rather than using the same function) and provided both a candidate and an alternative background model. Their choice based on two considerations: the probability associated to the χ^2 values and bias studies. The latter consists in assessing the biases introduced, during the fitting procedure, when parametrizing the background with different pdfs. Running Monte Carlo simulations, we produced the physic components and a background sample with a specific model, and fitted it with the alternative description. We compared the bias on the Higgs signal strength μ_{Bias} ¹ with the statistical error μ_{stat} . We retained only the functions with a $\mathcal{P}(\chi^2, dof) > 0.05$ and with a bias on the Higgs signal strength μ smaller than its statistical error. We took the candidate with less free-parameters. Table 4.3 summarizes the results.

4.3 Signals determination

The simultaneous fit over the four regions extrapolated the signal strength, normalized to the SM expected Higgs yield. Table 4.3 lists the functions

¹ μ is the scaling factor for the Higgs cross section

		$\mathcal{P}(\chi^2, dof)$			
		BDT Region	Function	χ^2	dof
Background Candidates	Region I	Exponentials	138.09	40	~ 0 [%]
		Bernstein 2 nd	416.17	40	~ 0 [%]
		Bernstein 3 rd	78.66	39	0.03 [%]
		Bernstein 4 th	43.35	38	29.10 [%]
		Bernstein 5 th	39.88	37	38.65 [%]
	Region II	Exponentials	71.10	40	0.24 [%]
		Bernstein 2 nd	129.96	40	~ 0 [%]
		Bernstein 3 rd	57.013	39	3.95 [%]
		Bernstein 4 th	47.42	38	16.69 [%]
		Bernstein 5 th	47.30	37	14.33 [%]
	Region III	Exponentials	44.72	40	31.82 [%]
		Bernstein 2 nd	56.01	40	5.92 [%]
		Bernstein 3 rd	42.78	39	35.26 [%]
		Bernstein 4 th	41.55	38	36.04 [%]
		Bernstein 5 th	33.60	37	67.30 [%]
	Region IV	Exponentials	32.67	40	82.00 [%]
		Bernstein 2 nd	33.37	40	79.59 [%]
		Bernstein 3 rd	32.43	39	79.69 [%]
		Bernstein 4 th	31.69	38	79.09 [%]
		Bernstein 5 th	31.69	37	75.52 [%]

Configuration	BDT Region	Background Model	$\mathcal{P}(\chi^2, dof)$	Alternative Model	$\mathcal{P}(\chi^2, dof)$
	Region I	4 th	29.10 [%]	5 th	38.65 [%]
	Region II	4 th	16.69 [%]	5 th	14.33 [%]
	Region III	3 rd	35.26 [%]	Exponentials	31.82 [%]
	Region IV	2 nd	79.59 [%]	3 rd	79.69 [%]

Table 4.3: This table lists the χ^2 and the probabilities associated for very background candidate we took into consideration. For every region we proposed a background model and an alternative description.

used in each region to model the background. The analysis is still blind – we do not have the correct pdf for the Z contribution –, thus we keep the μ values hidden. The Z^0 MC sample will provide the correct BDT and $m_{b\bar{b}}$ spectrums, allowing us to evaluate the strength of both the signals. However, we can assess the statistical uncertainty:

$$\mu_H = \frac{\sigma_H}{\sigma_H^{SM}} = \mu \pm 1.8 \quad (4.4)$$

Figure 4.4 shows the results of the simultaneous fit in the four BDT regions, where the blind region has been set to zero; we highlighted the Z^0 boson in red.

4.4 Systematic uncertainties

The assessment of the systematic uncertainties has been performed using the standard approach. However, we plan to incorporate them in the fit using the profile likelihood approach, in order for the results to be easily compared with other experiments/searches. This analysis receives systematic contributions from several sources:

- **Fit function choice:** It is related to the fact the background model we used may not be the one that best describe the data.
- **b -tagging uncertainty:** It impacts the signal yield. The b -tagging calibration is available in form of ratio (scale factor) between efficiency measured in real data divided by MC efficiency as a function of the relevant kinematic variables of the jet (p_T and η). The b -tagging scale factors will be added as a nuisance parameters for the b -jet efficiency for both Z and Higgs Monte Carlo.
- **Jet energy scale and resolution:** Uncertainties in the jet energy scale and resolution change the four vectors of the jets in the final state distorting the $m_{b\bar{b}}$ shape for both Z and Higgs signal. Moreover the change in the jet energy scale modifies the value of the BDT output and hence can cause migration of events between BDT categories.
- **Theory:** Uncertainties in the vector boson fusion and gluon fusion cross sections.

Table 4.4 lists these sources and the magnitude of their contributions to the final results.

4.4.1 Background-modelling uncertainty

The background-modelling systematics is introduced when the background parametrization used do not reflect the one the data follow. We evaluated how a wrong choice of the background modelling influences the signal strength by means of Monte Carlo simulations.

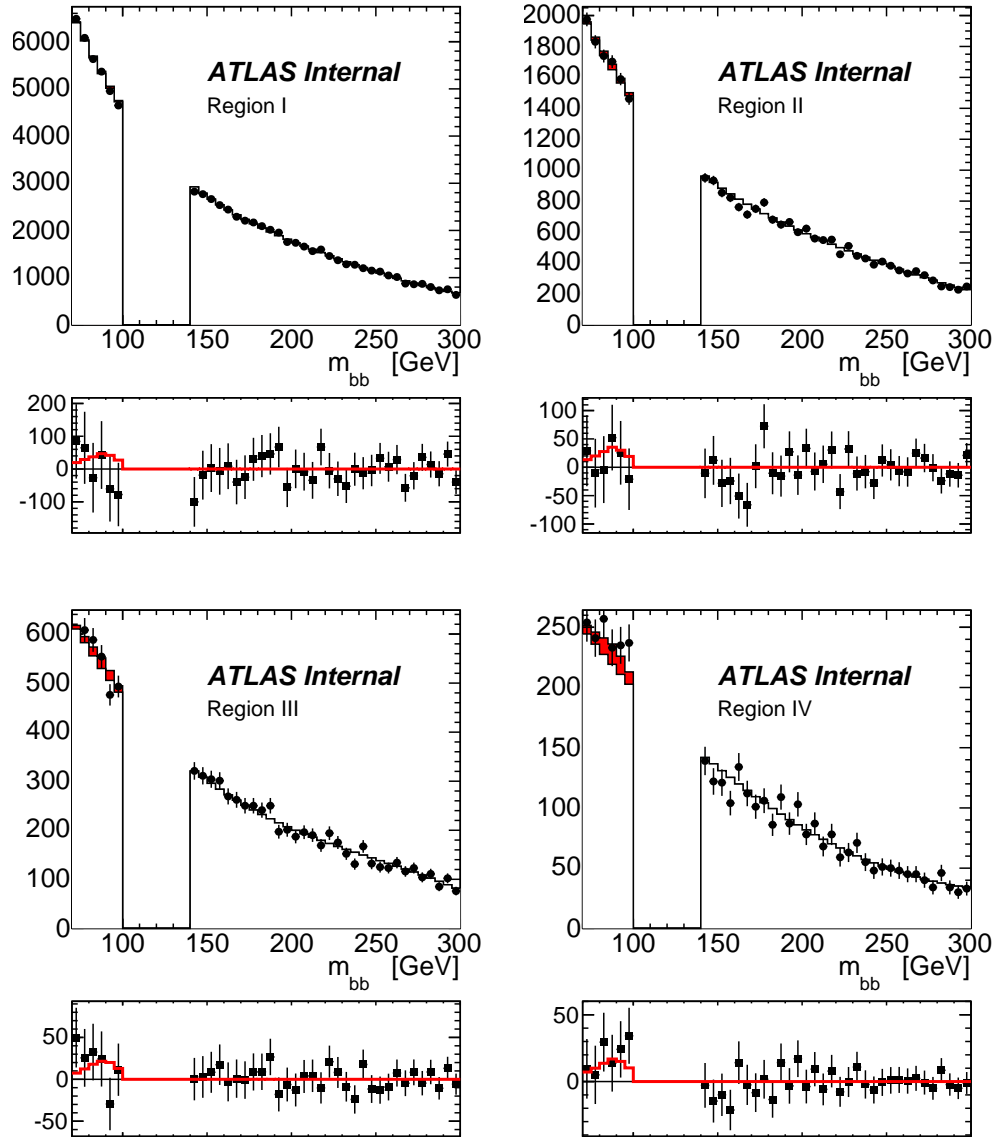


Figure 4.4: Results of the simultaneous fit over the four BDT regions. The top plots show the data pull in each region, the bottom plots show the difference between the data and the fitted combinatorial background. In red is highlighted the Z^0 boson.

Source	Uncertainty contribution
bkg-modelling	7.2 %
b -tagging	5.6 %
JES	19.2 %
Theory	5.0 %
Total uncertainty	21.8 %

Table 4.4: *The list of the systematics uncertainties we calculated, and the combination of their contributions.*

- We generated several MC experiments. For three of the four BDT regions we used the background description as listed in table 4.3, for the fourth region the alternative model.
- We performed two simultaneous fits: one using the same background model configuration used in the generation process, another using the designed background models configuration of table 4.3. In both cases we extrapolate the μ_{meas} value.
- We repeated the previous operations three times, using the alternative background model in a different region. Every time the systematic contributions is taken to be the difference between the calculated μ values.

The systematic uncertainty is obtained combining these four independent contributions. The procedure produced a systematic error of $\sigma_{bkg}(\mu) = 7.2 \%$.

4.4.2 b -tagging uncertainty

The uncertainty on the b -tagging efficiency only affects the signal statistics, leaving unchanged its template. As a consequence, it effects only the μ value and can be easily computed. Combining the systematic contributions for both the ggF and the VBF sample with a weighted sum, the resulting systematic uncertainty results:

$$\sigma_{b-tag} = \sqrt{\sigma_{VBF}^2 + \sigma_{ggF}^2} = 13 \text{ events } [5.6\%] \quad (4.5)$$

4.4.3 Jet-Energy-Scale uncertainty

The calorimeters jet response needs to be corrected for different effects: non-compensating calorimeters; energy losses in inactive regions of the detector; particles leakage; out-of-cone effects; and inefficiencies in calorimeter clustering and jet reconstruction. The Jet Energy Scale (JES) correction aims at recovering the true 4-vector of the jets measured in the calorimeter [85]. It consists in a jet by jet correction applied as a function of the momentum and $|\eta|$.

We calculated this systematic contribution following the recommendation from the ATLAS group. They require to assess the JES systematics through the splitting of the nuisance parameters coming from the various in-situ techniques – these parameters are propagated through the analysis separately in order to maintain the full information on correlations. A reduced set of nuisance parameters involves 14 variables:

- 6 from the reduction of the in-situ analyses nuisance parameters
- 2 from η intercalibration (modeling and statistics)
- 1 from the behaviour of high-pT jets in propagation of single hadron uncertainties to jet
- 1 from MC non-closure
- 4 from pile-up

Hence, we varied one parameter at a time of $\pm 1\sigma$ and produced the MC simulation of the resonant processes. The resulting signal templates were used to evaluate how much the signal strength change, by fitting the real data. The systematic uncertainty is taken to be the signal strength difference; thus, each changed nuisance parameter produces two uncertainties: σ_i^+ and σ_i^- . We symmetrized these values: the uncertainty for the nuisance parameter i is given by:

$$\begin{aligned} \sigma_i &\equiv \frac{1}{2} (\sigma_i^+ - \sigma_i^-) && \text{if } \sigma_i^+ \text{ and } \sigma_i^- \text{ have opposite sign} \\ \sigma_i &\equiv \frac{1}{2} (|\sigma_i^+| + |\sigma_i^-|) \text{ sign}(\sigma_i^+) && \text{if } \sigma_i^+ \text{ and } \sigma_i^- \text{ have same sign} \end{aligned} \quad (4.6)$$

The JES systematic is obtained combining these 14 independent contributions. The total JES uncertainty obtained is $\sigma_{JES}(\mu) = 19.2\%$.

4.4.4 Theory uncertainty

The uncertainties on the Higgs cross-section and the $H \rightarrow b\bar{b}$ branching ratio affect the signal strength. The assessment of their systematic contribution is derived from table 1.5, provided by the Higgs cross section group. Combining these systematic contributions with a weighted sum, the resulting systematic uncertainty turns out to be

$$\sigma_{Theory} = \sqrt{\sigma_{VBF}^2 + \sigma_{ggF}^2} = 12 \text{ events } [5.0\%] \quad (4.7)$$

This procedure is naive. These uncertainties affect both the template and the statistics of the Monte Carlo samples. The correct assessment of these effects will be performed in the near future with MC simulations.

4.5 Comparison with CMS

Throughout this analysis we constantly compared our results with those the CMS collaboration obtained. Their study was taken as a guideline and as a parameter of comparison. Like us, they exploited Multivariate analysis techniques, used the output as the discriminating variable, and parametrized the background with a Bernstein polynomial. Unlike us, they exploited an Artificial Neural Network (ANN) – instead of a Boosted Decision Tree –, and they fixed the Z^0 contribution to the SM expectations – instead of leaving it a floating parameter. Their ANN output possesses more discriminant power than our BDT output. Together with the difference in the fit procedure and a more sophisticated quark/gluon tagger, this leads the CMS to have a better limit than us. With our analysis we reached a $\sigma_{stat}(\mu)$ value of 1.8, while they obtained a signal strength of:

$$\mu_H = \frac{\sigma_H}{\sigma_H^{SM}} = 0.7 \pm 1.4 \text{ (stat)} \quad (4.8)$$

Table 4.5 compares the expected signal and the real background events in each MVA slice and shows the lack in statistics we have. However, the ATLAS and the CMS performances are equivalent. The different results can be explained by a different acceptance, caused by the trigger performances of the experiments.

70 < $m_{b\bar{b}}$ < 250 GeV				
ATLAS	Bkg	VBF H	ggF H	ggF/VBF
Region 0	2.2e+5	18	51	289.0 [%]
Region I	1.1e+5	40	26	65.5 [%]
Region II	3.4e+4	38	9	24.1 [%]
Region III	1.1e+4	27	3	9.6 [%]
Region IV	4.8e+3	22	2	7.1 [%]

Expected signal in the overall BDT region				
ATLAS	3.8e+5	145	91	62.7 [%]

Expected signal in the $-0.07 < BDT < 1.00$ region				
ATLAS	1.6e+5	127	39	31.0 [%]

70 < $m_{b\bar{b}}$ < 250 GeV				
CMS	Bkg	VBF H	ggF H	ggF/VBF [%]
Region 0	1.9e+6	66	94	142.4 [%]
Region I	3.2e+5	79	37	46.8 [%]
Region II	1.1e+5	85	18	21.2 [%]
Region III	2.7e+4	49	6	12.2 [%]
Region IV	8.7e+3	33	2	6.1 [%]

Expected signal in the overall ANN region				
CMS	2.4e+6	312	157	50.3 [%]

Expected signal in the $0.52 < ANN < 1.00$ region				
CMS	4.7e+5	246	63	25.6 [%]

Table 4.5: Comparison between the ATLAS and the CMS results. The table shows the number of background and signal events in each region, and the corresponding ratio between the ggF- and VBF- produced Higgs bosons.

Conclusions

I carried out this thesis work in the ATLAS Collaboration, in close contact with researchers from several international organizations. I contributed to a search with the ATLAS detector for the Standard Model Higgs boson produced by vector boson fusion and decaying to a $b\bar{b}$ pair, using $\sim 20 \text{ fb}^{-1}$ of LHC proton-proton data at $\sqrt{S} = 8 \text{ TeV}$ collected during the 2012 data-taking period. This is the first search in ATLAS for this channels; it will add important information that will provide more precise measurements of the Higgs boson properties.

We can summarize my contribution in a few points. In the first stage of the analysis I selected the event candidates in order to isolate the interesting events. After a cut-based preselection, I exploited Multivariate Analysis techniques; amidst all the available tools I selected a Boosted Decision Tree, as it provides the greatest discriminant power. Its use raised the overall signal significance of the data pull.

I identified the optimum analysis strategy: a fit over the full $m_{b\bar{b}}$ spectrum that produces unbiased results for both the Z^0 and the Higgs boson.

I defined four independent BDT regions on which I performed a simultaneous fit extrapolating the signal strength. Eventually I assessed the main systematic uncertainties.

Right now we have obtained a signal strength statistical uncertainty, normalized to the expected SM prediction, of $\sigma_\mu(stat) = 1.8$ and a systematic uncertainty, obtained with the standard approach, of $\sigma_\mu(syst) = 0.2$ – it results negligible if compared to the statistical one. The analysis is not over yet. In the near future we plan to bring several improvements: finalize the production of the Z^0 MC simulation; evaluate the other systematics contributions, incorporating them in the fit using the profile likelihood approach for result comparison between experiments; and calculate the confidence limits with the CLs method [86, 87, 88].

CONCLUSIONS

ATLAS coordinate system

ATLAS uses a right-handed cartesian coordinate system: the origin lies at the nominal interaction point, the z -axis coincides with the two colliding protons beams and the x -axis points to the center of the LEP/LHC ring. Due to the accelerating tunnel tilt, the x - y - z axis are not at right angles but the y -axis slopes from vertical with a 0.7° angle.

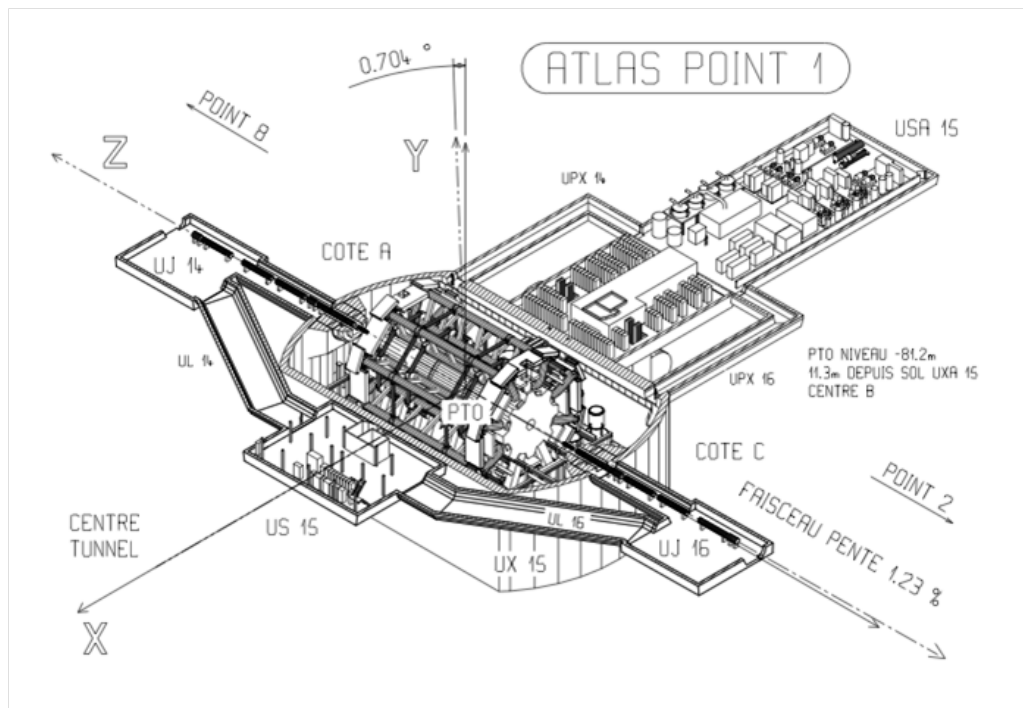


Figure A.1: A scheme of the ATLAS cartesian right-handed coordinate system. The general tilt of the LEP/LHC tunnel causes the y -axis to be slightly different from vertical. Figure taken by [89].

Spherical coordinates are more practical, and widely used. The azimuthal angle ϕ lies in the transverse plane, and the polar angle θ defines the angle from the beam axis. However, in High Energy Physics the pseudorapidity η is used instead of the latter and the transfer momentum defines the

vector modulus. This system is very convenient: what we measure in the experiment is the transverse momentum of particles and their production distribution is almost flat in η .

$$(x, y, z) \rightarrow (p_T, \eta, \phi) \quad (\text{A.1})$$

This angular quantity, the pseudorapidity, is an adimensional spatial coordinate defined as

$$\eta = -\ln \left[\tan \left(\frac{\theta}{2} \right) \right] \quad (\text{A.2})$$

which, expressed in terms of the three-dimensional momentum \mathbf{p} of the particle, assumes the form

$$\eta = \frac{1}{2} \ln \left(\frac{|\mathbf{p}| + p_L}{|\mathbf{p}| - p_L} \right) \quad (\text{A.3})$$

where p_L is the longitudinal momentum. In the limit where the particle is travelling close to the speed of light, or in the approximation that the mass of the particle is nearly zero, it is numerically equivalent to the experimental particle physicist's definition of rapidity but differs slightly from its definition in special relativity. Figure A.2 shows the correspondance between the polar angle θ and the pseudorapidity η .

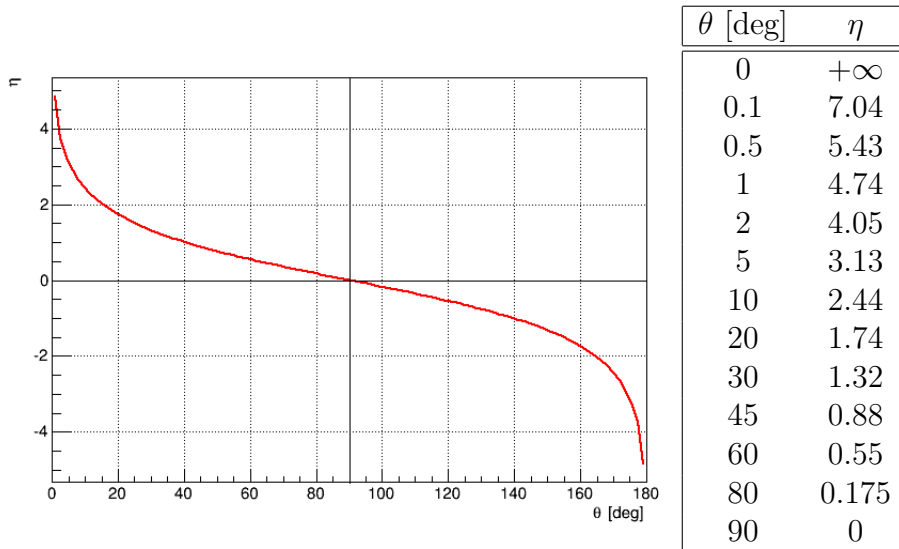


Figure A.2: Correspondance between the polar angle θ and the pseudorapidity in the range $\theta \in (0, 180)$ [deg]. Since the function is anti-symmetric with respect to 90° in the table are shown only the values in the range $\theta \in (0, 90)$ [deg].

b-tagging

With *b*-tagging selection we mean the identification of jets that originate from the fragmentation and the hadronization of bottom quarks. Isolate *b*- from light- and/or gluon-jets is basic in top physics, Higgs boson searches and new phenomena studies [90]; thus it constitutes a fundamental component of the ATLAS physics programme.

The tagging algorithms exploit the long lifetime, the hard fragmentation¹, and the invariant mass of B hadrons. They rely on the event topology, i.e. the presence of a displaced vertex, with respect to the point where the hard scatter collision occurred. These are divided according to the B hadrons physical properties they use: algorithms that exploit the transverse and longitudinal impact parameters; and algorithms that reconstruct the secondary vertices. As a consequence, the *b*-tagging selection strongly depends on the accuracy of the track reconstruction, the impact parameters being computed with respect to the selected primary vertex.

IP3D is the impact parameter-based algorithm ATLAS uses. It takes the transverse and the longitudinal impact parameters, and their correlation as input variables. Combining the two impact parameters significances, with a log-likelihood approach, it can distinguish between B hadron decay products and light-quarks tracks: the former have large impact parameters, the latter originate from the primary vertex.

ATLAS uses also SV1 [91, 92], i.e. an algorithm that reconstructs the secondary vertex using the likelihood ratio formalism. It exploits three of the vertex properties: the invariant mass of all tracks used to reconstruct the vertex; the ratio of the sum of the energies of these tracks to the sum of the energies of all tracks in the jet; and the number of two-track vertices. In addition, the ΔR between the jet direction and the direction of the line joining the primary vertex and the secondary vertex is used to reject secondary interactions in material. SV1 relies on a two-dimensional distribution of the two first variables and on two one-dimensional distributions of the latter variables.

¹A B hadron travels on average $\langle l \rangle = \beta\gamma c\tau \approx 3 \text{ mm}$ in the transverse plane for $p_T = 50 \text{ GeV}$ and retains $\sim 70\%$ of the original *b*-quark momentum.

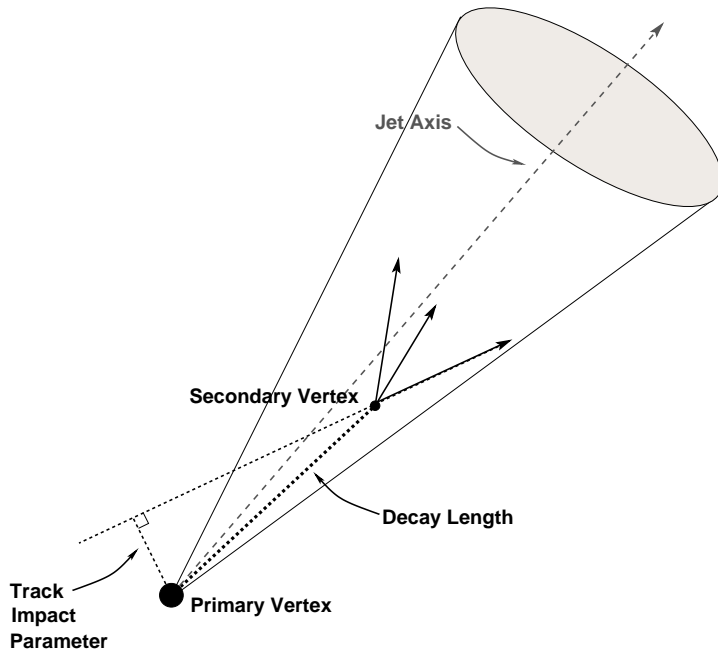


Figure B.1: A secondary vertex with a significant decay length indicates the presence of a long-lived particle in the jet. The secondary vertex is reconstructed from tracks with a large impact parameter significance with respect to the primary vertex. Image taken from reference [91].

Eventually, the `JetFitter` algorithm reconstructs the complete b -hadron decay chain, exploiting the topological structure of weak b - and c -hadron decay inside jet. It uses a Kalman filter [93] to find a common line from the primary vertex, through the b vertex, to the vertex decay chain. Thus, it separates b - and c -hadron vertices. This algorithm gathers eight variables in an artificial neural network and produces three output nodes, corresponding to the b -, c - and light-flavour jet hypotheses. The input variables are:

- Number of vertices with at least two tracks
- Total number of tracks at these vertices
- Number of additional single track vertices on the b -hadron flight axis.
- The invariant mass of all charged particle tracks attached to the decay chain.
- The energy of these charged particles divided by the sum of the energy of all charged particles associated to the jet.
- The weighted average vertex position divided by its error
- p^T and η , since the preceding input variables depends on them.

The vertex-based algorithms exhibit much lower mistag rates than the impact parameter-based ones, but the secondary vertex finding accuracy

limits their efficiency for b -jets. Tagging algorithms resulting from the combination of these approaches prove to be more versatile and powerful. ATLAS uses one of these: the MV1 algorithm [94, 95, 96, 97, 98]. This neural network combines the output of IP3D, SV1 and IP3D+JetFitter² exploiting the little correlations between the IP3D and the secondary vertex-based weights, together with the different correlations for b -jet and the light-jet samples of SV1 and IP3D+JetFitter weight. It produces a discriminant variable w such that jets with higher w are more likely to be b -jets. The training phase relies on a back-propagation algorithm and is based on two simulated samples of b -jets (signal hypothesis) and light jets (background hypothesis) obtained from simulated $t\bar{t}$ events. Table B.1 schematizes the MV1 configurations, with the corresponding efficiency, sample purity and reject factors.

Name	weight cut	b-jet efficiency	purity	c RF	tau RF	light RF
MV190	0.0616	89.97 [%]	59.34 [%]	1.75	1.56	2.97
MV185	0.1644	85.00 [%]	77.44 [%]	2.38	2.93	10.29
MV180	0.3900	80.00 [%]	85.76 [%]	3.09	5.64	27.13
MV175	0.6065	75.00 [%]	90.02 [%]	3.96	9.05	65.98
MV170	0.8119	70.00 [%]	92.43 [%]	4.99	14.07	150.00
MV165	0.9550	65.00 [%]	93.88 [%]	6.27	19.05	321.15
MV160	0.9867	60.00 [%]	94.95 [%]	7.98	25.21	651.81
MV157	0.990675	57.00 [%]	95.49 [%]	9.31	30.08	984.71
MV155	0.991711	55.00 [%]	95.83 [%]	10.37	33.87	1298.05
MV150	0.992515446	50.00 [%]	96.59 [%]	13.86	46.25	2545.27
MV145	0.992643775	45.00 [%]	97.26 [%]	19.06	64.47	4915.86
MV140	0.992665769	40.00 [%]	97.90 [%]	27.78	100.81	9591.62
MV135	0.992669703	35.00 [%]	98.52 [%]	43.72	211.38	17813.01
MV130	0.992670537	30.00 [%]	99.07 [%]	77.89	872.37	33908.80

Table B.1: Table summarizing the b -tagging Benchmarks, last updated on Nov 2012. This values have been extracted from a top-pair sample and are not necessarily the same for other samples. The above sample suffered from the HERWIG lifetime bug. This affect the b -jet efficiencies only very marginally, but the light-jet rejection numbers are not to be considered very reliable. Data taken from <https://twiki.cern.ch/twiki/bin/viewauth/AtlasProtected/BTaggingBenchmarks>.

²The IP3D+JetFitter algorithm is the JetFitter algorithm itself, with the IP3D output weight as an additional input node. It is also referred to as JetFitterCombNN.

Monte Carlo Simulations

Having a theoretical description of high energy particle collisions represents an essential component of any High Energy Physics search. But, understanding the final states of these reactions proves to be a theoretical challenge. Physicists address the problem with Monte Carlo simulations – the best suited integration method since its accuracy is irrespective of the dimension of the phase space. These software packages are able to simulate a wide range of processes at the LHC. Their use assures: to extract a signal of new physics from the background of SM processes; to measure SM parameters; to compare their predictions to the data; to provide realistic input for the design of new experiments or for new selection or reconstruction procedures within an existing experiment.

The MC simulations for hard processes follow a determined sequence; the event generation consists of several steps: a primary hard subprocess; parton showers associated with the incoming and outgoing coloured participants in the subprocess; non-perturbative interactions, that convert the showers into outgoing hadrons and connect them to the incoming beam hadrons; secondary interactions that give rise to the underlying event; and the decay of the instable resonances.

The simulation begins producing the hard subprocesses, and generating partonic events according to their matrix elements and phase space. Calculated with the tree-level matrix elements, these are typically of leading-order (LO) and/or of next-to-leading-order (NLO) calculation. Being colored, the QCD partons emit gluons and these themselves radiate, leading to a parton cascade or shower. This step is simulated with a step-wise Markov chain, called a parton shower algorithm. Moreover, during an hadron-hadron collision, more than one pair of partons may interact with each other. These multiple interactions go on to produce additional partons throughout the event.

Hadron formation occur naturally as the endpoint of parton showering, when the typical scale of momentum transfers is low and the corresponding value of the QCD running coupling is large, i.e. at scales of order 1 GeV. In this regime QCD becomes strongly interacting and perturbation theory breaks down. A non-perturbative hadronization model replaces the per-

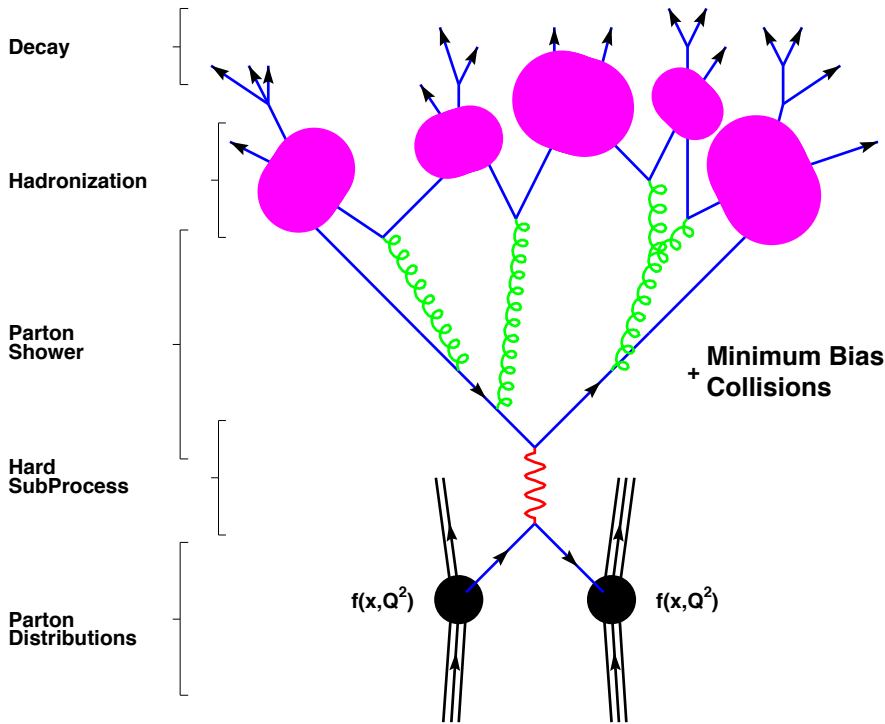


Figure C.1: Scheme that represents the Monte Carlo chain simulation. Image taken from reference [99].

turbative evolution: it describes the confinement of the system of coloured partons into colourless hadrons. In this regime individual partons do not hadronize independently, but rather colour-connected systems of partons hadronize collectively.

Then, many of the hadrons that are produced during hadronization are unstable resonances. Models are used to simulate their decay to the lighter hadrons that are long-lived enough to be considered stable on the time-scales of particle physics detectors. Finally, the digitization phase reproduces the detector response to the generated events, i.e. the response to the energy deposits. The output is equivalent to the real data.

It has become customary to use general-purpose event generators [100]. A physicist analysing hadron collider data obtains the most accurate theoretical predictions by combining components of many different simulation programs – minimum bias from one generator, signal process from another, and yet more programs for background generation. This diversification applies also for the generation of a single process: we use one program to produce a hard process; another to evolve the event through a parton shower algorithm; a third to hadronize the coloured products of the shower; and another to simulate the detector response. ATLAS exploits several Monte Carlo event generators. Amidst these we can name:

- **Powheg:** The Powheg program – acronym for Positive Weight Hardest

Emission Generator – is a general computer framework for implementing next-to-leading order QCD computations in shower Monte Carlo programs. It can be interfaced with all modern shower MC programs.

- **Pythia8:** It is a general-purpose event generator written in C++ language. The Pythia program includes a coherent set of physics models for the evolution from a few-body hard process to a complex multiparticle final state. Pythia provides a representation of event properties in a wide range of reactions, within and beyond the SM, with emphasis on those where strong interactions play a role, and therefore multihadronic final states are produced. The program is based on a combination of analytic results and various QCD-based models. It also has a set of utilities and several interfaces to external programs.
- **MadGraph:** MadGraph 5 is a general purpose matrix-element based event generator, written in the Python programming language. It features several output formats including C++ process libraries for Pythia 8, and full compatibility with FeynRules [101] for new physics models implementation, allowing for event generation for any model that can be written in the form of a Lagrangian.
- **Geant4:** Geant4 – i.e. GEometry ANd Tracking – is a toolkit for simulating the passage of particles through matter. Implemented in C++ programming language, it provides a complete range of functionality including tracking, geometry, physics models and hits. It covers several physics processes, including electromagnetic, hadronic and optical processes, a large set of long-lived particles, materials and elements, over a wide energy range, from 250 eV to the TeV energy scale. It can handle complex geometries.

Multivariate Analysis Techniques

The Multivariate Analysis techniques combine the individual discriminating power of some variables to create a single multivariate classifier. The cuts applied to their output provide a defined signal-to-background configuration. Several MVA algorithms exist. All of them require two data pulls in their input: a signal-only and a background-only sample. The n input variables define an n -dimensional space, the MVA techniques aim to build an n -dimensional surface able to separate between the regions that contain the signal from those that contain background, according to the values of the input variables. The differences between these algorithms lie in their complexity, the input variables handling, and the ability to exploit the variable correlations.

The MVA techniques follow the same procedure, consisting in two independent stages. The first stage consists in the classification, which trains and tests the MVA network. The training phase uses only half of the input events – randomly chosen – to build the n -dimensional surface separating the signal from the background, exploiting the knowledge of the event origin (signal or background). Eventually, the MVA algorithm produces a single classifier – as a function of the input variables – that discriminates between signal and background samples. The testing phase utilizes the remaining input events. It checks whether the n -dimensional surface built is too specific to the sample used during the training or not – the so-called overtraining, which occurs when a complex classifier is built using an input sample with an insufficient number of events. The overtraining worsens the MVA performance when it is applied to a different pull than the one used in the testing phase, thus the MVA wrongly classifies the events. The second stage consists in the application, where the MVA algorithm is applied to an independent sample.

During this search we took in consideration several algorithms: Boosted Decision Trees, Multi-Layers Perceptron Neural Network, LikelihoodPCA, and H-matrix. These methods are implemented in the ROOT-integrated [83] TMVA package [84].

D.1 Boosted Decision Tree

A Boosted Decision Tree is the ensemble of several Decision Trees (DT), i.e. binary tree-structured classifiers, as in figure D.1. A DT repeatedly takes left/right (yes/no) decisions on one single variable at a time until a stop criterion is fulfilled, hence splitting the phase space into a large number of hypercubes – identified as “signal-like” (S) or “background-like” (B), according to the majority of training events the leaf node contains.

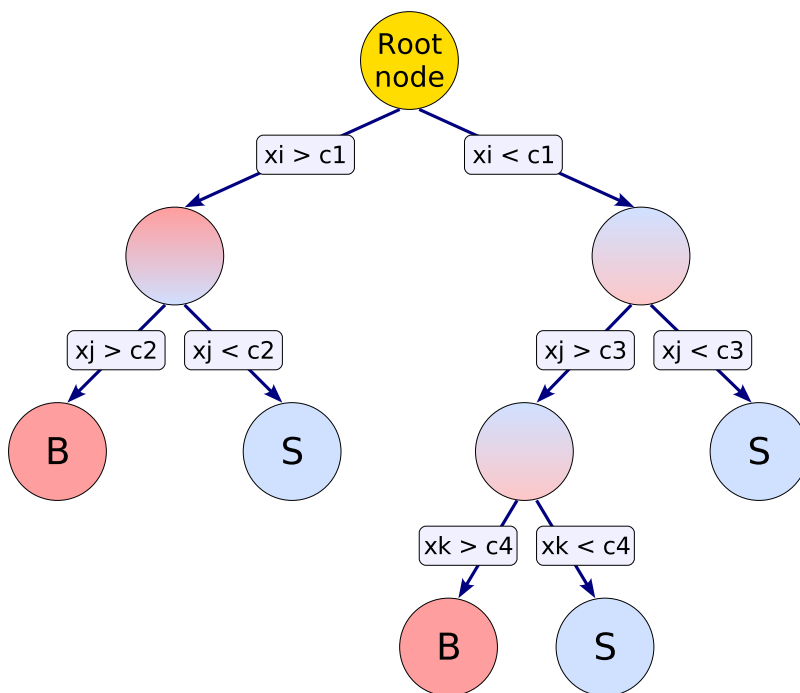


Figure D.1: *The structure of a Decision Tree. Starting from the root node, a sequence of binary splits using the discriminating variables x_i is applied. Each split uses the variable that at this node gives the best separation between signal and background when being cut on. The leaf nodes are labeled “S” for signal and “B” for background depending on the majority of events that end up in the nodes. Figure taken from reference [84]*

The training phase defines the splitting criteria for each decision node – from the root node to the leaves. It starts with an initial splitting criterion for the full training sample, and continues subjecting each subsets of training events to the same algorithm; hence determining the subsequent splitting iterations. This procedure is repeated until the whole tree is built. At each node, the splitting guarantees the best separation between signal and background. This is achieved by an accurate selection of the discriminating variable and cut value. The splitting selection criterion is determined

calculating the G_{ini} index:

$$G_{ini} \equiv \text{purity} (1 - \text{purity}) = \frac{SB}{(S + B)^2} \quad (\text{D.1})$$

where purity is defined as the ratio $S/(S + B)$. The greatest separation corresponds to the greatest reduction of this index, since it verges to zero when the training sample is dominated from one of the categories (S or B). Eventually, the leaf nodes are classified as signal or background according to the class the majority of events belongs to.

However, the instability with respect to statistical fluctuations in the training sample represents their shortcoming: if two input variables exhibit similar separation power, a fluctuation in the training sample may cause the tree growing algorithm to decide to split on one variable, while the other variable could have been selected without that fluctuation – this node affects the whole tree structure, resulting in a different classifier response. Boosted Decision Trees overcome the problem. They construct a forest of decision trees – each tree derived from the same training ensemble by reweighting events – and combine them into a single classifier with a weighted average of the individual decision trees, the so-called boosting. Boosting increases the statistical stability of the classifier and enhances the separation performance.

D.2 MultiLayers Perceptron Neural Network

An Artificial Neural Network processes the set of input signals by means of a network of inter-connected nodes, called “neurons”. The neural network constitutes a nonlinear mapping from a space of input variables x_1, \dots, x_n onto a one- or multi-dimensional space of output variables y_1, \dots, y_m . The layout of the neurons, the weights of the inter-neuron connections, and the neuron response function ρ – combination of a synaptic function $k : R_n \rightarrow R$ and an activation function $\alpha : R \rightarrow R$ – define the Neural Network behaviour.

MultiLayer Perceptrons Neural Networks (MLP) organize the neurons in layers, allowing connections between adjacent layers. Thus, they simplify the network structure, reducing the number of connections – a Neural Network with n input variables possess n^2 connections. The training phase maps these connections from the input layer, which holds the input values, to the output layer, which holds the estimator y_{ANN} . The other layers are hidden layers. For a classification problem, the Neural Networks possesses a first layer consisting of n_{var} neurons, and an output layer with a single node. The Neural Network builds the n -dimensional surface associating a weight w_{ij} to every connection.

The TMVA package utilizes the “back-propagation” algorithm [102, 103] in order to select the weights and optimise the classification performance. It is a supervised learning method, where the desired output for every input event is known (Bias). For background and signal events the desired outputs

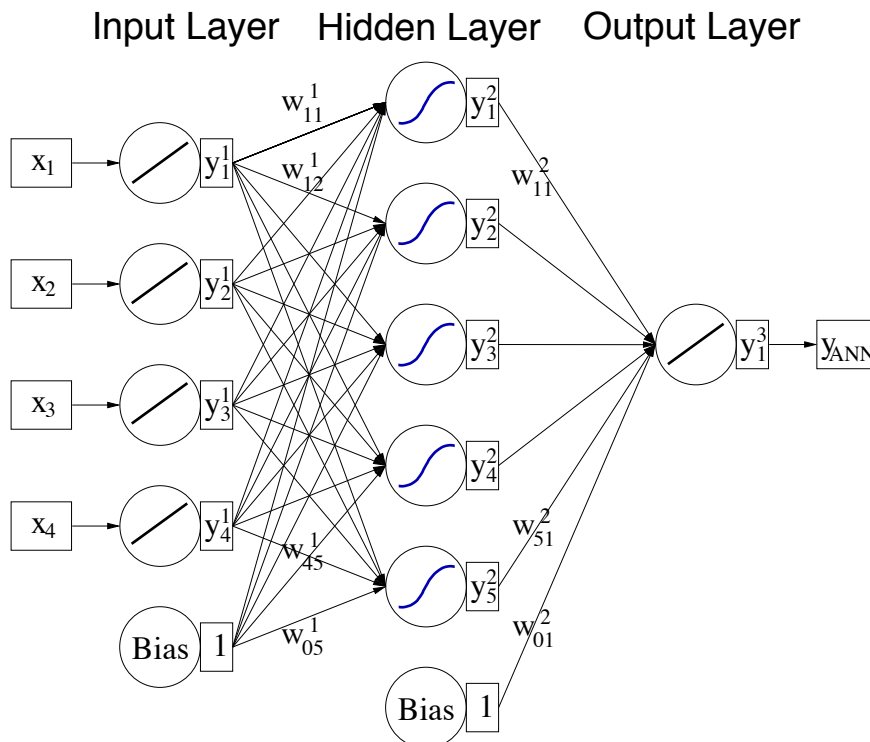


Figure D.2: Multilayer perceptron with one hidden layer. Figure taken from reference [84]

are zero and one. These operations are performed during the training phase exploiting several algorithms that minimize the deviation between the y_{ANN} outcome and the desired output. For an MLP with a single hidden layer, the output of the classifier is given by

$$y_{ANN} = \sum_{j=1}^{n_h} y_j^{(2)} w_{j1}^{(2)} = \sum_{j=1}^{n_h} \alpha \left(\sum_{i=1}^{n_{var}} x_i w_{ij}^{(1)} \right) w_{j1}^{(2)} \quad (\text{D.2})$$

where n_{var} and n_h are the number of neurons in the input layer and in the hidden layer respectively, $w_{ij}^{(1)}$ the weight between input-layer neuron i and hidden-layer neuron j , and $w_{j1}^{(2)}$ the weight between the hidden-layer neuron j and the output neuron.

D.3 LikelihoodPCA

This algorithm exploits the method of maximum likelihood [104], which consists of building a model out of probability density functions that reproduces the input variables for signal and background. It multiplies the signal probability densities of all input variables in order to construct the likelihood function for both signal (\mathcal{L}_S) and background (\mathcal{L}_B) and produces a likelihood ratio $y_{\mathcal{L}}(i)$ for each event i (peaked at zero and one for signal

and background events):

$$y_{\mathcal{L}}(i) \equiv \frac{\mathcal{L}_S}{\mathcal{L}_S + \mathcal{L}_B} \quad (\text{D.3})$$

This method ignores the correlations between the input variable; this affects its performance. The Principal Component Analysis (PCA) overcomes the problem: it performs an orthogonal transformation on the set of correlated variables, reducing them in a set of linearly uncorrelated variables giving more importance to those with the highest variance.

D.4 H-matrix discriminant

This Gaussian classifier [105, 106], the H-Matrix approach, assumes the correlated elements to be Gaussian distributed. The inverse of the covariance matrix is the H-Matrix. The algorithm exploits the differences in the mean values of the input elements between the two classes (signal and background) to create a multivariate χ^2 estimator. For an event i , it computes the χ^2 estimator for both signal (χ_S^2) and background (χ_B^2), using estimates for the sample means ($\bar{x}_{S,B,k}$) and covariance matrices ($C_{S,B}$) obtained from the training data

$$\chi_{S,B}^2(i) = \sum_{k,l=1}^{nvar} (x_k(i) - \bar{x}_{S,B,kl}) C_{S,B,kl}^{-1} (x_l(i) - \bar{x}_{S,B,l}) \quad (\text{D.4})$$

Thus, it computes the discriminant variable between the signal and background classes:

$$y_H(i) = \frac{\chi_B^2(i) - \chi_S^2(i)}{\chi_B^2(i) + \chi_S^2(i)} \quad (\text{D.5})$$

Acknowledgments

Siamo quindi giunti alla sezione dedicata ai ringraziamenti. Le persone che vorrei ringraziare sono molte, ma dato il tempo ristretto, cercherò di essere il più veloce possibile. Inizio ringraziando tutta la mia famiglia, dai parenti più stretti ai cugini sparsi per l'Italia e a quelli in giro per il mondo.

Vorrei ringraziare tutti coloro che mi hanno seguito durante questo lavoro di tesi: il gruppo ATLAS di Genova. Un gruppo stimolante, simpatico, che ti fa sentire parte di qualche cosa di importante. In particolare Fabrizio Parodi e Carlo Schiavi che mi hanno seguito durante il lavoro e mi hanno offerto tantissimi caffè – utilissimi per continuare a lavorare. Di certo non posso dimenticare i viaggi con Elisa, alle prese con il navigatore, con Claudia, alle prese con il cambio automatico, e con Stefano, pronto a puntualizzare. Impareggiabile. Vorrei inoltre ringraziare la Professoressa Carla Biggio, che si è interessata al mio lavoro e mi ha dato numerosi consigli.

Ringrazio i compagni di questo lungo viaggio. In particolare: Arturo (cosa avrei fatto a resistere durante le lezioni di italiano senza le nostre partite? O senza la nostra celeberrima poesia “N’è mai più d’amor povero Cugge”?); Elisa, che mi ha convinto persino a fare un corso di inglese; Alessandro (guai a te se non vieni a Parigi!), Lorenzo e Andrea Cab... Torchi con cui ho passato interminabili ore a ridere, scherzare, studiare e a spaccarmi la testa; Danilo e Diletta che hanno aggiunto quel pizzico di “Danilo” (non saprei come altro definirlo...); Luca Semeria e Jens per che non mi hanno amazzato durante le sessioni in laboratorio.

Infine un ringraziamento anche a Justin che involontariamente mi ha suggerito molte utili parole, che ho anche utilizzato in questa tesi.



List of Figures

1.1	Scheme of flavour symmetries of the $\mathbf{SU}(4)$ group: $\mathbf{4} \otimes \mathbf{4} \otimes \mathbf{4} = \mathbf{20}_S \oplus \mathbf{20}_{SM} \oplus \mathbf{20}_{AM} \oplus \mathbf{4}_A$: (a) the symmetric $\mathbf{20}_S$ of the $\mathbf{SU}(4)$ group, with the $\mathbf{SU}(3)$ decuplet on the lowest layer; (b) the mixed-symmetric $\mathbf{20}_S$, with the $\mathbf{SU}(3)$ octet on the lowest layer; (c) the antisymmetric $\mathbf{4}_A$, with the $\mathbf{SU}(3)$ singlet at the bottom. Image taken from reference [33]. . . .	9
1.2	The Higgs potential: $\mathcal{V} = \mu^2 \phi ^2 + \lambda \phi ^4$. With $\mu^2 < 0$ and $\lambda > 0$ the spontaneous symmetry breaking occurs. The minimum of the potential \mathcal{V} lies in a circle $\phi_0 = e^{i\alpha\theta}v/\sqrt{2}$ (where v is an $\mathbf{SU}(2)$ doublet constant with $ v = \sqrt{-\mu^2/\lambda}$): the vacuum state is chosen so that $\phi_0 = v/\sqrt{2}$, thus breaking the symmetry.	12
1.3	The Standard Model Higgs boson production cross sections at $\sqrt{S} = 8$ TeV for different Higgs mass values. Figure supplied by the Higgs Cross Section Working Group https://twiki.cern.ch/twiki/bin/view/LHCPhysics/CrossSections . . .	18
1.4	The Feynman diagrams representing the different production channels for the Higgs boson in proton-proton collision: gluon Fusion, Vector Boson Fusion, associate production with a intermediate vector boson and the associate production with a top pair.	18
1.5	The Standard Model Higgs boson decay branching ratios for different Higgs mass values. Figure supplied by the LHC Higgs Cross Section Working Group https://twiki.cern.ch/twiki/bin/view/LHCPhysics/CrossSections	19
1.6	The Feynman diagrams representing the Higgs boson decay channels at lowest orders: production of a $f\bar{f}$ pair ($f = b, \tau, c, \mu$), production of a weak vector boson pair, production of a gluon pair, and production of a $\gamma\gamma$ or a γZ^0 pair. .	19

2.1	A schematic of accelerator complex at CERN. Protons are accelerated by Linac, Booster, Proton Synchrotron (PS) and Super Proton Synchrotron (SPS). Protons are then guided into the LHC ring into two separated pipes, and eventually they collide where experiments are located. The LHC Technical Reports, in three volumes, are reported in references [46, 47, 48]	22
2.2	A detailed computer-generated image of the ATLAS detector and it's systems. Figure taken from http://www.atlas.ch/photos/index.html	24
2.3	Overview of the ATLAS Inner Detector and a scheme of the barrel sector, being crossed by one high-energy particle, with labels and dimensions. Figure taken from http://www.atlas.ch/photos/index.html	27
2.4	A computer generated image of the full ATLAS calorimeter. Figure taken from http://www.atlas.ch/photos/index.html	30
2.5	Overview of the ATLAS muon spectrometer components, labeled. Figure taken from http://www.atlas.ch/photos/index.html	34
2.6	A schematic of the ATLAS trigger + DAQ infrastructure. . .	36
3.1	The ATLAS luminosity in the 2011-2012 data taking period. In green, yellow and blue we have the delivered, recorded by the ATLAS detector, and useful luminosity. In 2011 it reached $\sim 5 fb^{-1}$, in 2012 $\sim 20 fb^{-1}$. Image taken from [69].	40
3.2	Feynman diagrams of the resonant processes involded: the production of an Higgs or Z^0 boson via Vector Boson Fusion; and the production of an Higgs boson via gluon-gluon Fusion. The final states have two b -jets, resulting from the decay of the bosons.	41
3.3	The $p_T^{\bar{b}b}$ cut removes the $m_{\bar{b}b}$ "double structure" of the data. In magenta the $m_{\bar{b}b}$ spectrum before this restraint, in red the data excluded, and in blue the retained events.	45
3.4	The input distributions used in the BDT training and testing phase. The BDT output variable will be the discriminating variable that will separate the background from the signal sample.	47
3.5	The results of the MVA analysis: the ROC curves of the Multivariate Analysis tecniqued we tested; and the BDT output, with training and testing sample superimposed. The overtraining check for the classifiers is performed with the Kolmogorov-Smirnov test [81, 82].	48
3.6	Values of the VBF significance for different BDT cuts. We reported both the $S/\sqrt{S+B}$ value and its error. The the maximum signal significance is 0.63, obtained imposing the cut $BDT > +0.04$	49

4.1	The BDT output, i.e. our discriminating variable. We defined four independent regions, but only four of them were retained, covering a total BDT range of $-0.07 < VFB < 1.00$.	53
4.2	The VBF-produced Higgs Boson template. The events in the side-bands ($\sim 20\%$ of the total Higgs events) explain the bias obtained with the side-bands fit procedure.	54
4.3	Comparison between the two fit methods: the “side-bands procedure” (left) and the “full-range procedure” (right). The former presents a bias that increases linearly with the Higgs μ generated. We performed for each 2000 MC samples.	55
4.4	Results of the simultaneous fit over the four BDT regions. The top plots show the data pull in each region, the bottom plots show the difference between the data and the fitted combinatorial background. In red is highlighted the Z^0 boson.	59
A.1	A scheme of the ATLAS cartesian right-handed coordinate system. The general tilt of the LEP/LHC tunnel causes the y-axis to be slightly different from vertical. Figure taken by [89].	67
A.2	Correspondance between the polar angle θ and the pseudo-rapidity in the range $\theta \in (0, 180)$ [deg]. Since the function is anti-symmetric with respect to 90° in the table are shown only the values in the range $\theta \in (0, 90)$ [deg].	68
B.1	A secondary vertex with a significant decay length indicates the presence of a long-lived particle in the jet. The secondary vertex is reconstructed from tracks with a large impact parameter significance with respect to the primary vertex. Image taken from reference [91].	70
C.1	Scheme that represents the Monte Carlo chain simulation. Image taken from reference [99].	74
D.1	The structure of a Decision Tree. Starting from the root node, a sequence of binary splits using the discriminating variables x_i is applied. Each split uses the variable that at this node gives the best separation between signal and background when being cut on. The leaf nodes are labeled “S” for signal and “B” for background depending on the majority of events that end up in the nodes. Figure taken from reference [84].	78
D.2	Multilayer perceptron with one hidden layer. Figure taken from reference [84].	80



List of Tables

1.1	Scheme of spin-1/2 particles that constitute matter: the six leptons – electron, muon, tau and the corresponding neutrinos –; and the six quarks – up, down, charm, strange, top (or truth) and bottom (or beauty). Data taken from references [20, 21, 7].	4
1.2	Overview of the very-fundamental constituent of matter and anti-matter, divided into the three families. Anti-matter particles have the same properties of their matter counterparts, but different charges (electric, hypercharge).	5
1.3	Scheme of the three forces described by the Standard Model with the corresponding spin-1 gauge particles (the force carriers). Data taken from references [21, 7].	5
1.4	Values of the completely antisymmetric structure constant f_{ijk} for different ijk combinations. Data taken from reference [36].	11
1.5	Cross sections and breaking ration for different Higgs mass values and at a center of mass energy of $\sqrt{S} = 8$ TeV. Data taken from references [8, 9].	16
2.1	General performance goals of the ATLAS detector. Units for E and p_T are in GeV.	26
2.2	Main parameters of the ATLAS inner detector: the Overall ID envelope, the Pixel detector, the SCT and the TRT. . . .	28
2.3	Main parameters of the ATLAS calorimeter systems.	32
3.1	The Monte Carlo samples used, with their simulation and reconstruction tags, and their sizes. They simulated both the Vector Boson Fusion- and the gluon-gluon Fusion-produced Higgs boson and the decay to a bottom quarks pair.	42
3.2	Summary of the cut-flows that both data and MC samples got past. The signal yields are normalized to those expected on the full used luminosity, according to the values of cross-section and \mathcal{BR} given by the theory.	43

3.3	The triggers used in this analysis for the 2012 data taking periods. The ATLAS trigger naming conventions – referring to the forthcoming Run-II triggers – can be found on https://twiki.cern.ch/twiki/bin/view/Atlas/TriggerNamingRun2 . The main concept remain unchanged even for Run-I triggers.	44
3.4	The input variable ranking. The top ranked is the most discriminating. We labelled with J_1 and J_2 the VBF-jets, sorted in η .	49
4.1	The BDT output cuts that define the four analysis regions and the significances. The assessment of the statistical error $\Sigma_{stat}(\mu)$ is an underestimation of the real value.	52
4.2	Table showing the number of signal – both ggF- and VBF-produced – and the number of background events, according to the BDT regions. The ratios ggF/VBF are reported.	53
4.3	This table lists the χ^2 and the probabilities associated for very background candidate we took into consideration. For every region we proposed a background model and an alternative description.	57
4.4	The list of the systematics uncertainties we calculated, and the combination of their contributions.	60
4.5	Comparison between the ATLAS and the CMS results. The table shows the number of background and signal events in each region, and the corresponding ration between the ggF- and VBF- produced Higgs bosons.	63
B.1	Table summarizing the b -tagging Benchmarks, last updated on Nov 2012. This values have been extracted from a top-pair sample and are not necessarily the same for other samples. The above sample suffered from the HERWIG lifetime bug. This affect the b -jet efficiencies only very marginally, but the light-jet rejection numbers are not to be considered very reliable. Data taken from https://twiki.cern.ch/twiki/bin/viewauth/AtlasProtected/BTaggingBenchmarks .	71

Bibliography

- [1] Georges Aad, T Abajyan, B Abbott, J Abdallah, S Abdel Khalek, AA Abdelalim, O Abdinov, R Aben, B Abi, M Abolins, et al. Observation of a new particle in the search for the standard model higgs boson with the atlas detector at the lhc. *Physics Letters B*, 716(1):1–29, 2012.
- [2] Serguei Chatrchyan, Vardan Khachatryan, Albert M Sirunyan, A Tumasyan, W Adam, E Aguilo, T Bergauer, M Dragicevic, J Erö, C Fabjan, et al. Observation of a new boson at a mass of 125 gev with the cms experiment at the lhc. *Physics Letters B*, 716(1):30–61, 2012.
- [3] ATLAS collaboration et al. Measurements of higgs boson production and couplings in diboson final states with the atlas detector at the lhc. *Physics Letters B*, 726(1):88–119, 2013.
- [4] Atlas Collaboration et al. Evidence for the spin-0 nature of the higgs boson using atlas data. *Physics Letters B*, 726(1):120–144, 2013.
- [5] Combination of standard model Higgs boson searches and measurements of the properties of the new boson with a mass near 125 GeV. Technical Report CMS-PAS-HIG-13-005, CERN, Geneva, 2013.
- [6] CERN press office. New results indicate that new particle is a Higgs boson. <http://home.web.cern.ch/about/updates/2013/03/new-results-indicate-new-particle-higgs-boson>, 2013.
- [7] KA Olive, Particle Data Group, et al. Review of particle physics. *Chinese Physics C*, 38(9):090001, 2014.
- [8] S Dittmaier, C Mariotti, G Passarino, R Tanaka, J Baglio, P Bolzoni, R Boughezal, O Brein, C Collins-Tooth, S Dawson, et al. Handbook of lhc higgs cross sections: 1. inclusive observables. *arXiv preprint arXiv:1101.0593*, 2011.
- [9] S Heinemeyer, C Mariotti, G Passarino, R Tanaka, JR Andersen, P Artoisenet, EA Bagnaschi, A Banfi, T Becher, FU Bernlochner, et al. Handbook of lhc higgs cross sections: 3. higgs properties. *arXiv preprint arXiv:1307.1347*, 2013.

-
- [10] CMS Collaboration et al. Search for the standard model higgs boson produced in vector boson fusion, and decaying to bottom quarks. *CMS Physics Analysis Summary CMS-PAS-HIG-13-011*, CERN, 2013.
- [11] Andrea Favareto, Elisa Guido, Leonardo Paolo Rossi, Fabrizio Parodi, Carlo Schiavi, and Carlo Varni. Search for the Standard Model Higgs boson produced by vector boson fusion and decaying to beauty quarks with the ATLAS detector. Technical Report ATL-COM-PHYS-2014-1430, CERN, Geneva, Nov 2014.
- [12] Young-Kee Kim, Karol Krizka, and Yasuyuki Okumura. Search for the Standard Model Higgs boson produced by vector boson fusion and decaying to beauty quarks with the ATLAS detector using the cut-based analysis. Technical Report ATL-COM-PHYS-2014-1548, CERN, Geneva, Dec 2014.
- [13] Sheldon L Glashow. Partial-symmetries of weak interactions. *Nuclear Physics*, 22(4):579–588, 1961.
- [14] Abdus Salam and John Clive Ward. On a gauge theory of elementary interactions. *Il Nuovo Cimento (1955-1965)*, 19(1):165–170, 1961.
- [15] Steven Weinberg. A model of leptons. *Phys. Rev. Lett.*, 19:1264–1266, Nov 1967.
- [16] Nobelprize.org. The Nobel Prize in Physics 1979. http://www.nobelprize.org/nobel_prizes/physics/laureates/1979/, 2014.
- [17] G Arnison, A Astbury, B Aubert, C Bacci, G Bauer, A Bezaguet, R Böck, TJV Bowcock, M Calvetti, T Carroll, et al. Experimental observation of isolated large transverse energy electrons with associated missing energy at $s = 540$ gev. *Physics Letters B*, 122(1):103–116, 1983.
- [18] M Banner, R Battiston, Ph Bloch, F Bonaudi, K Borer, M Borghini, J-C Chollet, AG Clark, C Conta, P Darriulat, et al. Observation of single isolated electrons of high transverse momentum in events with missing transverse energy at the cern pp collider. *Physics Letters B*, 122(5):476–485, 1983.
- [19] FJ Hasert, S Kabe, W Krenz, J Von Krogh, D Lanske, J Morfin, K Schultze, H Weerts, GH Bertrand-Coremans, J Sacton, et al. Observation of neutrino-like interactions without muon or electron in the gargamelle neutrino experiment. *Physics Letters B*, 46(1):138–140, 1973.
- [20] Carlo M Becchi and Giovanni Ridolfi. *An introduction to relativistic processes and the standard model of electroweak interactions*. Springer, 2006.

-
- [21] Juerg Beringer, JF Arguin, RM Barnett, K Copic, O Dahl, DE Groom, CJ Lin, J Lys, H Murayama, CG Wohl, et al. Review of particle physics. *Physical Review D*, 86(1), 2012.
- [22] CS Wu, E Ambler, RW Hayward, DD Hoppes, and RP Hudson. Experimental test of parity conservation in beta decay. *Phys. Rev.*, 104:1315, 1956.
- [23] G Arnison, A Astbury, B Aubert, C Bacci, G Bauer, A Bezaguet, R Böck, TJV Bowcock, M Calvetti, P Catz, et al. Experimental observation of lepton pairs of invariant mass around 95 gev/c^2 at the cern sps collider. *Physics Letters B*, 126(5):398–410, 1983.
- [24] Po Bagnaia, M Banner, R Battiston, Ph Bloch, F Bonaudi, K Borer, M Borghini, J-C Chollet, AG Clark, C Conta, et al. Evidence for $z^0 \rightarrow e^+e^-$ at the cern pp collider. *Physics Letters B*, 129(1):130–140, 1983.
- [25] Murray Gell-Mann. A schematic model of baryons and mesons. *Physics Letters*, 8(3):214–215, 1964.
- [26] G Zweig. An SU_3 model for strong interaction symmetry and its breaking; Version 2. (CERN-TH-412):80 p, Feb 1964. Version 1 is CERN preprint 8182/TH.401, Jan. 17, 1964.
- [27] Sheldon L Glashow, Jean Iliopoulos, and Luciano Maiani. Weak interactions with lepton-hadron symmetry. *Physical Review D*, 2(7):1285, 1970.
- [28] J. Aubert, U. Becker, P. Biggs, J. Burger, M. Chen, G. Everhart, P. Goldhagen, J. Leong, T. McCorriston, T. Rhoades, M. Rohde, Samuel Ting, Sau Wu, and Y. Lee. Experimental observation of a heavy particle j . *Phys. Rev. Lett.*, 33:1404–1406, Dec 1974.
- [29] J. Augustin, A. Boyarski, M. Breidenbach, F. Bulos, J. Dakin, G. Feldman, G. Fischer, D. Fryberger, G. Hanson, B. Jean-Marie, R. Larsen, V. Lüth, H. Lynch, D. Lyon, C. Morehouse, J. Paterson, M. Perl, B. Richter, P. Rapidis, R. Schwitters, W. Tanenbaum, F. Vannucci, G. Abrams, D. Briggs, W. Chinowsky, C. Friedberg, G. Goldhaber, R. Hollebeek, J. Kadyk, B. Lulu, F. Pierre, G. Trilling, J. Whitaker, J. Wiss, and J. Zipse. Discovery of a narrow resonance in e^+e^- annihilation. *Phys. Rev. Lett.*, 33:1406–1408, Dec 1974.
- [30] Kuang-Ta Chao, Nathan Isgur, and Gabriel Karl. Strangeness $^{-2}$ and $^{-3}$ baryons in a quark model with chromodynamics. *Phys. Rev. D*, 23:155–162, Jan 1981.
- [31] Nathan Isgur and Gabriel Karl. p . *Phys. Rev. D*, 18:4187–4205, Dec 1978.

-
- [32] Nathan Isgur and Gabriel Karl. Positive-parity excited baryons in a quark model with hyperfine interactions. *Phys. Rev. D*, 19:2653–2677, May 1979.
- [33] Volker Crede and Winston Roberts. Progress towards understanding baryon resonances. *Reports on Progress in Physics*, 76(7):076301, 2013.
- [34] Makoto Kobayashi and Toshihide Maskawa. Cp-violation in the renormalizable theory of weak interaction. *Progress of Theoretical Physics*, 49(2):652–657, 1973.
- [35] Nicola Cabibbo. Unitary symmetry and leptonic decays. *Physical Review Letters*, 10(12):531, 1963.
- [36] Franz Mandl and Graham Shaw. *Quantum field theory*. John Wiley & Sons, 2010.
- [37] Jeffrey Goldstone. Field theories with «superconductor» solutions. *Il Nuovo Cimento*, 19(1):154–164, 1961.
- [38] Jeffrey Goldstone, Abdus Salam, and Steven Weinberg. Broken symmetries. *Physical Review*, 127(3):965, 1962.
- [39] Yoichiro Nambu. Quasi-particles and gauge invariance in the theory of superconductivity. *Phys. Rev.*, 117:648–663, Feb 1960.
- [40] François Englert and Robert Brout. Broken symmetry and the mass of gauge vector mesons. *Physical Review Letters*, 13(9):321–323, 1964.
- [41] Peter W Higgs. Broken symmetries, massless particles and gauge fields. *Physics Letters*, 12(2):132–133, 1964.
- [42] Peter W Higgs. Spontaneous symmetry breakdown without massless bosons. *Physical Review*, 145(4):1156, 1966.
- [43] David Smith. Higgs boson searches at lep ii. 2000.
- [44] Higgs Working Group, CDF collaboration, D0 Collaboration, et al. Updated combination of cdf and d0 searches for standard model higgs boson production with up to 10.0 fb^{-1} of data. *arXiv preprint arXiv:1207.0449*, 2012.
- [45] Lyndon Evans and Philip Bryant. Lhc machine. *Journal of Instrumentation*, 3(08):S08001, 2008.
- [46] Oliver Sim Brüning, Paul Collier, P Lebrun, Stephen Myers, Ranko Ostojic, John Poole, and Paul Proudlock. *LHC Design Report*, volume 1. CERN, Geneva, 2004.

-
- [47] Oliver Sim Brüning, Paul Collier, P Lebrun, Stephen Myers, Ranko Ostojic, John Poole, and Paul Proudlock. *LHC Design Report*, volume 2. CERN, Geneva, 2004.
- [48] Michael Benedikt, Paul Collier, V Mertens, John Poole, and Karlheinz Schindl. *LHC Design Report*, volume 3. CERN, Geneva, 2004.
- [49] Georges Aad, E Abat, J Abdallah, AA Abdelalim, A Abdesselam, O Abdinov, BA Abi, M Abolins, H Abramowicz, E Acerbi, et al. The atlas experiment at the cern large hadron collider. *Journal of Instrumentation*, 3(08):S08003, 2008.
- [50] Atlas Collaboration et al. Atlas detector and physics performance technical design report. *CERN/LHCC*, 15:1999, 1999.
- [51] TDR ATLAS. 5, inner detector technical design report, vol. i. Technical report, CERN/LHCC/97-17, 30 April, 1997.
- [52] MS Alam, SB Athar, Z Ling, AH Mahmood, HS Severini, SC Timm, FR Wappler, E Anderssen, D Bintinger, A Ciocio, et al. Atlas pixel detector: Technical design report. 1998.
- [53] G Aad, M Ackers, FA Alberti, M Aleppo, G Alimonti, J Alonso, EC Anderssen, A Andreani, A Andreatza, JF Arguin, et al. Atlas pixel detector electronics and sensors. *Journal of Instrumentation*, 3(07):P07007, 2008.
- [54] ATLAS collaboration et al. The atlas inner detector commissioning and calibration. *arXiv preprint arXiv:1004.5293*, 2010.
- [55] M Capeans, G Darbo, K Einsweiler, M Elsing, T Flick, M Garcia-Sciveres, C Gemme, H Pernegger, O Rohne, and R Vuillermet. ATLAS Insertable B-Layer Technical Design Report. Technical Report CERN-LHCC-2010-013. ATLAS-TDR-19, CERN, Geneva, Sep 2010.
- [56] A Abdesselam, T Akimoto, PP Allport, J Alonso, B Anderson, L Andricek, F Anghinolfi, RJ Apsimon, G Barbier, AJ Barr, et al. The barrel modules of the atlas semiconductor tracker. *Nuclear Instruments and Methods in Physics Research Section A: Accelerators, Spectrometers, Detectors and Associated Equipment*, 568(2):642–671, 2006.
- [57] A Abdesselam, PJ Adkin, PP Allport, J Alonso, L Andricek, F Anghinolfi, AA Antonov, RJ Apsimon, T Atkinson, LE Batchelor, et al. The atlas semiconductor tracker end-cap module. *Nuclear Instruments and Methods in Physics Research Section A: Accelerators, Spectrometers, Detectors and Associated Equipment*, 575(3):353–389, 2007.
- [58] E Abat, TN Addy, TPA Åkesson, J Alison, F Anghinolfi, E Arik, M Arik, G Atoian, B Auerbach, OK Baker, et al. The atlas transition radiation tracker (trt) proportional drift tube: design and performance. *Journal of Instrumentation*, 3(02):P02013, 2008.

-
- [59] *ATLAS calorimeter performance: Technical Design Report*. Technical Design Report ATLAS. CERN, Geneva, 1996.
- [60] *ATLAS muon spectrometer: Technical Design Report*. Technical Design Report ATLAS. CERN, Geneva, 1997. distribution.
- [61] Georges Aad, B Abbott, J Abdallah, AA Abdelalim, A Abdesselam, O Abidinov, B Abi, M Abolins, H Abramowicz, H Abreu, et al. Performance of the atlas trigger system in 2010. *The European Physical Journal C*, 72(1):1–61, 2012.
- [62] Carolina Gabaldon. Performance of the atlas trigger system. *Journal of Instrumentation*, 7(01):C01092, 2012.
- [63] Christoph Eck, J Knobloch, Leslie Robertson, I Bird, K Bos, N Brook, D Düllmann, I Fisk, D Foster, B Gibbard, C Grandi, F Grey, J Harvey, A Heiss, F Hemmer, S Jarp, R Jones, D Kelsey, M Lamanna, H Marten, P Mato-Vila, F Ould-Saada, B Panzer-Steindel, L Perini, Y Schutz, U Schwickerath, J Shiers, and T Wenaus. *LHC computing Grid: Technical Design Report. Version 1.06 (20 Jun 2005)*. Technical Design Report LCG. CERN, Geneva, 2005.
- [64] Collaboration ATLAS, Torsten Åkesson, Paula Eerola, Vincent Hedberg, Göran Jarlskog, Björn Lundberg, Ulf Mjörnmark, Oxana Smirnova, Sverker Almehed, et al. Atlas computing: Technical design report. *LHCC Reports; ATLAS Technical Design Reports*, 2005.
- [65] GAUDI& Barrand, I Belyaev, P Binko, M Cattaneo, R Chytracsek, G Corti, M Frank, G Gracia, J Harvey, E van Herwijnen, et al. Gaudi—a software architecture and framework for building hep data processing applications. *Computer Physics Communications*, 140(1):45–55, 2001.
- [66] CERN press office. First beam in the LHC - accelerating science. <http://press.web.cern.ch/press-releases/2008/09/first-beam-lhc-accelerating-science>, 2008.
- [67] CERN press office. Incident in LHC sector 3-4. <http://press.web.cern.ch/press-releases/2008/09/incident-lhc-sector-3-4>, 2008.
- [68] CERN press office. Two circulating beams bring first collisions in the LHC. <http://press.web.cern.ch/press-releases/2009/11/two-circulating-beams-bring-first-collisions-lhc>, 2009.
- [69] ATLAS Public. Luminosity Public Results. https://twiki.cern.ch/twiki/bin/view/AtlasPublic/LuminosityPublicResults#Integrated_luminosity_summary_pl, 2013.

-
- [70] Stefano Frixione, Giovanni Ridolfi, and Paolo Nason. A positive-weight next-to-leading-order monte carlo for heavy flavour hadroproduction. *Journal of High Energy Physics*, 2007(09):126, 2007.
- [71] Stefano Frixione, Paolo Nason, and Giovanni Ridolfi. The powheg-hvq manual version 1.0. *arXiv preprint arXiv:0707.3081*, 2007.
- [72] Torbjörn Sjöstrand, Stephen Mrenna, and Peter Skands. A brief introduction to pythia 8.1. *Computer Physics Communications*, 178(11):852–867, 2008.
- [73] MadGraph Manual. Madevent: a multipurpose event generator powered by madgraph, 2007.
- [74] Sea Agostinelli, John Allison, K al Amako, J Apostolakis, H Araujo, P Arce, M Asai, D Axen, S Banerjee, G Barrand, et al. Geant4—a simulation toolkit. *Nuclear instruments and methods in physics research section A: Accelerators, Spectrometers, Detectors and Associated Equipment*, 506(3):250–303, 2003.
- [75] Hung-Liang Lai, Marco Guzzi, Joey Huston, Zhao Li, Pavel M Nadolsky, Jon Pumplin, and C-P Yuan. New parton distributions for collider physics. *Physical Review D*, 82(7):074024, 2010.
- [76] New ATLAS event generator tunes to 2010 data. Technical Report ATL-PHYS-PUB-2011-008, CERN, Geneva, Apr 2011.
- [77] ATLAS tunes of PYTHIA 6 and Pythia 8 for MC11. Technical Report ATL-PHYS-PUB-2011-009, CERN, Geneva, Jul 2011.
- [78] Georges Aad, B Abbott, J Abdallah, AA Abdelalim, A Abdesselam, O Abidinov, B Abi, M Abolins, H Abramowicz, H Abreu, et al. The atlas simulation infrastructure. *The European Physical Journal C*, 70(3):823–874, 2010.
- [79] Georges Aad, T Abajyan, B Abbott, J Abdallah, S Abdel Khalek, O Abidinov, R Aben, B Abi, M Abolins, OS AbouZeid, et al. Measurement of the electroweak production of dijets in association with a z-boson and distributions sensitive to vector boson fusion in proton-proton collisions at $\sqrt{s}=8$ tev using the atlas detector. *Journal of High Energy Physics*, 2014(4):1–56, 2014.
- [80] Matteo Cacciari, Gavin P Salam, and Gregory Soyez. The anti-kt jet clustering algorithm. *Journal of High Energy Physics*, 2008(04):063, 2008.
- [81] Andrej N Kolmogorov. *Sulla determinazione empirica di una legge di distribuzione*. na, 1933.

-
- [82] Nickolay Smirnov. Table for estimating the goodness of fit of empirical distributions. *The annals of mathematical statistics*, pages 279–281, 1948.
- [83] Rene Brun and Fons Rademakers. Root—an object oriented data analysis framework. *Nuclear Instruments and Methods in Physics Research Section A: Accelerators, Spectrometers, Detectors and Associated Equipment*, 389(1):81–86, 1997.
- [84] Jan Therhaag and TMVA Core Developer Team. Tmva-toolkit for multivariate data analysis. In *INTERNATIONAL CONFERENCE OF COMPUTATIONAL METHODS IN SCIENCES AND ENGINEERING 2009:(ICCMSE 2009)*, volume 1504, pages 1013–1016. AIP Publishing, 2012.
- [85] Measurements of multijet production cross sections in proton-proton collisions at 7 TeV center-of-mass energy with the ATLAS Detector. Technical Report ATLAS-CONF-2010-084, CERN, Geneva, Oct 2010.
- [86] Glen Cowan, Kyle Cranmer, Eilam Gross, and Ofer Vitells. Asymptotic formulae for likelihood-based tests of new physics. *The European Physical Journal C-Particles and Fields*, 71(2):1–19, 2011.
- [87] Alexander L Read. Presentation of search results: the cls technique. *Journal of Physics G: Nuclear and Particle Physics*, 28(10):2693, 2002.
- [88] Bernhard Mistlberger and Falko Dulat. Limit setting procedures and theoretical uncertainties in higgs boson searches. *arXiv preprint arXiv:1204.3851*, 2012.
- [89] Ulrik Egede. *The search for a standard model Higgs at the LHC and electron identification using transition radiation in the ATLAS tracker*. PhD thesis, DEPARTMENT OF PHYSICS, LUND UNIVERSITY, 1998.
- [90] G Aad, E Abat, B Abbott, J Abdallah, A A Abdelalim, A Abdesselam, O Abdinov, B Abi, M Abolins, H Abramowicz, et al. Expected performance of the atlas experiment-detector, trigger and physics. 2008.
- [91] Performance of the ATLAS Secondary Vertex b-tagging Algorithm in 7 TeV Collision Data. Technical Report ATLAS-CONF-2010-042, CERN, Geneva, Jul 2010.
- [92] Performance of the ATLAS Secondary Vertex b-tagging Algorithm in 900 GeV Collision Data. Technical Report ATLAS-CONF-2010-004, CERN, Geneva, Jun 2010.

-
- [93] Rudolph Emil Kalman. A new approach to linear filtering and prediction problems. *Journal of Fluids Engineering*, 82(1):35–45, 1960.
- [94] Commissioning of the ATLAS high-performance b-tagging algorithms in the 7 TeV collision data. Technical Report ATLAS-CONF-2011-102, CERN, Geneva, Jul 2011.
- [95] *b*-jet tagging calibration on *c*-jets containing D^{*+} mesons. Technical Report ATLAS-CONF-2012-039, CERN, Geneva, Mar 2012.
- [96] Measurement of the b-tag Efficiency in a Sample of Jets Containing Muons with 5 fb^{-1} of Data from the ATLAS Detector. Technical Report ATLAS-CONF-2012-043, CERN, Geneva, Mar 2012.
- [97] Measurement of the Mistag Rate with 5 fb^{-1} of Data Collected by the ATLAS Detector. Technical Report ATLAS-CONF-2012-040, CERN, Geneva, Mar 2012.
- [98] Measuring the b-tag efficiency in a top-pair sample with 4.7 fb^{-1} of data from the ATLAS detector. Technical Report ATLAS-CONF-2012-097, CERN, Geneva, Jul 2012.
- [99] Matt A Dobbs, Stefano Frixione, Eric Laenen, Kirsten Tollefson, H Baer, E Boos, B Cox, R Engel, W Giele, J Huston, et al. Les houches guidebook to monte carlo generators for hadron collider physics. *arXiv preprint hep-ph/0403045*, 2004.
- [100] Andy Buckley, Jonathan Butterworth, Stefan Gieseke, David Grellscheid, Stefan Höche, Hendrik Hoeth, Frank Krauss, Leif Lönnblad, Emily Nurse, Peter Richardson, et al. General-purpose event generators for lhc physics. *Physics Reports*, 504(5):145–233, 2011.
- [101] Adam Alloul, Neil D Christensen, Celine Degrande, Claude Duhr, and Benjamin Fuks. Feynrules 2.0—a complete toolbox for tree-level phenomenology. *Computer Physics Communications*, 185(8):2250–2300, 2014.
- [102] J Orbach. Principles of neurodynamics. perceptrons and the theory of brain mechanisms. *Archives of General Psychiatry*, 7(3):218–219, 1962.
- [103] David E Rumelhart, Geoffrey E Hinton, and Ronald J Williams. Learning internal representations by error propagation. Technical report, DTIC Document, 1985.
- [104] Glen Cowan. *Statistical data analysis*. Oxford University Press, 1998.
- [105] H Fairfield Smith. A discriminant function for plant selection. *Annals of Eugenics*, 7(3):240–250, 1936.

-
- [106] Prasanta Chandra Mahalanobis. On the generalized distance in statistics. *Proceedings of the National Institute of Sciences (Calcutta)*, 2:49–55, 1936.